THE SONIC HEDGEHOG PATHWAY MEDIATES CENTRAL REGULATION OF CEREBELLAR DEVELOPMENT AND SARCOMA PHENOTYPIC OUTCOME

By

Jonathan Fleming

Dissertation

Submitted to the Faculty of the

Graduate School of Vanderbilt University

in partial fulfillment of the requirements

for the degree of

DOCTOR OF PHILOSOPHY

in

Cell and Developmental Biology

May, 2014

Nashville, Tennessee

Approved By:

James R Goldenring, MD, PhD

David Miller, Phd

Andrea Page-McCaw, Phd

Anna Means, Phd

Chin Chiang, PhD

To my family

ACKNOWLEDGEMENTS

When my time of study in the Chiang laboratory began in May, 2008 I was quite naïve, in science, but in life as well. I was twenty-four years old, and I am now thirty. These years of study have most certainly been a formative experience, charted by what I consider extensive professional and personal growth.

I chose to join Chin's lab because I knew the training environment he maintains is rigorous, and his trainees are taught to conduct their science as he conducts his, with serious dedication to finding the truth and following wherever it leads. Always, the best effort was expected from every member of our research team, and often meeting such high expectations proved difficult. However, our group worked well together, and I very much enjoyed my training experience. Even though seemingly harsh at times, the benefit far outweighed the cost, as the skills and strengths I have gained greatly exceed the potential I originally felt I possessed. My time in the Chiang lab was transformative and truly enriching.

Not only did Chin guide me, but his wife, Ying, who is also a gifted researcher, oversaw much of my progress. They shared with me their scientific vision, an appetite for frequent debate and discussion, and energy for research that I believe are mostly unparalleled. Chin and Ying pushed me to always be better, to ask the right questions and address them with the best and most direct experimental design. From them I learned far too much to summarize here; but, I will say that they trained me to think and develop questions independently, to observe carefully and not only

look for that which I expect to find, and to defend my ideas and findings. All of which are fundamental strengths an aspiring young scientist should aim to develop.

There are many current and past members of the Vanderbilt research community that have made substantial contributions to my training and to my research. Chris Wright, D. Phil has established and maintained the Program in Developmental Biology that has helped build an incredibly strong environment for education and collegial research. His program provided me directly with many beneficial experiences, by allowing opportunities for both learning and teaching here at VUMC as well as for engaging with visiting scientists of stature, all of whom shared insightful advice for career development and happy living. Chris has been generous, not only with reagents but especially with his personal time. He committed *many* hours to helping me to develop critical science writing skills. To Chris I am truly grateful.

I entered into the realm of sarcoma biology quite by accident, so when that transition came I was unaware of many things relevant to my new area of investigation. Luckily, I was able to find several collaborators here at VUMC that readily lent their expertise, and often reagents, which proved critical to guiding my work forward. These investigators include Jennifer Black, MD, Cheryl Coffin, MD, Patrick Grohar, MD, PhD, and Scott Borinstein, MD, PhD.

I must thank Catherine Alford and Yan Guo, PhD for lending technical support and for helping me better understand and appreciate science and technology. Cathy provided years of assistance with fluorescence activated cell sorting, while Yan lent his expertise with informatics and statistics. Mark deCaestecker, MS, PhD, has consistently been a great friend on and off campus, and gave me valuable teaching opportunities by entrusting to me roles in his Cancer and

Embryonic Development course as guest speaker and course organizer. Rebecca Ihrie, PhD has provided critical feedback on manuscripts and has taught me how to perform stereotactic micro-injections, a technique that I suspect will benefit my work significantly in the future.

All along the way my thesis committee has been a strong guiding force, helping lead my development as a student. Jim Goldenring, MD, PhD has always provided support and guidance, even prior to becoming my committee chair. I was fortunate to have had Stacey Huppert, PhD, serve as a committee member before departing Vanderbilt. I am grateful for the opportunities I have had to learn from David Miller, PhD, Anna Means, PhD, and Andrea Page-McCaw, PhD, the remaining member of my thesis committee.

I certainly would not have arrived in graduate school at Vanderbilt had it not been for several previous mentors. Lynn Matrisian, PhD and Conor Lynch, PhD provided my first real world research experiences by welcoming me into their lab for two consecutive undergraduate summers (2005 and 2006). They embraced my enthusiasm to learn, even though it was accompanied by great inexperience. Importantly, they committed to nurturing my desire to seek further training and find opportunities. Ron Rosen, who is an out-standing college educator, was a mentor with whom I worked closely during my time at Berea College. He contributed greatly to my educational experience and provided my first research experience, which ultimately led a life in research. Another stand out educator to whom I am grateful is Philip Traina, an impassioned high school Latin instructor, who taught me language and urged me to pursue higher education.

I have been very fortunate also to have a loving and gracious support network, including my immediate family members and an extensive collection of friends. My mother, Dawn, and my siblings, Chris, Emily, and Elizabeth, and now their respective spouses and children, have continue to enrich my life immeasurably.

TABLE OF CONTENTS

LIST OF FIGURES

LIST OF ABBREVIATIONS

aP2	Adipocyte protein 2
ASD	Autism spectrum disorder
Atoh1	Atonal 1
BDNF	Brain derived neurotrophic factor
β-gal	β-galactosidase
BLBP	Brain lipid binding protein
BrdU	Bromo deoxyuridine
CAG	Chicken β-actin
CB	Cerebellum
CD15	Leukocyte cluster of differentiation 15
CD133	Leukocyte cluster of differentiation 133
CNS	Central nervous system
DCN	Deep cerebellar nuclei
EFT	Ewing's family of tumors
EGF	Endothelial growth factor
EGL	External granule cell layer
Fabp4	Fatty acid binding protein 4
FACS	Fluorescent activated cell sorting
FCS	Forward scatter
GAD	Glutamic acid decarboxylase
GABA	γ-aminobutyric acid

GAPDH	Glyceraldehyde 3-phosphate dehydrogenase
GCP	Granule cell precursor
GFAP	Glial fibrillary acidic protein
GIFM	Genetically inducible fate mapping
Glast	Glutamate aspartic acid transporter
IGL	Internal granule cell layer
MB	Midbrain
MBP	Myelin basic protein
ML	Molecular layer
MRF	Myogenic regulatory factor
NSC	Neuronal stem cell
OPC	Oligodendrocyte precursor cell
Pax2/3/7	Paired box2/3/7
Pcp2	Purkinje cell protein 2
PCL	Purkinje cell layer
PDGF	Platelet derived growth factor
PN	Purkinje neuron
PNET	Peripheral neuro-ectodermal tumor
PPARγ	Peroxisome proliferator-activatod receptor gamma
Ptch1/ PTCH1	Patched/ PATCHED1
Ptf1a	Pancreatic transcription factor 1a
PWM	Presumptive white matter
RL	Rhombic lip

RMS	Rhabdomyosarcoma
RNA	Ribonucleic acid
ROI	Region of interest
RT-PCR	Reverse transcription-polymerase chain reaction
SAG	Smoothened agonist
SEM	standard error from the mean
Shh	Sonic hedgehog
Smo	Smoothened
SmoM2	SmoothenedM2
Sox2/10	Sex determining region Y box-2/10
SRCS	Small round cell sarcoma
SVZ	Subventricular zone
TM	Tamoxifen
Tnc	TenascinC
USTS	Undifferentiated soft tissue sarcoma
VZ	Ventricular zone
Wnt	Wingless –int-1
WM	White matter
YFP	Yellow fluorescent protein

ABSTRACT

Sonic hedgehog (Shh) signaling regulates critical processes during embryonic development and in homeostasis of adult tissues. Deregulated pathway activity is a major factor underlying the etiology of numerous developmental disorders and cancers. In this dissertation, I investigated early neonatal cerebellar development, where I identified that the Purkinje neuron utilizes bi-directional distribution of Shh to centrally regulate neurogenesis, and to expand a previously unappreciated stem cell – progenitor cell lineage in the white matter niche. Additionally, I established a novel mouse model for a soft tissue sarcoma, Ewing's sarcoma. These findings provide new understanding of how the Purkinje neuron oversees cerebellar development, as well as key insight into the molecular underpinnings of a Shh-driven sarcoma variant.

CHAPTER I

GENERAL INTRODUCTION

During embryonic development the rudiments of the central nervous system (CNS) emerge as the neural tube is progressively partitioned along the anterior-posterior axis. Ontogeny of the cerebellum, or "mini-brain" as it is also known, initiates from rhombomere one at a region that is destined to become the hindbrain-midbrain boundary (Sotelo, 2004). The cerebellum is a brain structure that is well-known for it's absolute requirement in coordinating fine motor control, but in recent years a contribution to mediating higher cognitive functions has been revealed concomitant with the identification of important neuronal connections between the cerebellum and the pre-frontal cortex (White and Sillitoe, 2012).

Historically, the cerebellum has provided a "go-to" system for pioneering neurobiologists, facilitating several of the most fundamental concepts in neuroscience. The architecture of the cerebellar cortex naturally lends itself to the study of complex neurodevelopmental processes. It displays a stereotypical laminar structure in which only a limited number of well-characterized neuronal subtypes are encountered, and they are divided into two major categories based on neurotransmitter profile: GABAergic or Glutamatergic. The mature cerebellum contains four cortical layers, the outer-most molecular layer (ML), which overlies the Purkinje cell layer (PCL). Beneath that is a hyper-dense layer called the internal granule cell layer (IGL), comprised almost entirely of granule cells, the most abundant neuronal type in the entire brain. At the cerebellar core is a layer of white matter (WM), which mostly contains myelinated axonal

projections and glial cell types, oligodendrocytes and astrocytes (Sillitoe and Joyner, 2007; Sotelo, 2004).

Outside-to-inside, cerebellar neurons include the inhibitory, GABA-expressing component: basket and stellate cells (ML), Purkinje neurons (PCL), Golgi and Lugaro cells (IGL), and a subset of deep cerebellar nuclei (DCN) neurons within the core of the WM. The cerebellar excitatory, Glutamate-expressing component includes candelabrum cells (PCL), granule cells and unipolar brush cells (IGL), and the remaining DCN neurons (WM). All of these neurons are arranged into a complicated circuit the central node of which is the Purkinje neuron (PN). PNs not only received input from this cerebellar circuit, but also exchange input with clusters of neurons housed within the brain stem and spinal cord, making them the only projection neurons within the cerebellar system, and all others local circuit interneurons. Collectively, that totals only nine neuronal cell types, for which the morphology and localization is known. One last cell type of note are the Bergmann glial cells, a population of unipolar astrocytes occupying the PCL that appear to play an important role in the development and maintenance of the cerebellar system (Sillitoe and Joyner, 2007; Sotelo, 2004).

This description accounts for the basic outline of cerebellar cortical architecture, or what the cerebellum looks like as a finished product of normal development. However, much is also known regarding the origin of the cell types described above, and of the foliation events that impart the cerebellum with a distinctively folded cortex, a striking structural motif not seen elsewhere in the CNS. The origin of all nine neuronal subtypes can be traced back to two neuroepithelial layers of the embryonic cerebellar anlagen, a nascent but cylindrical structure,

and are born in an "inside-out" sequence with the inner-most cells appearing first (Leto et al., 2009). The ventricular zone (VZ), which is adjacent to the hindbrain 4th ventricle, harbors neuronal stem and progenitor cells with potential to eventually furnish all GABAergic neurons and glia (Altman J, 1997). Progenitor cells delaminate form the VZ, migrate radially into the cerebellar primordium and either become the first born GABAergic neurons or persist postnatally as progenitors within the presumptive white matter (PWM) that eventually give rise to the largest fraction of the inhibitory component, basket and stellate cells (Leto et al., 2010).

Meanwhile, progenitors in the adjacent rhombic lip (RL) give rise exclusively to the Glutamatergic component. Granule cell precursors (GCPs) exit the RL and undergo tangential migration to form the external granule cell layer (EGL), a transient germinal layer that envelops the growing cerebellum until postnatal day 15 in mice. Intense clonal expansion of GCPs is the driving force behind cerebellar growth and foliation. As they exit the cell cycle, GCPs then migrate inward, forming the IGL, and as developmental time progresses the EGL disappears, leaving the ML exposed at the superficial, pial surface of the cerebellum (Machold R., 2005).

Additionally, much is also known about the regulation of cerebellar development, in particular the transcriptional code necessary for segregating the two major neuronal lineages. Expression of the transcription factor Atoh1 is needed to specify the Glutamatergic lineage, while Ptf1a function is required to induce GABAergic fate (Hoshino et al., 2005; Machold R., 2005). The molecular signals responsible for expanding these lineages and dictating subtype choice are not at all that well understood, but it is clear that a secreted signaling molecule, called Sonic hedgehog (Shh), is the principal factor that induces cellular proliferation of GCPs, and is thus

required for cerebellar growth (Dahmane and Ruiz i Altaba, 1999; Lewis P.M., 2004; Wallace, 1999; Wechsler-Reya and Scott, 1999).

Shh is a lipid-modified protein from a family of three mammalian hedgehog (Hh) isoforms (Ingham PW, 2001). Originally, the Hh gene was discovered in a genetic mutational screen in the fruit fly, Drosophila melanogaster, in which mutant embryos failed to undergo correct segment patterning and ultimately were small, roundish-looking and covered in bristles, similar to a hedgehog. Findings from this screen led to the eventual Nobel prize in physiology or medicine in 1995 for Eric Wieschaus and Christiane Nusslein-Volhard, who along with other investigators uncovered the genes encoding the core components of the Hh signaling cascade. In flies, Hh protein is secreted by producing cells and is transmitted over some distance to receiving cells where it binds to a 12-pass transmembrane receptor, Patched1 (Ptch1). This binding event between Hh and Ptch1 relieves inhibition on a second transmembrane protein, Smoothened (Smo), allowing it to potentiate an intracellular cascade culminating in activation of target gene expression, which is mediated by the transcription factor, Cubitus interruptus (Ci). In the absence of Hh, Ci is maintained as a transcriptional repressor of target genes (Ingham PW, 2001).

Though very similar in terms of basic outline, the pathway in mammals is somewhat more complex. However, the core components remain the same; Hh binds to Ptch1, relieving inhibition of Smo. The transcriptional repressor/ activator functions of Ci are carried out by a family of three proteins, the Glioma-associated (Gli1) transcription factors, Gli1, Gli2 and Gli3. Gli1 and 2 primarily mediate activation, while in the absence of Hh ligand repression is mediated by Gli3. Another significant difference between invertebrate and vertebrate Hh signaling is that

the latter requires a specialized microtubule-based cellular organelle called a primary cilium (Huangfu and Anderson, 2005). All mammalian cells project a single primary cilium that serves as a cellular antenna, enabling cells to perceive cues within their local environment. Core Hh components localize to the cilium, and ciliary function is absolutely required for transducing pathway activity intracellularly (Haycraft C et al., 2005). However, invertebrate Hh signaling does not require this cellular structure.

A number of Hh target genes have been identified, the products of which act as downstream effectors of Hh signaling to mediate diverse and context-dependent processes. Two core pathway components, Ptch1 and Gli1, are both Shh target genes themselves, providing reliable read-outs to identify Shh-responding cells. Classically, Hh signaling is known to mediate two major functions, it is known to act as either a morphogen or a mitogen, meaning it induces cellular fate choices or cellular division, respectively (Fuccillo et al., 2006). Just prior to mid-embryogenesis in the ventral neural tube, or floor plate, where notochord-derived Shh is known to act (and later floor plate-derived Shh), specific neural cells fates are determined via induction of target gene expression (Chiang et al., 1996). One example is the transcription factor Nkx2.2, which designates the progenitor domain of V3 interneurons (Vokes et al., 2007). Another classic example of Shh-mediated patterning is the developing limb bud where Shh expressed in the posterior compartment is required to establish digit identity. Genetic and chemical studies have shown that Shh signaling is absolutely required for patterning these regions, among others, and severe defects in axial patterning result in the absence of normal Shh signaling (Chiang et al., 1996; Cooper et al., 1998).

As mentioned above, Shh also provides an instructive cue that induces cellular proliferation, and there are many examples during development and in the homeostasis of adult tissues where this function is of great importance. The clonal expansion of GCPs that transforms the cerebellum into an extensively foliated structure is driven by mitogenic Shh activity. Long after the EGL has vanished and the adult brain structure is completed, Shh continues to maintain proliferative progenitor populations in forebrain regions, in particular the subgranular zone (SGZ) in the hippocampal dentate gyrus, and the subventricular zone (SVZ) of the lateral ventricles (Fuccillo et al., 2006). In addition to this function, Shh also maintains quiescent stem cell populations residing in both germinal zones (Ahn and Joyner, 2005). Even outside the CNS, Shh maintains stem cell populations. In the hair follicle stem cell niche, Shh signals to basal progenitors within the bulge domain that maintain the structure throughout life (Brownell et al., 2011; Chiang et al., 1999). An important and not well-understood issue is what cellular source provides Shh ligand to these critical regions, and indeed this is an area of active investigation. The study presented here in CHAPTER III will address this very idea, by describing a role for Purkinje neuron-derived Shh in the PWM of the neonatal cerebellum (Fleming et al., 2013).

Since Shh function is such an important player in maintaining proliferative populations and stem cells, it may not a great stretch of imagination to realize that deregulation of this potent mitogenic cue can also lead to oncogenic transformation. The big three cancer types associated with oncogenic Shh pathway activity are medulloblastoma (cerebellar cancer arising from GCPs), basal cell carcinoma (skin cancer arising from hair follicle stem cells) and rhabdomyosarcoma (soft tissue sarcoma linked to precursors of muscle and fat). Mutations

leading to these forms of cancer are most typically associated with deactivation of Ptch1, or activating mutations in Smo (Ruiz i Altaba et al., 2002).

Rhabdomyosarcomas (RMS) fall within the category of small round cell sarcomas (SRCS), which is a broad spectrum of cancer entities (Kikuchi et al., 2011). Oncogenic Shh pathway activity has only been linked so far to RMS, however, the study described here in CHAPTER IV will present a strong argument that activation of human GLI2 leads to a different sarcoma variant, the Ewing's family of tumors (EFT). One major difference that distinguishes RMS from EFT is line of differentiation, RMS are characterized and diagnosed based upon myogenic differentiation. These sarcomas typically express molecular markers of differentiated muscle cells (Desmin), or muscle precursors (MyoD, Myogenin, Myf5 and Pax7) (Lessnick et al., 2009). However, Ewing's sarcoma, first described by James Ewing in 1975 have primarily received a diagnosis of exclusion since these sarcoma variants do not exhibit an obvious line of differentiation. Instead, members of the Ewing's family, which include osteosarcoma, extraosseous sarcoma, and primitive neuroectodermal tumors (PNETs), receive diagnostic conformation based upon the presence of a specific reciprocal chromosomal translocation event, t(11, 22); (q24, q12) (Lessnick et al., 2009).

This event fuses the *trans* activation domain of the TET protein, EWS, with the DNA-binding domain of ETS transcription factor, FLI1, producing a chimeric transcription factor, EWS-FLI1. This resulting oncoprotein is thought to be associated with >95% of EFT cases. Genomic studies have indicated that fusion redirects targeting of FLI1 to cancer associated genes, whereas it typically binds within proximal promoter elements of genes associated with development of the

hematopoietic system where it is known to play an important role (Liu et al., 2008; Patel et al., 2012).

EFT are highly aggressive sarcomas, most common in children and young adults, and require aggressive chemotherapy treatment programs. Although EWS-FLI1 appears to be an important mediator of EFT formation, the key molecules that act downstream of EWS-FLI1 are not known. No doubt the lack of this knowledge, along with a protracted absence of genetic mouse models for EFT has hindered the ability of researchers to develop new and more powerful diagnostic and treatment resources. Despite multiple attempts, no genetically-inducible mouse model currently exists for EFT, likely attributable to the lethality associated with introduction of EWS-FLI1 (Lin et al., 2008; Torchia et al., 2007). I will argue in CHAPTER IV that GLI2 is an important downstream effector of EWS-FLI1, and that GLI2 activation is sufficient to induce an EFT-like sarcoma phenotype in mice.

CHAPTER II

PROLOGUE

In this section I will present the two areas of research in which I have been most engaged and from which the most significant findings have come. Although, on the surface, these research interests may seem somewhat disconnected, they are strongly linked by several important common themes. Among these connections is the hedgehog signaling pathway, particularly the Sonic hedgehog (Shh) signaling molecule that is absolutely required for many disparate processes during development and for homeostasis in adult tissues.

The Shh signal is indeed potent, necessitating that a tight regulatory balance over pathway activity be in place to ensure that disorder does not ensue, as deregulated Shh signaling has been linked to the etiology of numerous developmental disorders and cancers. Though many players in the Shh pathway have been described, my work has revolved around core components: the receptor Patched1 (Ptch1), the signal transducer Smoothened (Smo), and the Gli transcriptional regulators. The respective functions of these factors are essential for mediating appropriate pathway activity, which can be a powerful oncogenic force when deregulated. For example, consider Gorlin's syndrome, which is caused by an inherited loss of function mutation in PTCH1, resulting in basal cell carcinoma (skin cancer), medulloblastoma (CNS cancer) and Rhabdomyosarcoma (soft tissue cancer) (Ruiz i Altaba et al., 2002).

In 2008 a "hot topic' in the Shh research community was the role of the primary cilium in transmitting the Shh signal intracellularly. Previous to 2004 the primary cilium was a rather

overlooked cellular organelle, however its connection to the Shh pathway, and to polycystic kidney disease, helped potentiate renewed interest in the structure's importance. When I entered the Chiang lab, a former student, Xi Huang, had just realized a possible contribution of Shh to neurogenesis in a neuroepithelium within the embryonic cerebellum called the ventricular zone (VZ). His finding that Shh signaling drives the expansion of cerebellar precursors in the VZ provided an important mechanism for understanding the genesis of the earliest born cerebellar GABAergic interneurons (Sotelo, 2004).

I chose to follow up on Xi's study by evaluating what role the primary cilium plays in transmitting the Shh signal to VZ precursor cells and did so by conditionally ablating their ciliary function (**Figure 1.1A-B'**). Initially, I was dismayed because this first wave of GABA neurogenesis seemed unaffected during late embryonic development following loss of cilia function. However, I found instead that during early neonatal development GABAergic precursors occupying the innermost presumptive cerebellar white matter (PWM) were greatly reduced in number, and this reduction occurred alongside loss of Shh pathway activity (**Figure 1.1 C-D'** and not shown).

This finding excited me greatly because research from other groups indicated that the PWM serves as a neonatal stem niche cell where a very large second wave of GABA neurogenesis occurs. I looked to see whether the Shh pathway was active in the PWM and this led to my first significant discovery, that Shh is a key signal governing the second wave of cerebellar GABA neurogenesis. My study evolved to include a very intriguing delivery mechanism utilized by producing cells to disseminate Shh over a considerable distance. This was my second major

finding; that Purkinje neurons distribute Shh bi-directionally to oversee the simultaneous generation of spatially and functionally distinct cerebellar interneurons. These findings are detailed at length in CHAPTER III.

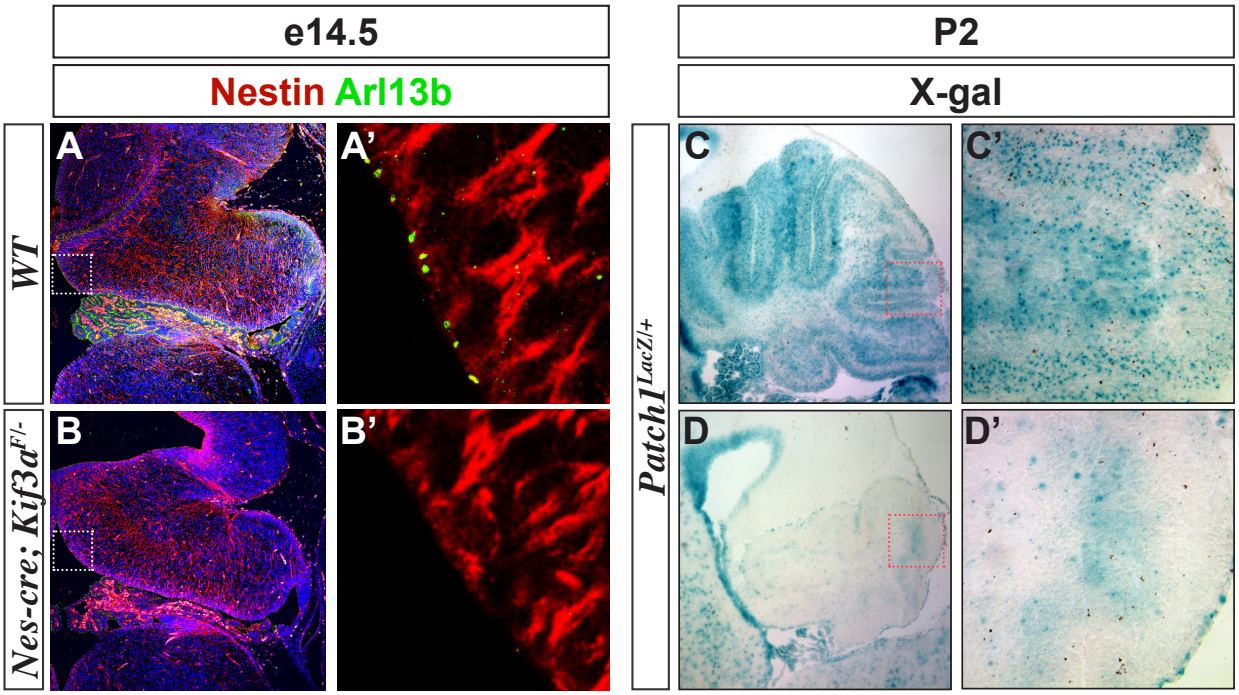

Figure 2.1. Deletion of VZ primary cilia identifies Shh signaling activity in the neonatal PWM niche.

(A-B') Coronal sections of *WT* (A, B') and *Nestin-cre; Kif3a*$^{F/-}$ (B, B') cerebellar VZ regions at e14.5. Radial glial cells express Nestin (red) and display primary cilia marked by Arl13b (green), which are absent in the *Nestin-cre; Kif3a*$^{F/-}$ VZ (B, B'). High magnification regions (A', B') correspond to boxed vermal VZ regions (A, B). (C-D') Sagittal sections of *Ptch*^{lacZ} cerebella showing Shh pathway activity, represented by X-gal staining in the PWM of *WT* (C, C') and *Nestin-cre; Kif3a*$^{F/-}$ littermates (D, D').

Having gained this progress, my research took a substantial step forward, and I chose to maintain focus on my new favorite cell, the Purkinje neuron (PN). Early in 2010 I became fascinated by studies implicating the cerebellum, and importantly the PN, in the autism spectrum disorders (ASD) because loss of function mutations in a gene with great similarity to Ptch1 were linked to ASD (Noor, 2010). We chose to evaluate the expression pattern of *PatchedD1* (Patched domain containing protein 1) in the developing cerebellum, and saw that it is mostly restricted to PNs. This finding led us to speculate that ectopic Shh pathway activation in PNs resulting from loss of PatchedD1 may lead to cerebellar cyto-architectural aberrations noted in some patients with autism. I chose to test this notion and activated Shh signaling cell-autonomously in PNs by introducing activated mutants of Smo (*SmoM2*) or Gli2, the major activator of Shh transcriptional targets (GLI2ΔN). Before any analyses could be performed, we were met with a very unexpected and surprising outcome, compound mutants carrying a PN-specific Cre recombinase, *L7*(*Pcp2-cre*), and GLI2ΔN (**Figure 1.2**) developed remarkably aggressive soft tissue tumors.

This experience served as my personal introduction to the importance of accidental discovery. Certainly, in some cases findings like this one can be attributed to simple good fortune. However, I felt that we had stumbled upon a fortuitous finding because we had asked good questions with solid rationale, and with a well-informed scientific mind the importance of our discovery was quickly recognized.

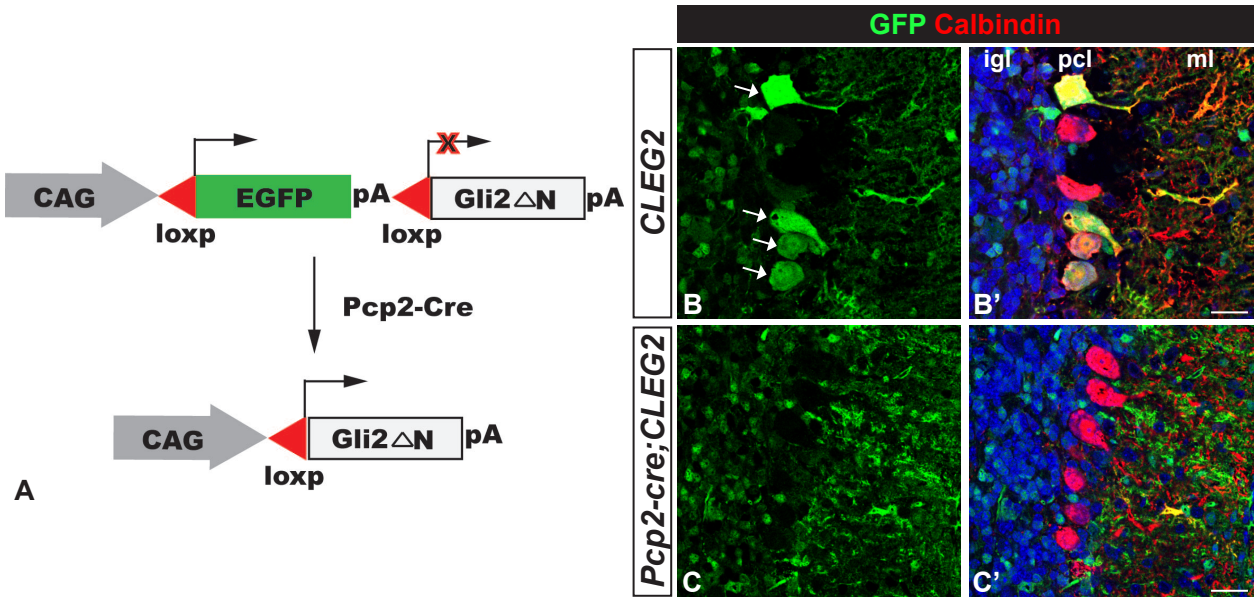

Figure 2.2. Targeting of GLI2Δ N to cerebellar Purkinje neurons in *L7(Pcp2)-cre; CLEG* mice.

(A-C') Activation of the *CLEG2* oncogene in postnatal cerebellar Purkinje neurons. (A) Schematic indicating layout of experiment and design of the *CLEG2* construct; the CAG promoter drives ubiquitous expression of EGFP in the absence of cre recombinase, which when present will simultaneously delete EGFP and activate GLI2ΔN. (B-C') Sagittal sections of *CLEG2* (B, B') and *L7(Pcp2)-cre; CLEG2* (C, C') adult cerebella. Purkinje neurons are marked by Calbindin (B', C'), and lose EGFP expression in the presence of cre (B, B' versus C, C'). IGL, internal granule cell layer; ML, molecular layer; PCL, Purkinje cell layer. Scale bars indicate 25 μm.

Though this study is described in CHAPTER IV, I will say here that I inadvertently activated Gli2ΔN in multi-potent mesenchymal progenitor cells using L7(*Pcp2)-cre*. This led to a tumor phenotype remarkably similar to Ewing's sarcoma, a complicated tumor family within the soft tissue sarcoma spectrum, divergent in many respects from Rhabdomyosarcoma (RMS). Despite nearly two decades of effort, at this time no one has been able to produce a genetically inducible mouse model recapitulating the Ewing's family of tumors (EFT). It seems that quite by accident I did, and simultaneously found that Gli2 is sufficient to induce EFT formation. Currently, the Ewing's community is largely focused on EWS-FLI1, the chimeric oncoprotein resulting from a chromosomal translocation event found in >95% of Ewing's cases. Our data strongly suggest that EWS-FLI1 binds Gli2, and likely utilizes this interaction to promote sarcomagenesis. Reaching this conclusion required considerable research efforts, and sustained passion to conquer new scientific territory.

An important lesson that I learned from this process was seeing the need for being well-informed. Unfortunately, it was not I who first recognized the discovery. Chin noticed that our mutants appeared to have sarcoma, which then seemed most likely to be RMS. Although I was familiar with cancers attributed to deregulated Shh pathway activity, RMS was one with which I had little familiarity. This was soon to change, but at the time my ignorance made the moment bittersweet. Of course I knew that something important had been found, but I was not informed enough on my own to truly appreciate what exactly was before me. However, I have used this learning experience to my benefit, and have made great strides to push forward.

Undoubtedly, deregulated Shh pathway function plays a greater role in sarcoma than is currently appreciated. Most noteworthy may be the conclusion that the level at which Shh pathway activation is induced determines the resulting sarcoma phenotype; whether activation occurs upstream at the level of Ptch1 loss of function/ Smo gain of function versus downstream at the level of transcriptional activator, dictates an RMS outcome versus EFT outcome. The connection between PNs and ASD described above, which was an unintended bridge to interests in sarcoma biology, has grown much stronger, and with that progress my interest in the autism field has thusly heightened. I will return to this connection in CHAPTER V.

Though the connection between the Shh pathway and regulation of stem/ progenitor cell niches, particularly in the developing and adult CNS, is not new, the findings I will describe in CHAPTER III provided several important revelations, extending our understanding of cerebellar neurogenesis considerably. Similarly, the link between deregulated Shh pathway activity and the formation of multiple forms of cancer has been under investigation for well over a decade. Despite this, my work with modeling sarcoma unexpectedly yielded several surprising, and very new, concepts to the field, expanding upon how researchers can think about the origin of a scarcely understood and highly aggressive pediatric cancer. Contemplating the potential impact of these studies, and considering how much knowledge we continue to lack, I am very excited to see what more the future holds.

CHAPTER III

THE PURKINJE NEURON ACTS AS A CENTRAL REGULATOR OF SPATIALLY AND FUNCTIONALLY DISTINCT CEREBELLAR PRECURSORS

Introduction

The embryonic neuroepithelium is the origin of neuronal diversity during genesis of the vertebrate nervous system (Alvarez-Buylla et al., 2001). Neural stem cells (NSCs) within specialized regions of the brain neuroepithelium are capable of generating secondary germinal zones where neurogenesis continues postnatally and in some regions throughout adulthood (Doetsch, 2003; Merkle et al., 2004). These secondary neurogenic zones not only contribute to regional neuronal diversity but also maintain a steady pool of new-born neurons (Doetsch, 2003). However, the establishment of these niches and their maintenance in distinct postnatal environments is less well understood.

The cerebellum provides an attractive system to study signaling mechanisms by which diverse cell types emerge from spatially and temporally defined niches. It has a relatively simple architecture, encompassing nine different neuronal subtypes that are stereotypically situated in distinct cortical layers: the superficial molecular layer (ML), Purkinje cell layer (PCL), internal granule cell layer (IGL), and the innermost white matter (WM) (Hatten and Heintz, 1995). Moreover, functional and anatomical evidence suggests that the cerebellum, in addition to a well-recognized role in motor learning and sensory control, contributes to cognitive function (Gillig and Sanders, 2010).

Neurogenesis in the cerebellum is initiated from two primary germinal neuroepithelia, the ventricular zone (VZ) of the fourth ventricle and the upper rhombic lip (RL). All excitatory glutamatergic neurons, including granule neurons, originate in the RL. The expansion of granule neurons is achieved through proliferation of granule cell precursors (GCPs) mediated by Shh during late embryogenesis and early postnatal life (Dahmane and Ruiz i Altaba, 1999; Lewis P.M., 2004; Wallace, 1999; Wechsler-Reya and Scott, 1999). In contrast, the VZ gives rise to a subset of inhibitory GABAergic interneurons including Purkinje neurons (PNs) and deep cerebellar nuclei (DCN) during embryogenesis (Sillitoe and Joyner, 2007). Recent studies demonstrated that a transventricular Shh signaling mechanism drives the expansion of GABAergic progenitors in the embryonic VZ (Huang X. et al., 2010).

The cerebellar VZ is also the source for precursors of the secondary germinal zone residing in the prospective white matter (PWM) through the first two weeks of postnatal life in mice (Maricich SM, 1999; Sudarov et al., 2011; Yuasa, 1996). Previous retroviral-mediated lineage analysis demonstrated the presence of dividing progenitors in the PWM, contributing to both GABAergic interneurons and astrocytes (Zhang and Goldman, 1996). These late-born interneurons, called stellate and basket cells, reside in the ML where they provide inhibitory input to PNs, the sole output neurons of the cerebellar cortex. More recent genetically-inducible fate mapping (GIFM) in mice showed that NSC-like ‘astroglial cells’ in the PWM robustly generate these late-born cell types (Silbereis et al., 2009).

Astroglia express prospective NSC markers such as Nestin, Sox2 and Leukocyte cluster of differentiation 15 (CD15), and may represent the common origin for different postnatally-born cerebellar cell types generated in the PWM (Silbereis et al., 2009). However, this niche also harbors a Prominin1 (CD133)-expressing population that is capable of self-renewal in culture and clonally generates neurons and glia when implanted into neonatal cerebella, and exhibits intrinsic region character (Klein et al., 2005; Lee et al., 2005). Therefore, it is unclear whether CD15 and CD133 mark common or distinct progenitors or if they are lineally related. Furthermore, their intrinsic developmental potentials in the PWM are unclear, as are the key regulatory signals and cellular mechanisms that support the remarkable neurogenic capacity of the PWM niche.

In this study, we describe functionally divergent PWM progenitor subpopulations with distinctive molecular signatures that commonly respond to Shh. We found that Ptf1a^{+} and Tnc$^{YFP\text{-}Low}$ CD15^{+} cells, which are lineally related to Tnc$^{YFP\text{-}Low}$ CD133^{+} primary progenitors, function as intermediate progenitors that, respectively, expand postnatal precursor pools of GABAergic interneurons and astrocytes. Accordingly, attenuation of Shh signaling in Tnc$^{YFP\text{-}Low}$ cells significantly disrupts the PWM-based expansion of these precursor pools and their progeny. Furthermore, we found that Shh from distant PNs maintains the PWM niche, independent of, GCPs. Thus, PNs couple the generation of excitatory and inhibitory interneurons, facilitating their coordinated integration into the emerging cerebellar circuit permitting their opposing neuronal actions to ultimately feedback on PNs.

Experimental Procedures

Animals

All experiments were performed using young neonatal and adult animals, ages P1-P30 according to the NIH and VUMC Division of Animal Care.

Mice of the following genetic lines, of either sex, were used: *CD133-CreER (Zhu et al., 2009)*, *Gli1*^{nlacZ} (Bai C.B., 2002) *Tnc*$^{YFP\text{-}CreER}$ (see below), *Gli1*^{CreER} (Ahn and Joyner, 2004), *Smo*$^{F/F}$ (Long et al., 2001), *Ptf1a*^{CreER} (Pan et al., 2013), *Shh*^{Cre} (Li et al., 2006), *L7-Cre* (Lewis P.M., 2004), *Shh*$^{F/F}$ (Lewis P.M., 2001), *Math1-CreER*^{T2} (Machold R., 2005), *Rosa26*^{lacZ} (Soriano, 1999), *R26R*^{eYFP} (Srinivas S., 2001), *Ai9* (Madisen et al., 2010), and *mT/mG* (Muzumdar et al., 2007).

Tamoxifen (Sigma) was dissolved to a final concentration of 2 mg/ ml in corn oil (Sigma). Postnatal *CD133-CreER; Ai9*, *Gli1*^{CreER}*; R26R*^{eYFP}, *Ptf1a*^{CreER}*; R26R*^{eYFP}, *Tnc*$^{YFP\text{-}CreERT2}$*; Ai9*, *Tnc*$^{YFP\text{-}CreERT2}$*; Smo*$^{F/-}$, *Atoh1-CreER*^{T2}*; Smo*$^{F/-}$, *Atoh1-CreER*^{T2}*; R26R*^{eYFP} and wild-type littermates received 50 ul of tamoxifen by consecutive intraperitoneal injections on P1 and P2, or P3 and P4 as specified.

BrdU (Roche) was dissolved in PBS to a final concentration of 10 mg/ ml and was administered by intraperitoneal injection. *Tnc*$^{YFP\text{-}CreERT2}$*; Smo*$^{F/-}$ and *wt* littermates and *L7-Cre; Shh*$^{F/-}$ and *wt* littermates received a 2-hour BrdU pulse on P5 prior to sacrifice.

Gene targeting

A “knock-in” strategy was used to create a Cre-recombinase mouse driven by the endogenous Tenascin-C promoter. The Cre transgene was engineered immediately behind the translation start site (ATG) of the tenascin-C gene to ensure that the expression pattern of Cre is similar to that of the endogenous tenascin-C gene. Mouse genomic tenascin-C gene was obtained by a BAC library screen (RPCI-22 mouse BAC library, Invitrogen). The targeting construct was assembled in pBlue (Clontech), including a 4kb 5’ arm homogenous to 5’ region upstream of the tenascin-C gene translation start codon in exon 2, an inducible CreER2, an IRES (internal ribosome entrance site)-EGFP (enhanced green fluorescence protein), a PGK-Neo selection cassette flanked by FRT, and a 2kb 3’ homogenous arm. The CreER2 was made from CreER version 1 (kindly provided by Dr. Andrew P. McMahon) via site directed mutagenesis according to the literature (Feil et al., 1997).

The IRES-EGFP cDNA in the targeting construct allows for detecting site of Cre expression in mice carrying the transgene. The targeting construct was linearized by Ahd I and introduced into E14 129SvJ ES cells with established protocols (Tompers and Labosky, 2004) at Vanderbilt Mouse/ESC Shared Resource. Neo-resistant ES cell clones were screened by southern blot. Primers used for synthesizing 5' probe were: 5'-TAGAGCAGGTGGTCCCAAACAT-3' and 5'-CCAGGAGCCAGGAAATAGCCTTA-3'. Primers used for synthesizing 3' probe were: 5'-GATGACGACTACACTGGGGAA-3' and 5'-ACTGGGGCACCTTTGCTCTT-3'. Positive clones were picked for blastocyst injection, and germline transmission of the transgene was obtained. Mice heterozygous for the tenascin-C-CreER2 allele were viable and of normal size without significant developmental or functional abnormalities.

Mice were genotyped using genomic DNA isolated from tail tissue. PCR primers used to amplify across the region where the 5' CreER2 was inserted were: sense: 5'-GGGGGCAAGAAGGCAAAAAT-3'; antisense-1: 5'-GTTCTGCGGGAAACCATTT-3'; antisense-2: 5'-TCTCGCTTGTGCCTGATGAT-3'. Primer pair of sense and antisense-1 gave a band of ~430bp for a targeted allele and no band for a wild type allele. Primer pair of sense and antisense-2 gave a band of ~300bp for a wild type allele and no band for a targeted allele.

RNA isolation and reverse transcription

Total RNA was purified from sorted cells using the RNeasy mini kit (Qiagen) and cell homogenization was performed using QIAshredder columns (Qiagen). cDNAs were synthesized with 300ng total RNA input for all samples tested using a High-Capacity cDNA reverse transcription kit (Applied BioSciences). PCR was performed with primers for *Gli1* and *GAPDH* at 34 cycles with annealing temperature of 60^{o}C and as previously described (Liu et al., 2013).

Tissue processing and Immunohistochemistry/ Immunocytochemistry

For animals younger than P30, brains were dissected out and fixed in 4% paraformaldehyde for either 4-6 hours or O/N at 4^{o} C. Animals between P21-P30 received 50 ul intraperitoneal injections of Ketamine and received ice-cold PBS via transcardial perfusion followed by 4% paraformaldehyde. Brains were collected and submersion fixed in 4% paraformaldehyde O/N at 4^{o} C. These tissues were either processed for frozen embedding in OCT compound or processed for paraffin embedding. Frozen tissues were sectioned on a Leica cryostat at 10 um, paraffin embedded tissues were cut at 5 um.

Antibodies

Immunohistochemistry (IHC) and immunocytochemistry (ICC) were performed as previously described (Huang X. et al., 2010). The following primary antibodies were used to perform IHC/ ICC on frozen and/ or paraffin tissue sections or for flow cytometry/ FACS: chicken α-βGal (ICL), rabbit α-βGal (ICL), rabbit α-BLBP (Abcam), mouse α-BrdU (DSHB), mouse α-CD15 (eBioscience, MMA), mouse α-CD15 Alexa-567 (BioLegend, MC-480), rat αCD133 PE (eBioscience, 13A4), mouse α-GABA (Simga), mouse α-GAD-67 (Abcam), rabbit α-GFAP (Abcam), mouse α-GFAP (Covance), chicken α-GFP (Aaves), guinea pig α-GLAST (Millipore), mouse α-Glutamate (Swant), rabbit α-Calbindin (Swant), and rabbit α-Ki67 (NeoMarkers), mouse α-MBP (Covance), rabbit α-Musashi (Neuromics), mouse α-Nestin (DSHB), mouse α-NeuN (Millipore), rabbit α-Neurogranin (Millipore), mouse α-O4 (Millipore), rabbit α-Pax2 (Invitrogen), mouse α-Parvalbumin (Sigma), rabbit α-Ptf1a (Hald et al., 2008), rabbit α-Sox2 (Millipore), guinea pig α-Sox10 (Maka et al., 2005), chicken α-Tbr2 (Millipore) and rabbit α-Zic1 (Chemicon). For bright-field staining, species-specific HRP-conjugated secondary antibodies (Invitrogen) were used followed by incubation in DAB reaction (Invitrogen). Double-labeling fluorescence immunohistochemistry was performed using species-specific, AlexaFluor-tagged secondary antibodies Alexa 488, Alexa 568 and Alexa 647 (Invitrogen) followed by counterstaining with To-pro3 iodide (Invitrogen).

X-gal staining and transcript detection

X-gal staining for β-galactosidase activity was performed on post-fixed, frozen sections according to standard protocols. The following cDNAs were used as templates for synthesizing digoxygenin-labeled riboprobes: *Gli1*.

Flow Cytometry, Neurosphere and Differentiation Assays

Cerebella were isolated at P3, P4 or P5 from wild-type *Tnc*$^{YFP\text{-}CreERT2}$ mice and were dissociated to single cell suspensions via microdissection and trituration in sterile PBS, then strained through 40 μm filters. Cells were resuspended in 1% BSA and stained on ice for 30 min with primary antibodies, washed in sterile PBS, and resuspended with DAPI to permit exclusion of non-viable cells. Flow cytometry and cell sorting were performed on a FACSAria cell sorter (BD) to purify Tnc$^{YFP\text{-}low}$-expressing, CD133^{+} or CD15^{+} cells. Tnc$^{YFP\text{-}}$ cerebella and forward scatter (FSC) were used for gating, and post-sort analysis was performed to evaluate purity of sorted cells. These populations were then cultured under standard neurosphere conditions in NSC medium [Neurobasal medium (GIBCO) supplemented with EGF (25 ng/ ml) B27 (GIBCO), N2 (GIBCO), glutamine and Pen-Strep (Cellgro)] for 7-10 days at 37^{o}C, 5% CO_2. For quantification of 2^{o} and 3^{o} neurosphere formation, SAG (20 nM) and KAAD-cyclopamine (4 μM) were used to manipulate Shh signaling. Induction of differentiation was performed on 1^{o} and 2^{o} neurospheres derived from FACS-purified, Tnc$^{YFP\text{-}low}$ cells, which were attached to PDL-coated glass coverslips and cultured for 7-10 days in NSC medium (w/o EGF) containing either PDGF-aa (10 ng/ ml) or 10% serum.

Microscopy

Bright-field images were collected on an Olympus BX51 upright microscope or on a Leica M165 FC stereoscope. Detection of double-labeling was performed using either confocal imaging on a Leica TCS SP5 laser-scanning or with an Olympus fluorescent microscope outfitted with an Optigrid system (qioptiqimaging) for optical sectioning and Metamorph^{TM} software (Molecular Devices) for image acquisition.

Quantifications and statistical analyses

Metamorph^{TM} (molecular devices) and ImageJ software were used to measure area (um^2) for regions of interest (ROI), for acquisition of cell counts, and for surface intensity measurements. For each developmental stage, four ROIs were used per section. For all immunohistochemical stainings cell counts were obtained from a minimum of five to ten sections per brain, and all cell counts were normalized to area. A minimum n=3 animals was required for all genotypes at each stage analyzed. Sections (5 um for paraffin, 10 um for frozen) were collected in serial from midline regions covering 200-400 um of tissue (depending on developmental stage) along the medial-lateral axis. For quantification of 2^o and 3^o neurospheres, single cells were plated at clonal density (1-2 cells/ mm^2) on 60 mm gridded cell culture dishes (SARSTEDT) and neurospheres present within a 100 mm^2 area were counted. Statistical analyses were performed using Prism software (GraphPad).

Results

Shh targets distinct progenitor populations resident in the neonatal PWM

To determine whether Shh signaling is active in the neurogenic PWM niche, we used *Gli1*^{nlacZ} mice to assess Shh pathway activity (Bai C.B., 2002). In addition to previously reported expression in GCPs and Bergmann glia (Corrales JD, 2004; Lewis P.M., 2004), we observed β-galactosidase (β-gal) expression in cells abundant throughout the lobular (but not DCN) PWM at P3 and P5, and observed a similar expression pattern for *Gli1* mRNA, confirming activation of Shh signaling (**Figures 3.1A-B**). To ascertain the molecular identity of this Shh-responding population, β-gal$^+$ cells were quantified in four regions of interest (ROI) that delineate domains

of lobular PWM with greatest frequency of β-gal$^+$ cells (**Figure 3.1A**, R1-4). Because no significant regional variations were observed, ROI measurements were combined to generate a single value.

We found that most β-gal$^+$ cells expressed NSC/ astroglial markers Sox2 (75±11.8% at P3 and 78±9.7% at P5, n=3) and BLBP (60±7.3% at P5, n=3), whereas fewer β-gal$^+$ cells expressed cell cycle marker Ki67 (44±3%, n=3) or surface antigen CD15 (**Figure 3.1C-F**). In the early neonatal PWM, Shh-responding cells are numerous and represent ~one-half of total Sox2$^+$ cells (54±13.2% at P3 or 47±6.6% at P5, n=3), but this signaling appears transient in nature because β-gal$^+$ cells were not detected at P6 (not shown). It is important to note that neither β-gal expression nor concurrent cellular proliferation were observed in the cerebellar VZ (**Figure 3.2 A-A"**), arguing against a contribution from that neuroepithelium in the postnatal period. These data indicate that PWM NSC-like astroglia actively respond to Shh in the early postnatal period.

In contrast, Pax2$^+$ GABAergic progenitors, which delineate the PWM and are largely post-mitotic (Leto et al., 2009; Maricich SM, 1999; Weisheit et al., 2006), were negative for Shh signaling (**Figure 3.1G, G'**). However, many β -gal$^+$ cells expressed Ptf1a (pancreatic transcription factor 1a) (31±4% at P3, n=3, **Figure 3.1H, H'**), which genetic studies have shown is required for GABA-lineage specification (Hoshino et al., 2005; Pascual et al., 2007). Following a 2-hour BrdU pulse we noted a large fraction of Ptf1a$^+$ cells in S-phase that persisted at P6 (**Figure 3.1I**). This observation was surprising given that Ptf1a$^+$ cells in the embryonic cerebellum are exclusively post-mitotic (Huang X. et al., 2010). To assess whether Ptf1a$^+$ cells generate Pax2$^+$ cells, genetically inducible fate mapping (GIFM) experiments were performed

using a *Ptf1a*^{CreERT2} knock-in driver (Pan et al., 2013) paired with *R26R*^{eYFP} mice, to which tamoxifen (TM) was administered on P1 and P2. Some Ptf1a-GIFM cells proliferate in the PWM at P7, but most are Pax2^{+} (**Figure 3.1J, K**), confirming that Ptf1a^{+} cells emerge upstream of and contribute considerably to neonatal Pax2^{+} pools. These data provide a novel cellular mechanism supporting the rapid neonatal expansion of GABAergic progenitors pools. Long-term Ptf1a-GIFM studies revealed exclusive marking of ML GABAergic interneurons at P30, with no labeling of astrocytes or other cell types at P7 or P30 (**Figures 3.1L and 3.2B, C**).

Shh-responding cells establish progenitors of GABAergic interneurons and astrocytes

To characterize the developmental potential of Shh-responding PWM cells, we used GIFM with the *Gli1*^{CreER} mouse, which has been shown to efficiently label Gli1^{+} cells and their progeny 24 hours following TM administration (Ahn and Joyner, 2004). TM was administered to *Gli1*^{CreER}; *R26R*^{eYFP} mice on P1 and P2 (or on P3 and P4) and the fate of YFP^{+} cells was determined at P5, P7 and P30 (**Figure 3.3A**). Because P3, P4 TM administration yielded lower YFP-labeling in marker^{+} populations (not shown), due to the transient nature of Shh signaling in the PWM, administration at P1 and P2 only was used throughout the remainder of our study. We quantified Gli1-GIFM cells by measuring YFP-labeling in four PWM ROI delineated by adjacent NeuN^{+} IGL granule neurons (**Figure 3.4A**). Because substantial regional variations in cre activity were not observed, measurements were combined into a single value. Labeling of Bergmann glia, a persistent population of Shh-responding astrocytes (Corrales JD, 2004; Lewis P.M., 2004) indicated our labeling efficiency was between 18% and 37% at P5 or P7, respectively (n=3) (**Figure 3.4G, H, and J**). As expected, labeling of proliferative GCPs was also observed (**Figure 3.4I**).

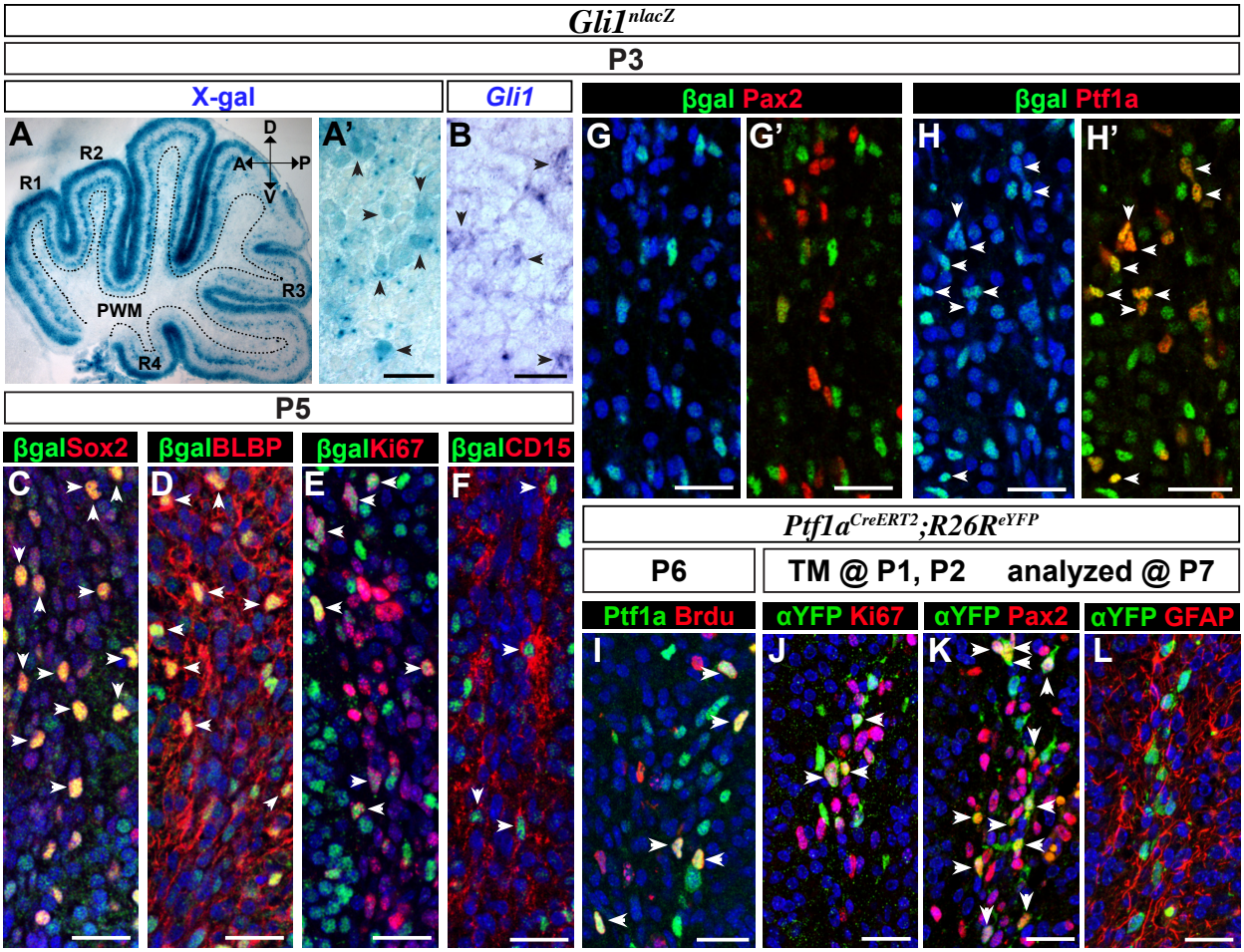

Figure 3.1. Distinct progenitor populations in the neonatal PWM niche respond to Shh.

(**A-H'**) Sagittal sections of *Gli1*^{nlacZ} cerebella showing Gli expression, represented by either X-gal staining (A, A'), or *Gli1* mRNA in situ hybridization (B) or β-gal antibody staining (C-H'), in the PWM. Gli1 expression in the PWM co-localizes with NSC/astroglia markers such as Sox2 (C), BLBP (D) and CD15 (F) as well as proliferative marker Ki67 (E) at P5. It is also expressed in Ptf1a^{+} (H, H') but not Pax2^{+} (G, G') GABAergic progenitors. (I-L) Ptf1a^{+} cells represent a proliferative population of GABAergic progenitors (I, J), and *Ptf1a*^{creERT2}-GIFM analysis reveal that Pax2^{+} progenitors (K) but not GFAP^{+} astrocytes (L) are derived from Ptf1a^{+} progenitors. Black arrowheads indicate X-gal^{+} cells (A') or *Gli1* mRNA expressing cells (B), and white arrowheads indicate double-labeled cells. PWM, presumptive white matter. Scale bars indicate 25 μm.

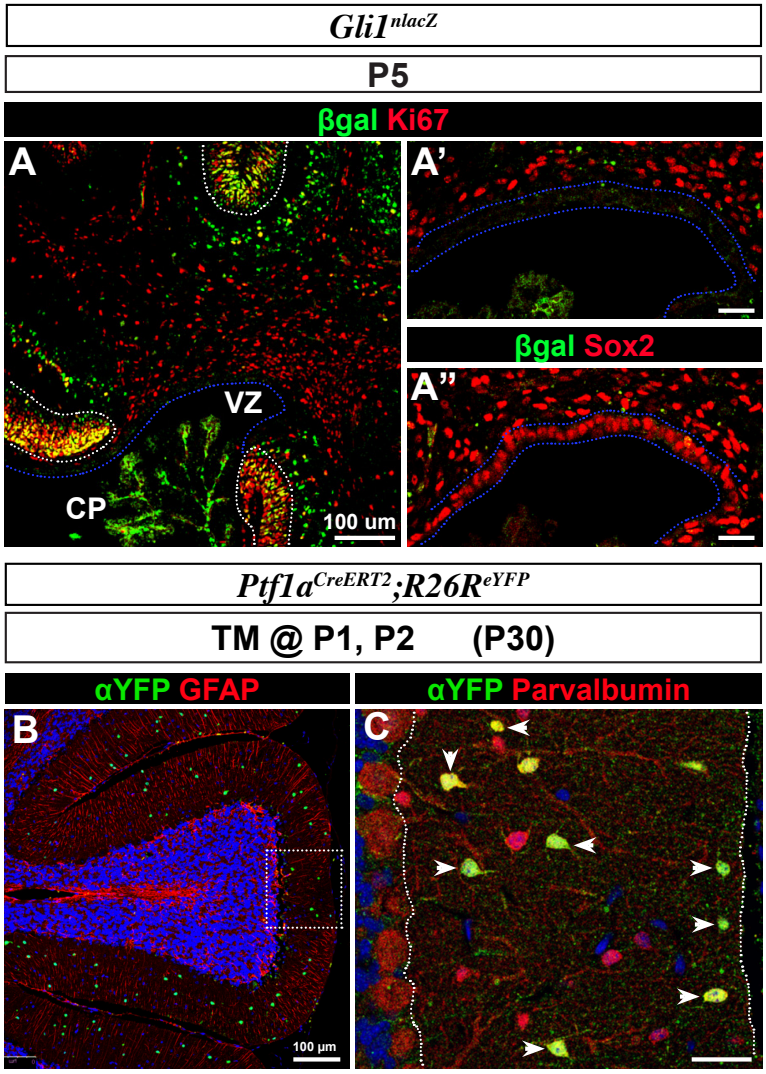

Figure 3.2. Shh signaling is activated in distinct PWM progenitor populations.

(**A-A"**) Sagittal sections of *Gli1*^{nlacZ} cerebella showing Gli1 expression as marked by βgal staining is not detectable in the ventricular zone (VZ) at P5. Note that cells at VZ demarcated by blue dotted lines are no longer proliferative (A') but express Sox 2 (A''). (**B, C**) Ptf1a-GIFM analysis; *Ptf1a*^{CreERT2}*; R26R*^{eYFP} mice received TM on P1, P2 and were analyzed at P30, revealing that Ptf1a^{+} cells generate only ML GABAergic interneurons (Parvalbumin^{+}) but not astrocytes (GFAP^{+}). Nuclei are counter-stained with To-pro3 iodide (blue). White arrowheads indicate double-labeled cells and dotted lines demarcate ML. Scale bars indicate 25 μm unless otherwise indicated.

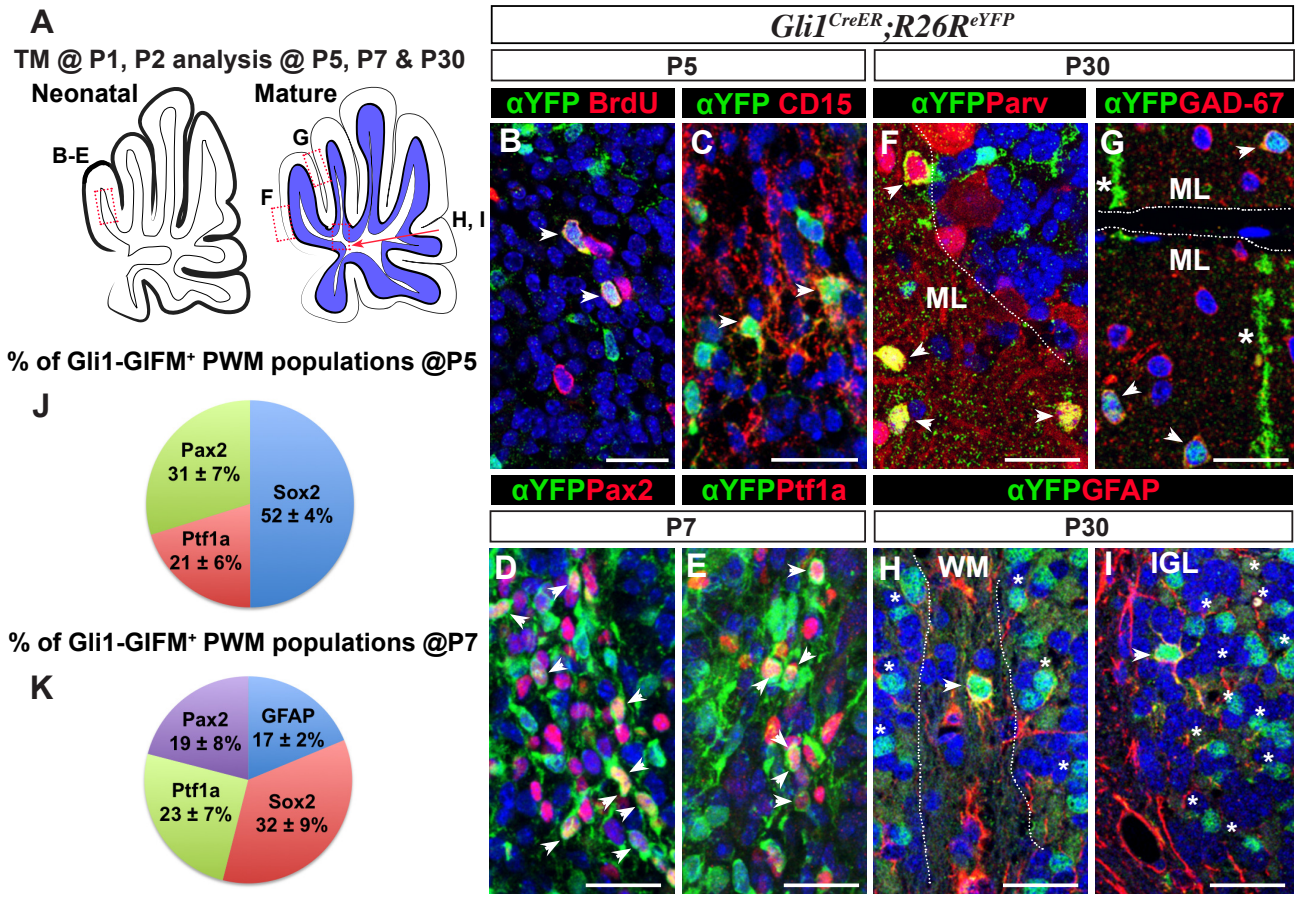

Figure 3.3. PWM Shh-responding cells generate GABAergic interneurons and astrocytes.

(**A**) Schematics indicating regions used for analysis of Gli1-GIFM^{+} cells. (**B-I**) *Gli1*^{CreER}; *R26R*^{eYFP} mice were injected with TM on P1 and 2 and analyzed at P5 (**B, C**), P7 (**D, E**) and P30 (**F-I**). Some Gli1-GIFM^{+} cells highlighted by YFP expression are proliferative at P5 (B), and some express CD15 (C), Pax2 (D), or Ptf1a (E) in the PWM and contribute to both mature GABAergic interneurons (F, G) and astrocytes (H, I). (**J, K**) Quantitative analyses of Gli1-GIFM studies at P5 (**J**) and P7 (**K**) showing percentage of Gli1-GIFM^{+} PWM populations. Dotted line demarcates the PWM or ML as indicated, white arrowheads indicate double-labeled cells, and asterisks mark mature granule neurons. Abbreviations: IGL, internal granule cell layer; WM, white matter; ML, molecular layer. Scale bars indicate 25 μm.

At P5 (n=5), the majority of PWM YFP$^+$ cells express Sox2 (52±4.3%), while the remaining fractions express either Ptf1a (21±5.9%) or Pax2 (31±6.9%) (**Figures 3.3J and 3.4B, D**). We also found fractions of Gli1-GIFM cells that were dividing, based on a 2-hour pulse with S-phase marker BrdU$^+$, or that expressed surface antigen CD15 (**Figure 3.3B, C**). At P7, we detected more extensive YFP-labeling of marker$^+$ populations than at P5, likely from accumulation of these cell types over a 48-hour period. However, the percentage of Sox2$^+$ Gli1-GIFM cells was lower (32±5.5%), suggesting progression to lineage commitment with Gli1-GIFM cells expressing Ptf1a (23±4.2%), Pax2 (19±4.7%) and GFAP (17.3±4.4%) (n=5) (**Figures 3.3D, E, K and 3.4E, F**). We noted that Gli1-GIFM$^+$, Pax2$^+$ cells were abundant only within lobular PWM, but not in the DCN/ periventricular WM (**Figures 3.3D and 3.4B, C**) where a subset of GABAergic DCN interneurons are born during perinatal stages (Leto K, 2006; Maricich SM, 1999).

To establish the terminal fate of Gli1-GIFM cells, we evaluated the *Gli1^{CreER}; R26R^{eYFP}* cerebellar cortex at P30 (n=5). Consistent with the above progenitor labeling at P5-P7, abundant Gli1-GIFM$^+$ cells were found in the ML positive for GAD-67 and Parvalbumin, markers of basket and stellate cells (**Figure 3.3F, G**). However, Gli1-GIFM studies did highlight two spatially segregated populations of astrocytes residing in the IGL and WM (**Figure 3.3H, I**), which likely represent velate protoplasmic (bushy) and smooth protoplasmic astrocytes, respectively (Yamada and Watanabe, 2002). However, we did not find that Gli1-GIFM cells contribute to MBP$^+$ oligodendrocytes (**Figure 3.4K**). Collectively, these findings indicate that Shh-responding PWM cells possess relatively broad developmental potential and contribute to distinct GABAergic interneuron and astrocyte subtypes.

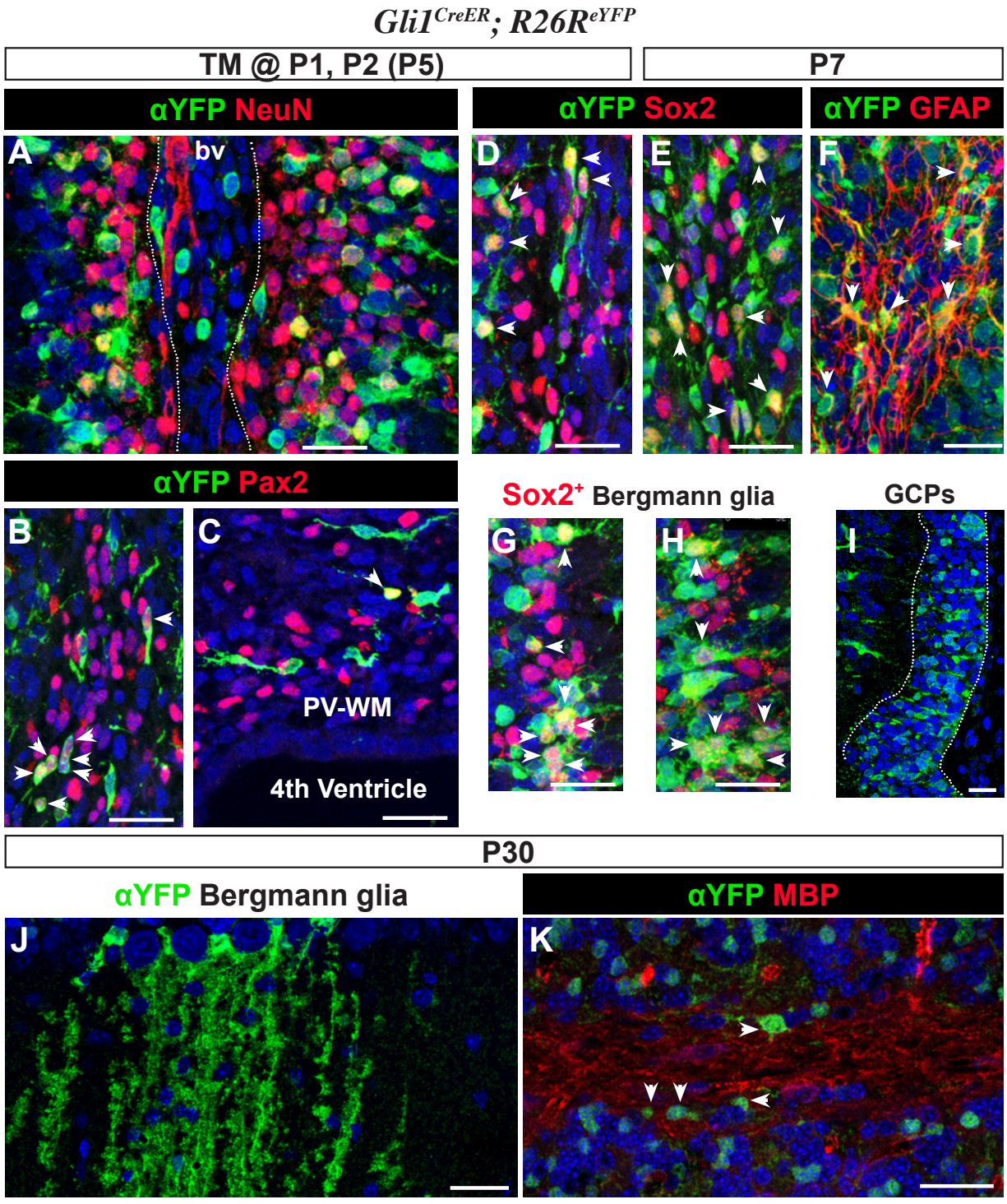
Gli1CreER; R26ReYFP
TM @ P1, P2 (P5)
P7
αYFP NeuN
αYFP Sox2
αYFP GFAP
A
bv
D
E
F
αYFP Pax2
Sox2+ Bergmann glia
GCPs
B
C
PV-WM
4th Ventricle
G
H
I
P30
αYFP Bergmann glia
αYFP MBP
J
K

Figure 3.4. Labeling of PWM Shh-responding cells and their progeny.

(**A-K**) *Gli1*^{CreERT2}*; R26R*^{eYFP} mice received TM on P1, P2 and were analyzed at P5 (**A-D, G**), P7 (**E, F, H, I**), and P30 (**J, K**). Gli1-expressing cells and their progeny (YFP) represent a wide array of cell types in the cerebellum including granule neurons (A), GABAergic interneurons (B, C), astroglia (D, E), Bergmann glia (G, H), and astrocytes (F). Note that Gli1 lineage cells do not contribute to oligodendrocytes as indicated by the lack of Myelin basic protein (MBP) staining (K). Nuclei are counterstained with To-pro3 iodide (blue). White dotted lines demarcate the PWM (**A**) or EGL (**I**). Scale bars indicate 25 μm.. Abbreviations: PV-WM, periventricular white matter; bv, blood vessel.

Low TenascinC^{YFP} reporter expression marks PWM Shh-responding astroglia

To further characterize the molecular identity and function of Shh-responding cells during the early neonatal period, we generated inducible *Tnc*$^{YFP\text{-}CreER}$ mice in which CreER and YFP are expressed as a bicistronic message from the endogenous *TenascinC* (*Tnc)* locus. Previous studies have shown that the extracellular matrix glycoprotein Tnc is expressed in glia occupying the neonatal cerebellar PWM (Yuasa, 1996). Our analyses indicated that *Tnc*$^{YFP\text{-}CreER}$ expression faithfully recapitulates the reported *Tnc* expression pattern, and revealed no Tnc^{YFP} in the VZ at postnatal stages (**Figure 3.5A-C** and 3**.6A, A'**).

Analysis with *Gli1*^{nlacZ} revealed that, similar to Sox2, ~3/4 of β-gal^{+} cells in the PWM express Tnc^{YFP} (74±7% at P3, n=3) (**Figure 3.5A**). Most Tnc^{YFP+} cells, if not all, expressed Sox2 or BLBP at P3 and P5 (**Figure 3.5B, C**), but not GABA progenitor marker Pax2 and rarely GFAP (**Figure** 3**.6B, C**). We performed Tnc-GIFM with TM administered to *Tnc*$^{YFP\text{-}CreER}$*; Ai9*$^{F/+}$ mice at P1 and P2, and analysis at P21 revealed that Tnc^{YFP+} cells, similar to Gli1^{+} PWM cells, contribute extensively to a diverse array of cerebellar cell types, including basket and stellate GABAergic interneurons (Parvalbumin^{+}) and astrocytes (GFAP^{+}) (**Figure 3.5D-F**).

We next measured the NSC attributes of Tnc^{YFP+} astroglia *in vitro*, and found that when cultured under standard neurosphere conditions, cells dissociated from cerebella of P3, P4 or P5 $Tnc^{YFP\text{-}CreER}$ mice consistently generated 1^o neurospheres (**Figure 3.5I-J**), all of which were positive for Tnc^{YFP} (279/279 neurospheres). FACS was used to isolate Tnc^{YFP+} cells from 1^o neurospheres and from freshly dissociated neonatal cerebella (**Figures 3.5G, H** and 3**.6D-F**). From the latter, two separate populations were distinguishable by Tnc^{YFP} fluorescence intensity: a low population (blue peak) and a high population (red peak) (**Figures 3.5H** and 3**.6F**). The low population (hereafter referred to as $Tnc^{YFP\text{-}low}$) exhibited a fluorescence peak that corresponds to that of enriched Tnc^{YFP+} sphere-forming cells (**Figure 3.5G vs. H**), indicating that sphere-forming cells are a distinctive subpopulation that can be readily isolated. Further analysis of $Tnc^{YFP\text{-}low}$ neurospheres, which exhibited capacity for extended self-renewal (*i.e.*, up to 5^o spheres), also revealed robust expression of numerous NSC markers (**Figure 3.5K-P**). The $Tnc^{YFP\text{-}high}$ cells likely represent Bergmann glia as they express higher level Tnc^{YFP} when compared to the PMW astroglia *in vivo* (**Figure** 3**.6G, H**) and the same has been shown at the mRNA level (Yuasa, 1996).

Shh signaling promotes self-renewal in $Tnc^{YFP\text{-}low}$ cells; addition of EGF and Shh agonist SAG (Chen et al., 2002) exerted a synergistic effect on 2^o neurosphere formation, eliciting an ~49% (n=3) increase in 2^o neurospheres versus EGF only, and that SAG alone could not induce neurosphere formation (**Figure 3.7A**). We performed 3^o neurosphere formation and again measured a robust Shh-mediated increase in self-renewal that correlated with expression of *Gli1* mRNA and was attenuated by Shh antagonist KAAD cyclopamine (n=3, **Figure 3.7B, C**).

Furthermore, multi-lineage differentiation capacity was tested, which showed that 3° $Tnc^{YFP\text{-}low}$ neurospheres can generate an extensive spectrum of cerebellar cell types based on marker expression for GABA (GABA, GAD-67, Parvalbumin and Neurogranin) and Glutamatergic lineages (Glutamate, NeuN, Tbr2 and Zic), as well as astrocytes (GFAP) and oligodendrocytes (O4) (**Figure 3.7D-M**).

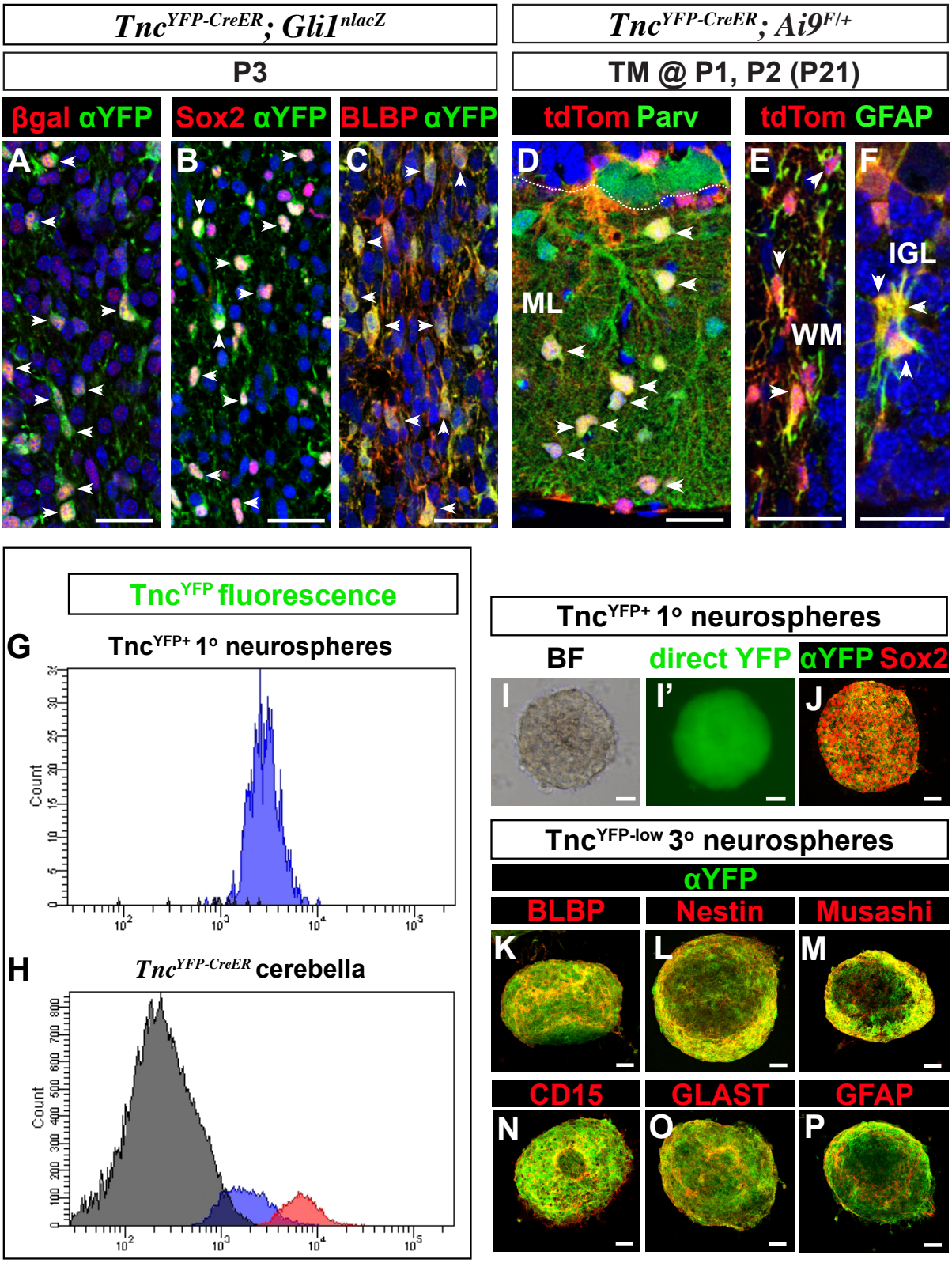
Tnc^YFP-CreER; Gli1^nlacZ
P3
Tnc^YFP-CreER; Ai9^F/+
TM @ P1, P2 (P21)
βgal αYFP
Sox2 αYFP
BLBP αYFP
tdTom Parv
tdTom GFAP
A
B
C
D
E
F
ML
WM
IGL
Tnc^YFP fluorescence
G
Tnc^YFP+ 1° neurospheres
Count
H
Tnc^YFP-CreER cerebella
Count
Tnc^YFP+ 1° neurospheres
BF
direct YFP
αYFP Sox2
I
I'
J
Tnc^YFP-low 3° neurospheres
αYFP
BLBP
Nestin
Musashi
K
L
M
CD15
GLAST
GFAP
N
O
P

Figure 3.5. $Tnc^{YFP\text{-}low}$ expression marks Shh-responding cells capable of self-renewal *in vitro*.

(A-C) Sagittal sections of $Tnc^{YFP\text{-}creER}$; $Gli1^{nlacZ}$ cerebella at P3 showing Tnc expression as marked by YFP co-localizes with β-gal of Gli1 reporter (A), $Sox2^{+}$ (B) and $BLBP^{+}$ (C) astroglia markers. (D-F) $Tnc^{YFP\text{-}creER}$; $Ai9^{F/+}$ mice were received TM on P1, P2 and were analyzed at P30. Tnc-expressing cells contribute both to $Parv^{+}$ GABAergic interneurons (D) and $GFAP^{+}$ astrocytes (E, F) in the cerebellum. White arrowheads indicate double-labeled cells. (G, H) Histograms from FACS showing YFP fluorescence intensity of dissociated Tnc^{YFP+} 2^{o} neurospheres (G) or dissociated P4 $Tnc^{YFP\text{-}CreER}$ cerebella (H). Note that dissociated $Tnc^{YFP\text{-}CreER}$ cerebella resolves into three peaks; grey indicates cells that are negative for Tnc^{YFP}, blue indicates low intensity corresponding to the peak derived from dissociated 2^{o} neurospheres (G, H), and red is high intensity. (I-J) A 1^{o} neurosphere derived from $Tnc^{YFP\text{-}CreER}$ P3 cerebella expresses YFP (I') and NSC Sox2 (J). Bright-field view is shown in (I). (K-P) $Tnc^{YFP\text{-}low}$-derived 3^{o} neurospheres express variety of NSC markers including BLBP (K), Nestin (L), Musashi (M), CD15 (N), Glast (O) and GFAP (P). Abbreviations: IGL, internal granule cell layer; ML, molecular layer; WM, white matter. Scale bars are 25 um.

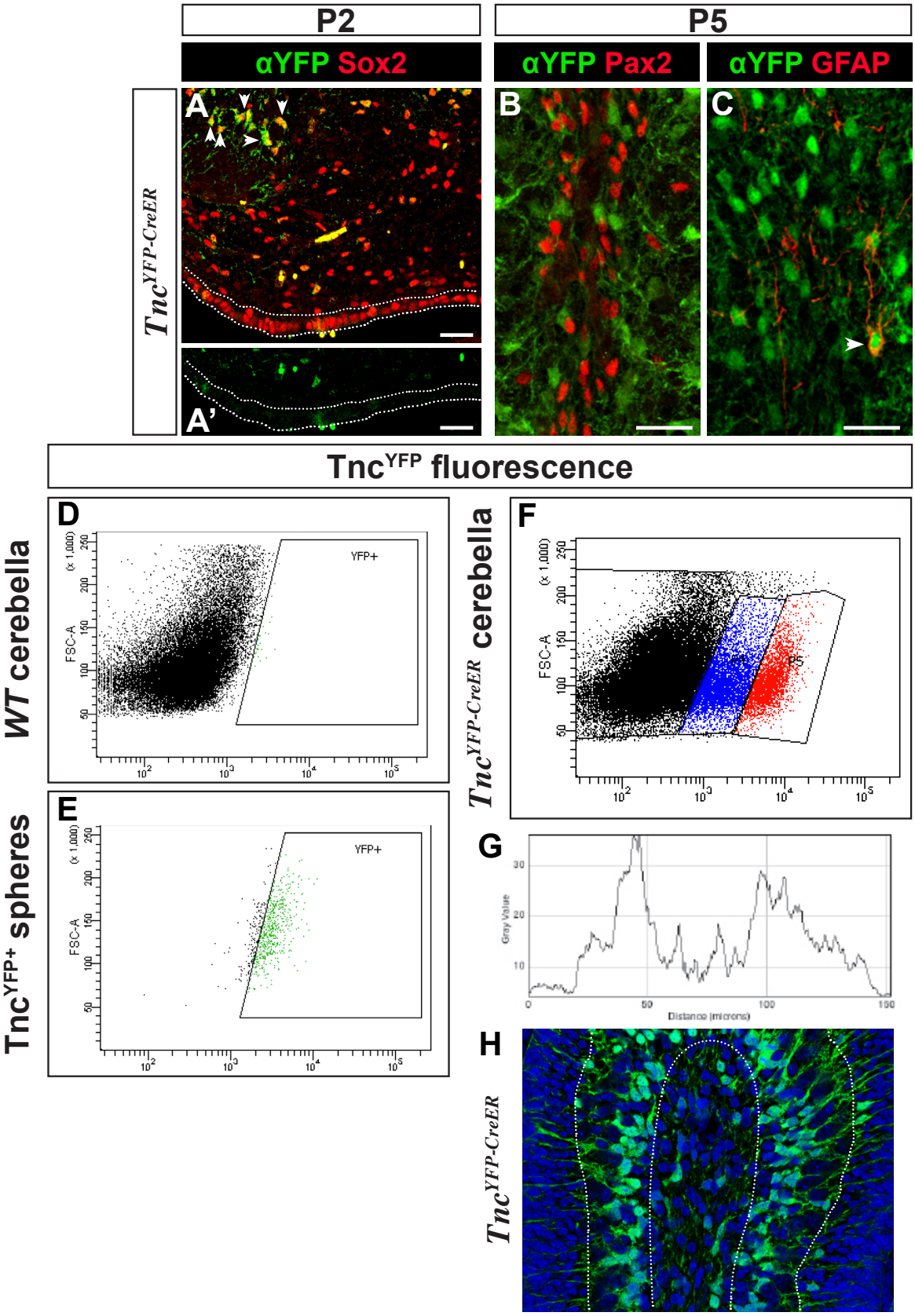
P2
P5
αYFP Sox2
αYFP Pax2
αYFP GFAP
A
A'
B
C
Tnc^YFP-CreER
Tnc^YFP fluorescence
WT cerebella
Tnc^YFP+ spheres
Tnc^YFP-CreER cerebella
D
E
F
G
H
YFP+
FSC-A
(x 1,000)
P5
Gray Value
Distance (microns)

Figure 3.6. Tnc^{YFP} fluorescence intensity facilitates the enrichment of self-renewing astroglial cells from the neonatal PWM niche.

(A-C) Sagittal sections of $Tnc^{YFP\text{-}CreER}$ cerebella showing the absence of Tnc expression as marked by YFP in VZ at P2 (A, A') and in $Pax2^+$ GABAergic progenitors of PWM at P5 (B). Tnc expression is rarely detected in astrocytes (C, white arrowhead). (D-F) FACS was performed on dissociated P3 wild-type cerebella (no Tnc^{YFP}) (D), dissociated Tnc^{YFP+} 2^o neurospheres (E) or dissociated P3 $Tnc^{YFP\text{-}CreER}$ cerebella (F). Dot plots show forward scatter plotted on the y-axis and YFP fluorescence detection on the x-axis, used to set gating for YFP^+ (green) versus YFP^- cells (black). Distinct populations from dissociated P3 $Tnc^{YFP\text{-}CreER}$ cerebella revealed by Tnc^{YFP} fluorescence intensity (F); Tnc^{YFP-} cells (black), $Tnc^{YFP\text{-}low}$ cells (blue), and $Tnc^{YFP\text{-}high}$ cells (red). (G) Surface plot measurement of Tnc^{YFP} signal intensity using grey scale values from a confocal optical slice of YFP staining depicted below in **H**, indicating distinct Tnc^{YFP} signals for Bergmann glia (high) and PWM astroglia (low). FCS, forward scatter. Scale bars indicate 25 μm.

Distinct Shh-responding astroglial subpopulations are revealed by $Tnc^{YFP\text{-}low}$ expression

Because Shh-responsive, $Tnc^{YFP\text{-}low}$ cells display attributes of cerebellar NSCs, we tested them for expression of CD133, an established NSC marker in the postnatal cerebellum (Lee et al., 2005). We found that only a small fraction of $Tnc^{YFP\text{-}low}$ cells express CD133 at P3 using flow cytometric analysis (<0.5%) (**Figure 3.7N**, boxed in Q2). Given that a subset of Shh-responding cells also express NSC-associated surface antigen CD15 (**Figure 3.1F**), the distribution of CD133 and CD15 was evaluated amongst $Tnc^{YFP\text{-}low}$ cells (**Figure 3.7N**, blue population). This combinatorial marker analysis clearly distinguished astroglial subpopulations at P5 that are either **1)** $Tnc^{YFP\text{-}low}$ $CD133^+$ (gold), **2)** $Tnc^{YFP\text{-}low}$ $CD15^+$ (purple), or **3)** $Tnc^{YFP\text{-}low}$ $CD133^-$ $CD15^-$ (blue) (**Figure 3.7O**, <2.5%, <0.5% or >97%, of $Tnc^{YFP\text{-}low}$ cells, respectively). Consistent with our above data we found that $Tnc^{YFP\text{-}low}$ $CD15^+$ cells exhibit Shh pathway activation as measured by *Gli1* expression, but also found that $Tnc^{YFP\text{-}low}$ $CD133^+$ cells respond to Shh (**Figure 3.7P**).

We next evaluated the respective NSC attributes of the above three $Tnc^{YFP\text{-}low}$ astroglial subpopulations *in vitro*, as well as the top 20% of $Tnc^{YFP\text{-}high}$ cells. Consistent with previous studies (Lee et al., 2005), $TNC^{YFP\text{-}low}$ $CD133^{+}$ cells generated neurospheres, but, to our surprise, so did $Tnc^{YFP\text{-}low}$ $CD15^{+}$ cells, $Tnc^{YFP\text{-}low}$ $CD133^{-}$ $CD15^{-}$ cells, and $Tnc^{YFP\text{-}high}$ cells, which expressed the same gamut of NSC markers (**Figure** 3**.8A-L**). Similar to previous studies, we observed progressively limited self-renewal with each passage (1/16-1/27 neurospheres/ cells plated)(Lee et al., 2005). However, when subjected to multi-lineage differentiation, all $CD133^{-}$ astroglial subpopulations predominantly generated astrocytes and displayed very limited neurogenic potential with no apparent GABA or glutamatergic marker expression (**Figure** 3**.8M-Q**). These findings suggest that all $CD133^{-}$ cells are restricted progenitors lacking the full repertoire of NSC characteristics. Collectively, our data indicate the PWM is comprised of multiple Shh-responding, functionally and antigenically divergent progenitors, and distinguishes previously unappreciated astroglial subpopulations.

Shh maintains PWM proliferation and GABAergic progenitor expansion

We next sought to determine the specific requirement for Shh signaling in $Tnc^{YFP\text{-}low}$ cells *in vivo* during the early neonatal period. Because Shh signaling is required for the proliferation of radial glial cells in the cerebellar VZ during embryogenesis (Huang X. et al., 2010), we decided to use inducible $Tnc^{YFP\text{-}CreER}$ mice to temporally ablate Shh-responsiveness in the PMW. To gauge Shh-responsiveness in the PWM following Smoothened (Smo) deletion with consecutive TM administrations on P1 and P2, we utilized the $Gli1^{nlacZ}$ reporter strain and noted qualitatively fewer $\beta\text{-gal}^{+}$ cells at P3 and P4 in PWM of $Tnc^{YFP\text{-}CreER}$; $Gli1^{nlacZ}$; $Smo^{F/-}$ mice versus littermate controls (**Figures** 3**.9A**, **B** and 3**.10A, B**). At P5, $Tnc^{YFP\text{-}low}$ cells were isolated from cerebella of

wild-type *Tnc*$^{YFP\text{-}CreER}$ and *Tnc*$^{YFP\text{-}CreER}$*; Smo*$^{F/-}$ littermates using FACS, and RT-PCR for *Gli1* mRNA confirmed attenuation of Shh signaling in mosaic mutant Tnc$^{YFP\text{-}low}$ cells (**Figure 3.10C, D**).

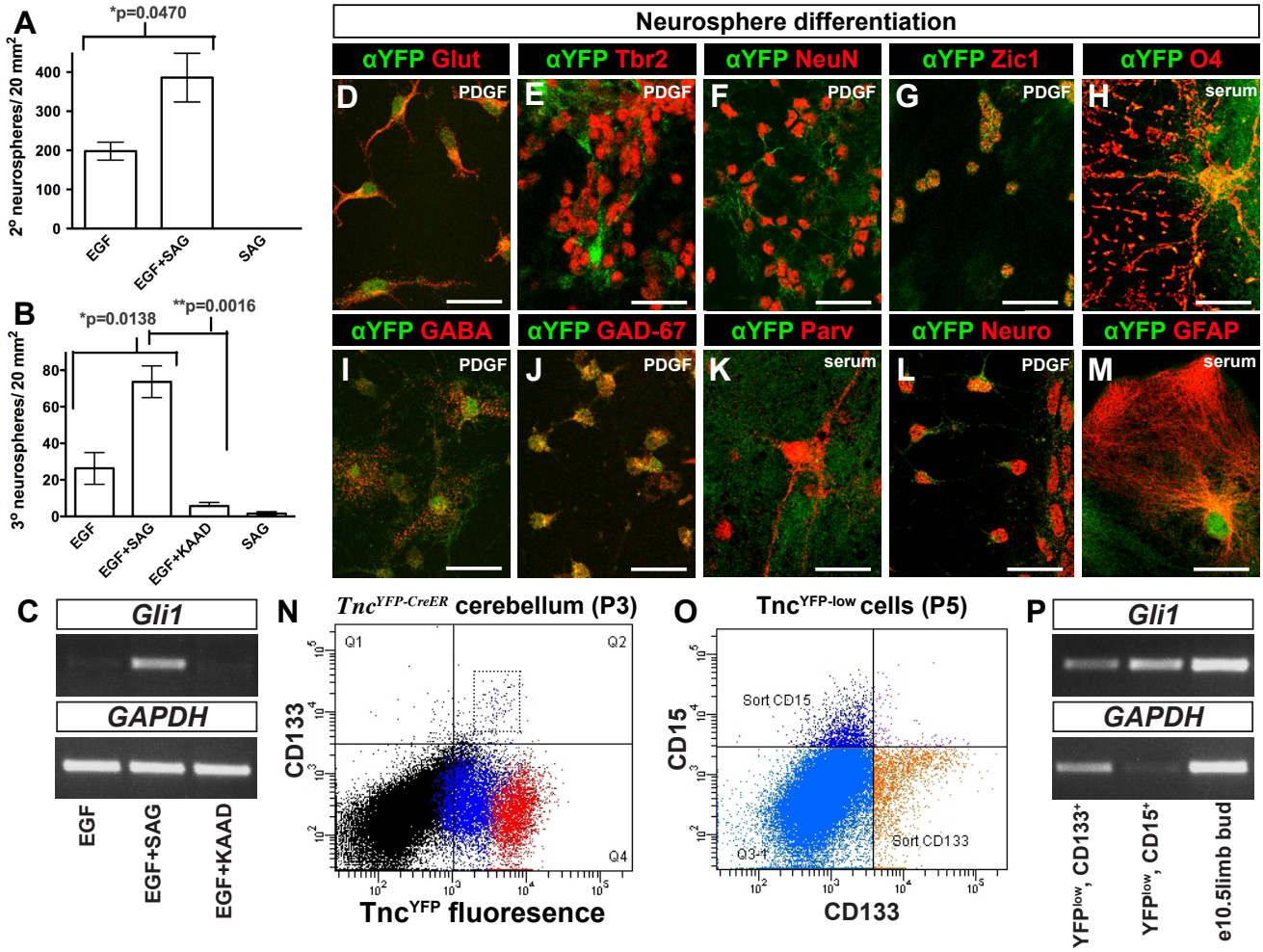

Figure 3.7. Shh promotes self-renewal of multi-potent Tnc$^{YFP\text{-}low}$ astroglia, which include molecularly distinct subpopulations.

(A-B) 2^{o} (A) and 3^{o} (B) neurospheres were generated from Tnc$^{YFP\text{-}low}$ cerebella and neurosphere formation were quantified following treatment with 25ng/ml EGF alone, 20nM SAG w/ EGF, 10nM KAAD cyclopamine w/ EGF or SAG alone for 10 days (n=3). SAG significantly augmented neurosphere-forming capacity of EGF. Additionally, neurosphere formation is dependent on Shh signaling as Smo inhibitor KAAD-cyclopamine inhibited neurosphere formation (B). (**C**) RT-PCR for *Gli1* and *GAPDH* using total RNA from treatment groups in **B**. (D-M) Tnc$^{YFP\text{-}low}$-derived 2^{o} neurospheres can differentiate into diverse array of cell types including glutamatergic neurons (D-G), GABAergic neurons (I-L), oligodendrocytes (H) and astrocytes (M) when exposed to serum or PDGF for 10 days. Glutamate (Glut), Tbr2, NeuN and Zic1 are markers of glutamatergic neurons; GABA, GAD-67, Neurograinin (Neuro) are markers of GABAergic neurons; O4 and GFAP are markers of oligodendrocytes and astrocytes, respectively. (N-O) Dot plot from FACS analysis showing distribution of CD133^{+} cells amongst all Tnc^{YFP} cells at P3 (N), and distribution of CD133^{+} and CD15^{+} cells in the Tnc$^{YFP\text{-}low}$ population at P5 (O). Note that Tnc$^{YFP\text{-}low}$, CD133^{+} cells (boxed) represents < 0.5%. (P) *Gli1* is expressed in both Tnc$^{YFP\text{-}low}$, CD133^{+} and Tnc$^{YFP\text{-}low}$, CD15^{+} subpopulations as indicated by RT-PCR. *GAPDH* was used as an internal control and e10.5 limb bud was used as a positive control for *Gli1* expression. Error bars are presented as SEM, and p value relative to control samples indicated. Scale bars indicate 25 μm.

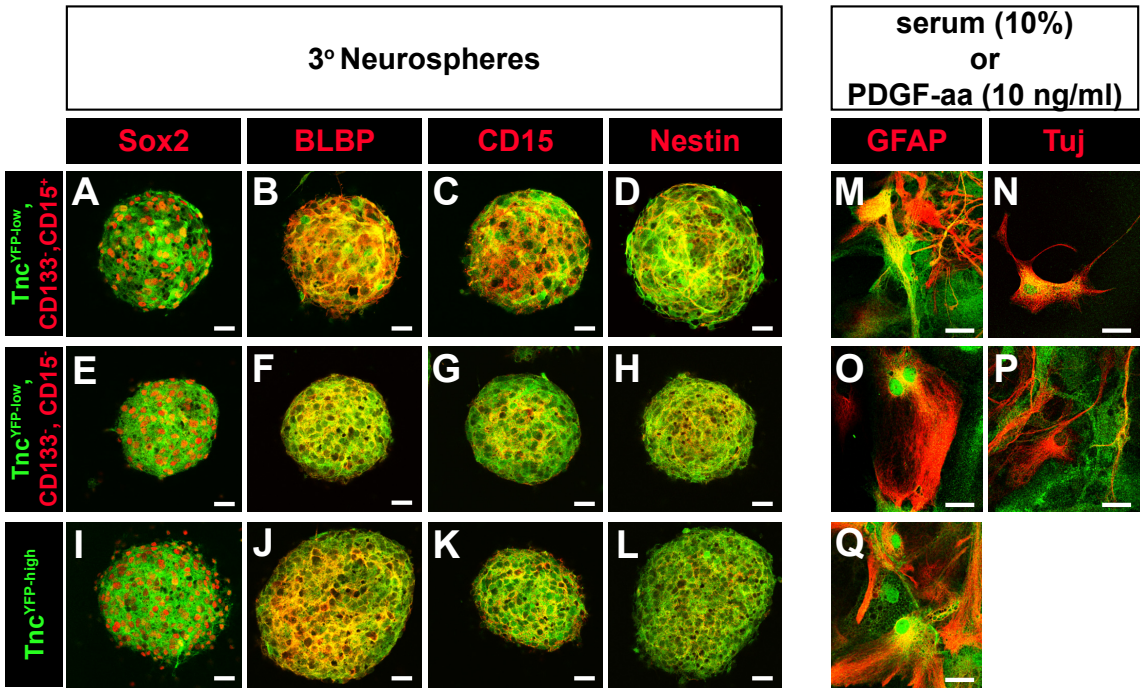

Figure 3.8. Molecularly distinct Tnc^{YFP} subpopulations generate neurospheres but exhibit limited differentiation potential.

(A-L) NSC marker Sox2 (A, E, I), BLBP (B, F, J), CD15 (C, G, K) and Nestin (D, H, L) expression by 3^{o} neurospheres derived from three distinct, FACS-purified Tnc^{YFP}, CD133- populations; (i) Tnc$^{YFP\text{-}low}$ CD15^{+} CD133^{-} (A-D), (ii) Tnc$^{YFP\text{-}low}$ CD15^{-} CD133^{-} (E-H) and (iii) Tnc$^{YFP\text{-}high}$ (I-L). (M-Q) Forced differentiation of 3^{o} neurospheres derived from the above-mentioned populations with serum or PDGF-aa for 10 days. Note that all CD133^{-} astroglial subpopulations predominantly generated astrocytes and displayed very limited neurogenic potential with no apparent GABA or glutamatergic marker expression. Scale bars indicate 25 μm.

We first focused our analysis on the extensive cellular proliferation occurring in the PWM at P5 following a 2 hour BrdU pulse, at which time presumably one-half of the GABA progenitor pool has been born (Weisheit et al., 2006). A large fraction of acutely dividing cells in normal cerebellum are $Sox2^+$ (**Figure 3.9C, C'**), and consistent with our finding that Shh stimulation can enhance the sphere-forming capacity of $Tnc^{YFP\text{-}low}$ cells (**Figure 3.7A, B**), there was a significant reduction in the fraction of dividing $Sox2^+$ cells in the PWM of the $Tnc^{YFP\text{-}CreERT2}$; $Smo^{F/-}$ cerebellum (ROI I: 28.92%, ROI II: 19.55%, ROI III: 18.24%, ROI IV: 29.73%, n=3) (**Figure 3.9C-D', M**). Reductions in proliferation were not accompanied by increased cell death (**Figure** 3**.10E**).

Subsequent analyses were focused on $Ptf1a^+$ and $Pax2^+$ cells in PWM between P5-P7, by which time the majority (75%) of the latter have been born (Weisheit et al., 2006). Reductions were apparent in these populations at P5 and P7, respectively (ROI I: 35%, ROI II: 18%, ROI III: 44%, ROI IV: 69%, n=3 and ROI I: 31%, ROI II: 30%, ROI III: 23%, ROI IV: 29%, n=4) (**Figure** 3**.9E-H, N, O**). When total $Pax2^+$ cell number was measured (versus the regional number above), it was considerably reduced (18.31%, n=4), precluding that a failure in migration of $Pax2^+$ cells contributed to reductions in regional pools (**Figure** 3**.9P**).

Additionally, the $Ai9^{F/+}$ reporter strain was used to more closely approximate the contribution of the Tnc-lineage to PWM $Pax2^+$ progenitor pools under normal conditions ($Tnc^{CreERT2}$; $Ai9^{F/+}$) and attenuated Shh signaling ($Tnc^{CreERT2}$; $Ai9^{F/+}$; $Smo^{F/-}$). Indeed, ablation of Smo disrupted the capacity of $Tnc^{YFP\text{-}low}$ cells for generating GABAergic precursors; $Tnc^{YFP\text{-}CreER}$; $Ai9^{F/+}$; $Smo^{F/-}$ cerebella had substantially reduced $Pax2^+$, $tdTomato^+$ (62.4%) and $Ptf1a^+$, $tdTomato^+$ (33%)

double-positive cells at P7 (per 20 um^2 of PWM) (**Figure 3.9I, J** and 3**.10F, G**). The reduction in $Pax2^+$, $tdTomato^+$ cells is unlikely due to lower recombination efficiency of the reporter in mutant cells because similar numbers of $tdTomato^+$, Tnc^{YFP+} double-positive Bergmann glia are observed between control and mutant (89.8±1% versus 92.1±0.8%, **Figure** 3**.105H**). However, such extensive labeling of internal control cells likely over-estimates *Smo* deletion. Consistent with reduced $Pax2^+$/ $Ptf1a^+$ cells, we observed a substantial loss (30.6%) of basket and stellate GABAergic interneurons at P30 (per 20 um2 of ML) (**Figure 3.9K, L, Q)** Collectively, these data demonstrate the importance of Shh signaling for the establishment of a neurogenic niche in the PWM.

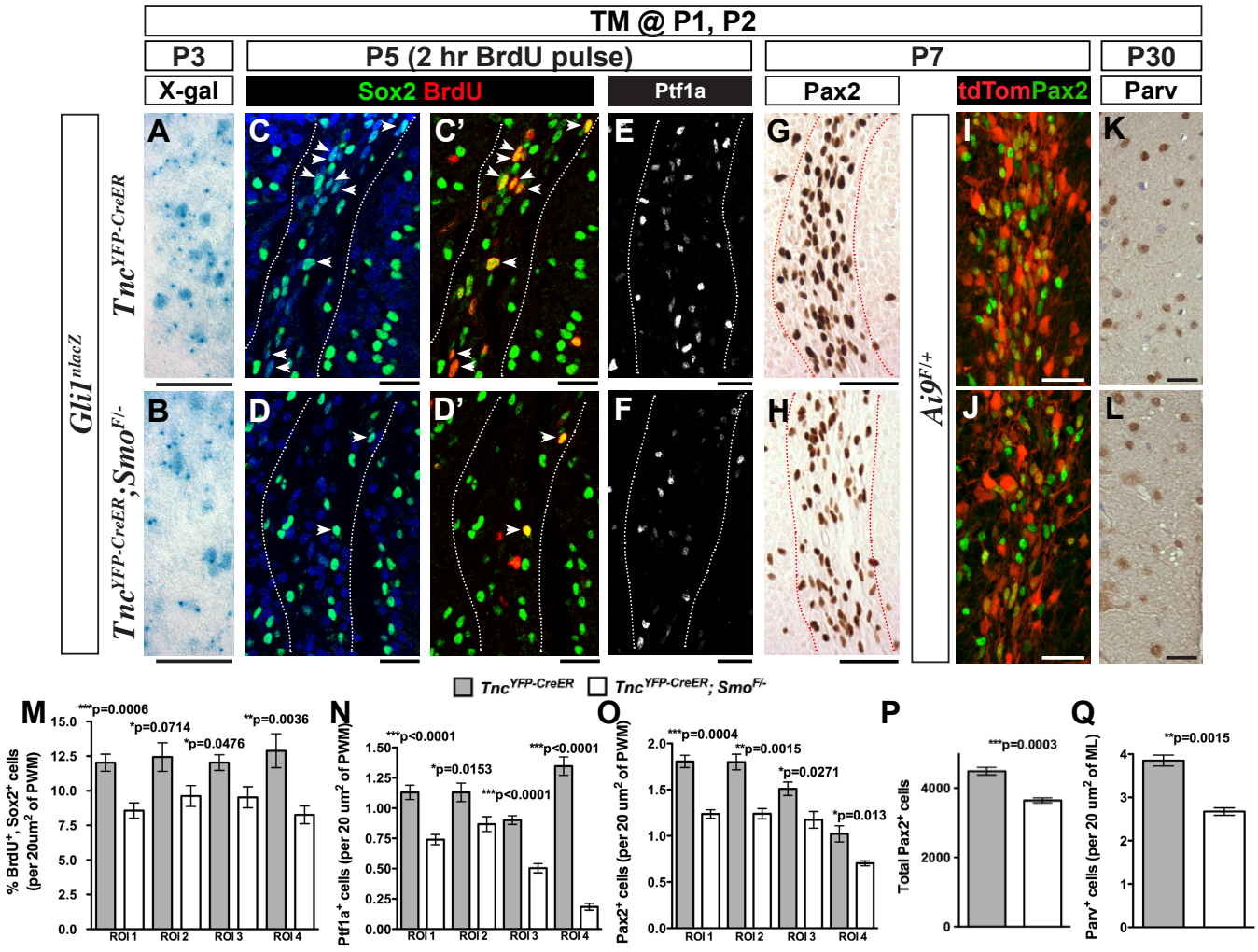

Figure 3.9. Shh signaling supports proliferation and expansion of GABAergic interneuron progenitors in PWM domains.

(A-L) Analysis of *Tnc*$^{YFP\text{-}CreER}$ and *Tnc*$^{YFP\text{-}CreER}$*; Smo*$^{F/-}$ cerebella from mice injected with TM on P1, P2 and analyzed at P3 (A, B), P5 (C-F), P7 (G-J) or P30 (K, L) with either the *Gli1*^{nlacZ} (A-H) or *Ai9*$^{F/+}$ (I-L) reporter. Gli1 expression as detected by X-gal is reduced in PWM of P3 *Tnc*$^{YFP\text{-}CreER}$*; Smo*$^{F/-}$ *Gli1*^{nlacZ}*; Smo*$^{F/-}$ cerebella when compared to the control *Tnc*$^{YFP\text{-}CreER}$*; Gli1*^{nlacZ} (A, B). Similarly, Brdu^{+} Sox2^{+} (C-D'), Ptf1a^{+} (E, F), Pax2^{+} (G, H, I, J) and Parv^{+} (K, L) cells are also significantly reduced in the mutants. (M-Q) Quantitative analyses of BrdU^{+}, Sox2^{+} cells over total Sox2^{+} cells (M), Ptf1a^{+} cells (N), Pax2^{+} cells (O), total Pax2^{+} cells (P) and Parv^{+} cells (Q) in *Tnc*$^{YFP\text{-}CreER}$ (grey bar) and *Tnc*$^{YFP\text{-}CreER}$*; Smo*$^{F/-}$ (open bar) cerebella. All the analyses were performed on 5 to 10 sections per brain and with three or four animals per genotype. Error bars are presented as SEM, and p value relative to control samples indicated. White dotted lines demarcate the PWM, white arrowheads indicate double-labeled cells. Scale bars indicate 25 μm.

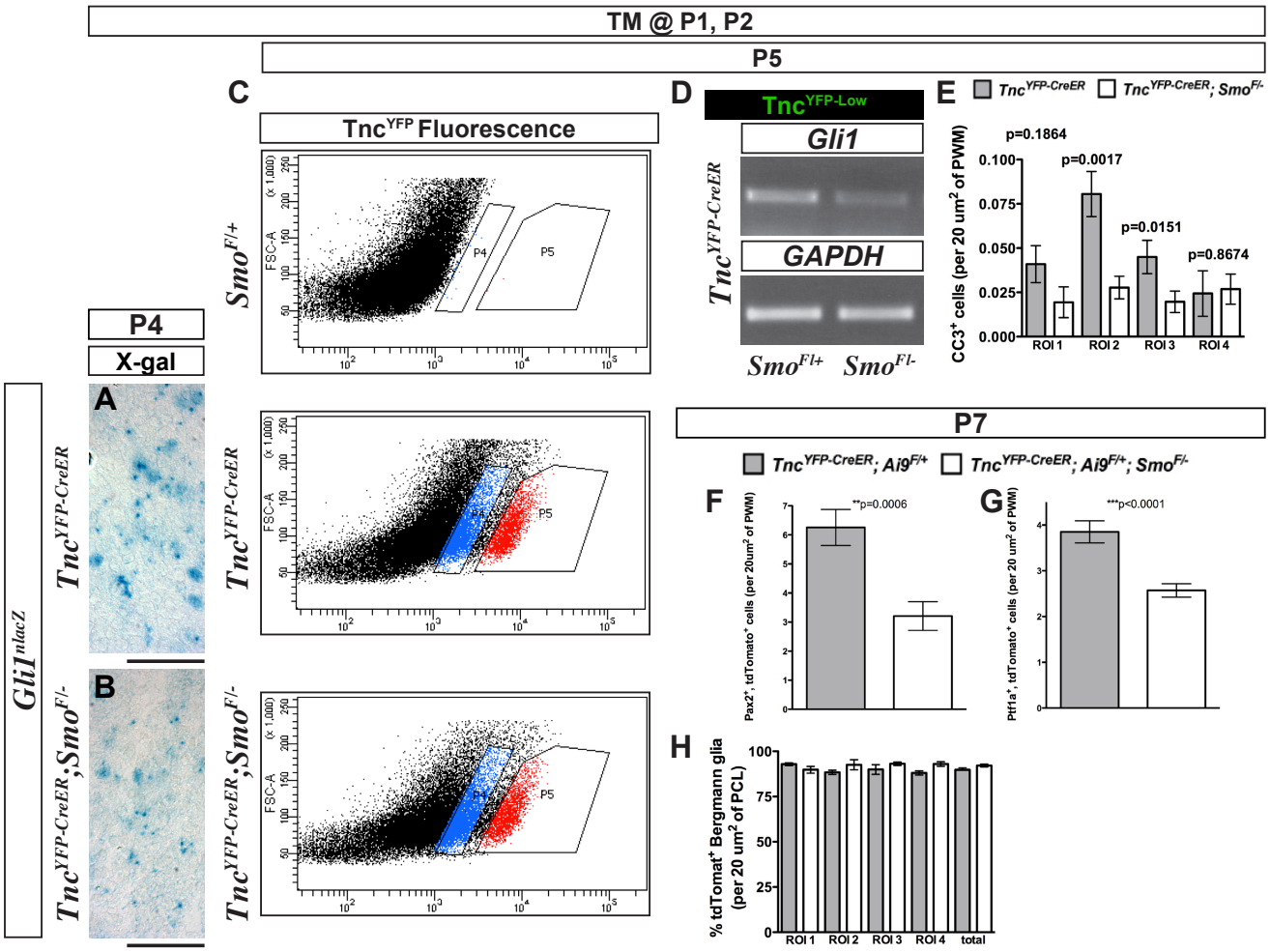
TM @ P1, P2
P5
C
Tnc^YFP Fluorescence
Smo^F/+
Tnc^YFP-CreER
Tnc^YFP-CreER;Smo^F/-
P4
P5
D
Tnc^YFP-Low
Gli1
GAPDH
Tnc^YFP-CreER
Smo^Fl+
Smo^Fl-
E
Tnc^YFP-CreER
Tnc^YFP-CreER; Smo^F/-
p=0.1864
p=0.0017
p=0.0151
p=0.8674
CC3+ cells (per 20 um2 of PWM)
ROI 1
ROI 2
ROI 3
ROI 4
P4
X-gal
A
B
Gli1^nlacZ
P7
Tnc^YFP-CreER; Ai9^F/+
Tnc^YFP-CreER; Ai9^F/+; Smo^F/-
F
**p=0.0006
Pax2+, tdTomato+ cells (per 20um2 of PWM)
G
***p<0.0001
Ptf1a+, tdTomato+ cells (per 20 um2 of PWM)
H
% tdTomat+ Bergmann glia (per 20 um2 of PCL)
ROI 1
ROI 2
ROI 3
ROI 4
total

Figure 3.10. Attenuation of Shh pathway activity after Smo ablation in Tnc$^{YFP\text{-}low}$ cells.

(A, B) X-gal detection for β-galactosidase activity in PWM of P4 *Tnc$^{YFP\text{-}CreER}$; Gli1^{nlacZ}* or *Tnc$^{YFP\text{-}CreER}$; Gli1^{nlacZ}; Smo$^{F/-}$* cerebella from mice that received TM on P1, P2. Gli1 expression as detected by X-gal is reduced in PWM of P4 *Tnc$^{YFP\text{-}CreER}$; Smo$^{F/-}$ Gli1^{nlacZ}; Smo$^{F/-}$* cerebella (B) when compared to the control *Tnc$^{YFP\text{-}CreER}$; Gli1^{nlacZ}* (A). (C) Tnc^{YFP} fluorescence intensity from FACS; dot plots of dissociated P5 cerebella from *Smo$^{F/+}$*, *Tnc$^{YFP\text{-}CreER}$*, and *Tnc$^{YFP\text{-}CreER}$; Smo$^{F/-}$* mice that received TM on P1 and P2. Forward scatter is plotted on the y-axis and YFP detection is on the x-axis. Black color indicates cells regarded as Tnc$^{YFP\text{-}}$, blue indicates Tnc$^{YFP\text{-}low}$, and red indicates Tnc$^{YFP\text{-}high}$ status. (D) Attenuation of Shh-responsiveness was evident in *Smo$^{F/-}$* mutant, Tnc$^{YFP\text{-}low}$ cells indicated by RT-PCR for *Gli1*. *GAPDH* was used as an internal control. (E) Quantitative analysis of cleaved-caspase 3 (CC3)$^{+}$ cells in *Tnc$^{YFP\text{-}CreER}$* (grey bar) and *Tnc$^{YFP\text{-}CreER}$; Smo$^{F/-}$* (open bar) cerebella indicated cell viability is not compromised in the PWM following Smo ablation. (F-H) Cerebella from *Tnc$^{YFP\text{-}CreER}$; Ai9$^{F/+}$* (grey bar) and *Tnc$^{YFP\text{-}CreER}$; Smo$^{F/-}$; Ai9$^{F/+}$* (open bar) mice that received TM on P1, P2 and were analyzed at P7 for (F) Pax2^{+}, tdTom^{+}, (G) Ptf1a^{+}, tdTom^{+} cells, and (H) Tnc^{YFP+}, tdTom^{+} Bergmann glia. All the analyses were performed on 5 to 10 sections per brain and with three or four animals per genotype. Error bars are presented as SEM, and p value relative to control samples indicated. Scale bars indicate 25 μm unless otherwise stated. FCS, forward scatter.

Shh promotes expansion of CD15^{+} astrocyte precursors in lobular PWM domains

Because Tnc$^{YFP\text{-}low}$ CD15^{+} cells were overwhelmingly gliogenic *in vitro* (**Figure** 3**.8**) we sought to further evaluate their developmental potential *in vivo*. Although flow cytometry indicated that CD15^{+} cells represent a small fraction of Tnc$^{YFP\text{-}low}$ cells at P5 (<0.5%) (**Figure 3.7O**), we found broad distribution of CD15 in the lobular PWM at P7. We first examined whether CD15 marks oligodendrocytes or their precursors at the latter stage. We did not find convincing co-expression with MBP, which was largely restricted to core PWM (DCN) near the 4th ventricle (**Figure 3.11A, A'**). Analysis of oligodendrocyte precursor cell marker Sox10 (Stolt et al., 2002) showed no definitive overlap with CD15 in neither core nor lobular PWM (**Figure 3.11B, C**), and revealed that Sox10^{+} cells persist in the PWM of *Tnc$^{YFP\text{-}CreER}$; Smo$^{F/-}$* mutants (**Figure 3.11B, C** versus **D, E**). These data are consistent with our Gli1-GIFM, which indicated Gli1^{+} cells do not generate oligodendrocytes in the postnatal period, and with previous transplantation and chick-

quail chimeric studies that showed cerebellar OPCs largely arise from extracerebellar regions during embryogenesis (Grimaldi et al., 2009; Mecklenburg et al., 2011).

However, this analysis did reveal that expansion of $CD15^+$ cells in lobular PWM is heavily dependent on Shh signaling: in $Tnc^{YFP\text{-}CreER}$; $Smo^{F/-}$ mutants $CD15^+$ cells fail to accumulate in these regions (**Figure 3.11B** versus **D**). Interestingly, we found frequent co-expression between CD15 and GFAP (**Figure 3.11F**), suggesting that $Tnc^{YFP\text{-}low}$ $CD15^+$ cells may be intermediate astrocyte precursors. These data demonstrate the importance of Shh activity we detected earlier in β-gal^+, $CD15^+$ cells in $Gli1^{nlacZ}$ cerebella (**Figure 3.1F**) and in FACS-purified $Tnc^{YFP\text{-}low}$ $CD15^+$ cells at P5 (**Figure 3.7P**). Because we did not observe β -gal^+ cells in the core PWM in $Gli1^{nlacZ}$ cerebella (at either P3, P5 or P6), we were not surprised to find that CD15 expression there was largely unaffected in $Tnc^{YFP\text{-}CreER}$; $Smo^{F/-}$ mutants (**Figure 3.11C** versus **E**). However, in lobular PWM at P7 the accumulation of $GFAP^+$ cells was markedly reduced (37% overall, n=3) in $Tnc^{YFP\text{-}CreER}$; $Smo^{F/-}$ mutants (**Figure 3.11F** versus **H** and **G** versus **I, J**), implicating Shh as a major driver in the generation of cerebellar astrocytes via a $Tnc^{YFP\text{-}Low}$ $CD15^+$ intermediate progenitor.

To assess whether $CD15^+$ PWM cells descend from a $CD133^+$ primary progenitor, CD133-GIFM with TM administered to *CD133-CreER; $Ai9^{F/+}$* mice at P1 and P2 was performed. At P7 that PWM $CD15^+$ cells have descended from a $CD133^+$ parent population, similar to astrocytes and $Pax2^+$ cells (**Figure 3.11K-M**). Additionally, at P21, CD133-GIFM cells generate many cerebellar cell types, including ML GABAergic interneurons and various astrocyte populations (**Figure 3.11N, O**). However, we never observed that CD133-GIFM cells contribute to

Bergmann glia, which are born prior to E14.5 (Sudarov et al., 2011) (**Figure 3.11P**). These data support a lineage relationship between $Tnc^{YFP\text{-}low}$ $CD133^{+}$ primary progenitors with intermediate astrocyte precursors ($Tnc^{YFP\text{-}low}$ $CD15^{+}$) and transient amplifying GABAergic progenitors ($Ptf1a^{+}$)

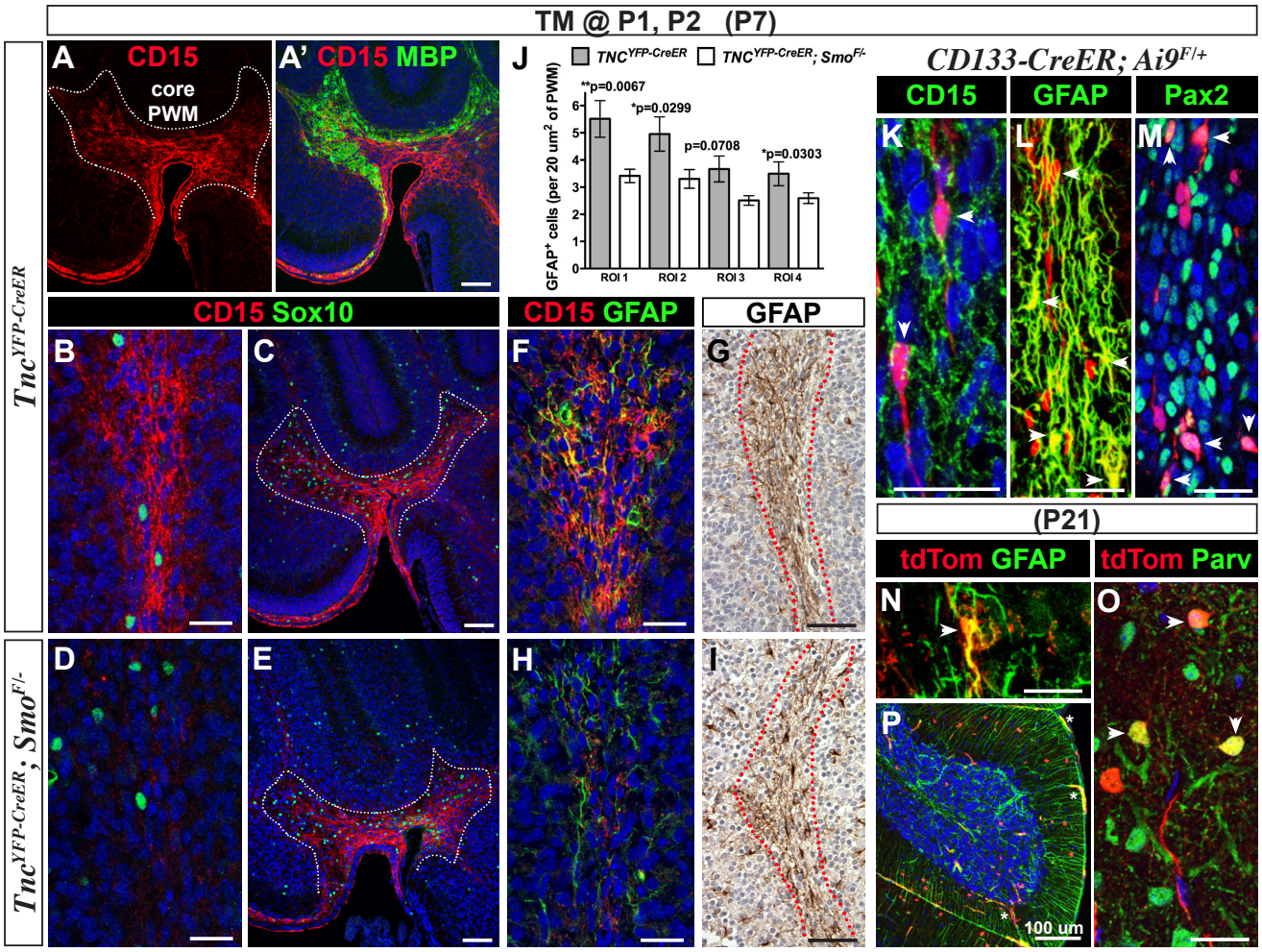
TM @ P1, P2 (P7)
Tnc^YFP-CreER
Tnc^YFP-CreER; Smo^F/-
A
CD15
core
PWM
A' CD15 MBP
J
TNC^YFP-CreER
TNC^YFP-CreER; SmoF/-
**p=0.0067
*p=0.0299
p=0.0708
*p=0.0303
GFAP+ cells (per 20 um2 of PWM)
ROI 1
ROI 2
ROI 3
ROI 4
CD133-CreER; Ai9F/+
CD15
GFAP
Pax2
K
L
M
CD15 Sox10
B
C
CD15 GFAP
F
GFAP
G
(P21)
tdTom GFAP
tdTom Parv
N
O
D
E
H
I
P
100 um

Figure 3.11 Shh signaling promotes expansion of CD15$^+$ intermediate astrocyte precursors, lineally related to CD133$^+$ PWM neuronal stem cells.

(**A-I**) Control *Tnc$^{YFP\text{-}CreER}$* (A-C, F, G) and mutant *Tnc$^{YFP\text{-}CreER}$; Smo$^{F/-}$* (D, E, H, I) mice were injected with TM on P1, P2 and cerebella were stained with CD15 (A-F, H), Sox10 (B-E) and GFAP (F-I) at P7. CD15 expression is broadly distributed in the core and lobular PWM (A, B) and does not represent oligodendrocytes as revealed by the lack of co-localization with MBP (A') or Sox10 (C) expression. In *Tnc$^{YFP\text{-}CreER}$; Smo$^{F/-}$* mutants, only the lobular (B, D) but not the core (C, E) CD15 expression is drastically reduced, whereas Sox10 expression remains unaffected (C, E). Accordingly, the expression of astrocyte marker GFAP is reduced in the mutants (F-I). Red dotted lines in G and I indicate PWM. (**J**) Quantitative analysis of GFAP$^+$ cells in *Tnc$^{YFP\text{-}CreER}$* (grey bar) and *Tnc$^{YFP\text{-}CreER}$; Smo$^{F/-}$* mutant (open bar) cerebella. All the analyses were performed on 5 to 10 sections per brain and with four animals per genotype. Error bars are presented as SEM, and p value relative to control samples indicated. (**K-P**) Lineage analysis of CD133$^+$ cells in the cerebellum. *CD133-CreER; Ai9$^{F/+}$* mice received TM on P1 and P2, analyzed at P7 (K-M) and P21 (N-P). CD133$^+$ cells contribute broadly to diverse cell types including CD15$^+$ precursors (K), GFAP$^+$ astrocytes (L, N), Pax2$^+$ progenitors (M) and Parv$^+$ GABA interneurons (O, P). Asterisks indicate endothelial cells. Scale bars indicate 25 μm.

PN-derived Shh signals distantly to maintain the PWM niche

We previously reported that CSF-derived Shh promotes radial glial proliferation in the embryonic cerebellar VZ (Huang X. et al., 2010). Though it is unlikely this transventricular signaling could reach the lobular PWM, cerebellar PNs express Shh and extend axons deep into the cortex by the end of embryogenesis (Lewis P.M., 2004; Sillitoe et al., 2009). Our analysis with *Shh^{Cre}; mT/mG* mice clearly indicated PN axons descend through PWM at P3 (**Figure 3.12A**). These projections bring PNs into close proximity with otherwise distant Sox2$^+$ cells (**Figure 3.12B**), suggesting a plausible means of disseminating Shh over this distance. Indeed, we were able to detect puncta of Shh ligand distributed throughout the lobular PWM at P3-P4, in a pattern similar to that observed in the EGL, while the strongest signal was concentrated around the soma of Shh-producing PNs (**Figure 3.12C-D'**).

To determine if Shh produced by PNs does indeed activate Shh signaling to maintain the PWM niche, Shh signaling in PMW cells was robustly blocked using the PN-specific *L7-Cre* transgenic driver to remove Shh function starting at e17.5, without affecting embryonic VZ function (Lewis P.M., 2004). We analyzed *L7-Cre; $Shh^{F/-}$*; *$Gli1^{nlacZ}$* cerebella and observed a dramatic loss of Shh signaling as evidenced by considerable loss of PWM β-gal$^+$, Sox2$^+$ (double-positive) cells compared to *$Gli1^{nlacZ}$* littermates (**Figure 3.12E** versus **F**). Accordingly, the fraction of S-phase Sox2$^+$ cells was significantly reduced in *L7-Cre; $Shh^{F/-}$* PWM at P5 (ROI I: 25%, ROI II: 47%, ROI III: 29%, ROI IV: 28%, n=3) (**Figure 3.12G'** versus **I', K**). These results indicate that PN-derived Shh ligand strongly supports a proliferative compartment in the PWM.

We next evaluated the capacity of PN-derived Shh to promote neurogenesis by measuring local Pax2$^+$ populations within the PWM. Indeed, these progenitors were considerably reduced in *L7-Cre; $Shh^{F/-}$* mice at P5 (ROI I: 25%, ROI II: 47%, ROI III: 29%, ROI IV: 28%, n=3) (**Figure 3.12H** versus **J, L**). This aberration was even more pronounced for total Pax2$^+$ cell number, which was dramatically reduced (46.15%, n=3, **Figure 3.12M**). These changes were not accompanied by increases in cell death. In fact, decreases in cell death were evident, possibly due to the substantial loss of GABAergic progenitors (46.15%), some of which are known to normally undergo cell death in the PWM (Yamanaka et al., 2004).

PN-derived Shh supports the generation of multiple GABAergic interneuron subtypes

Birth-dating studies have shown that PNs are generated early, from E10.5 to E12.5, whereas GABAergic interneurons are generated during late embryogenesis through the first week of postnatal life (Altman J, 1997). Consistent with this observation, PN number is largely

unaffected in *L7-Cre; Shh*$^{F/-}$ mutants (Lewis P.M., 2004) whereas the number of Parvalbumin^{+} basket and stellate cells in the ML was significantly reduced at P30 (**Figure** 3**.12N** and 3**.13A, B** versus **C, D**). Interestingly, an earlier-born GABAergic interneuron subtype, Golgi cells, which reside in the IGL and selectively express Neurogranin, were also reduced (**Figure** 3**.13E, F** versus **G, H, J**). We did not find that Golgi cells were marked by our Gli1, Ptf1a, Tnc, or CD133-GIFM experiments, likely owing to the proposed perinatal birth-date for this cell type (Sudarov et al., 2011). These results indicate that PN-derived Shh is a common driver for the generation of numerous GABAergic interneuron subtypes.

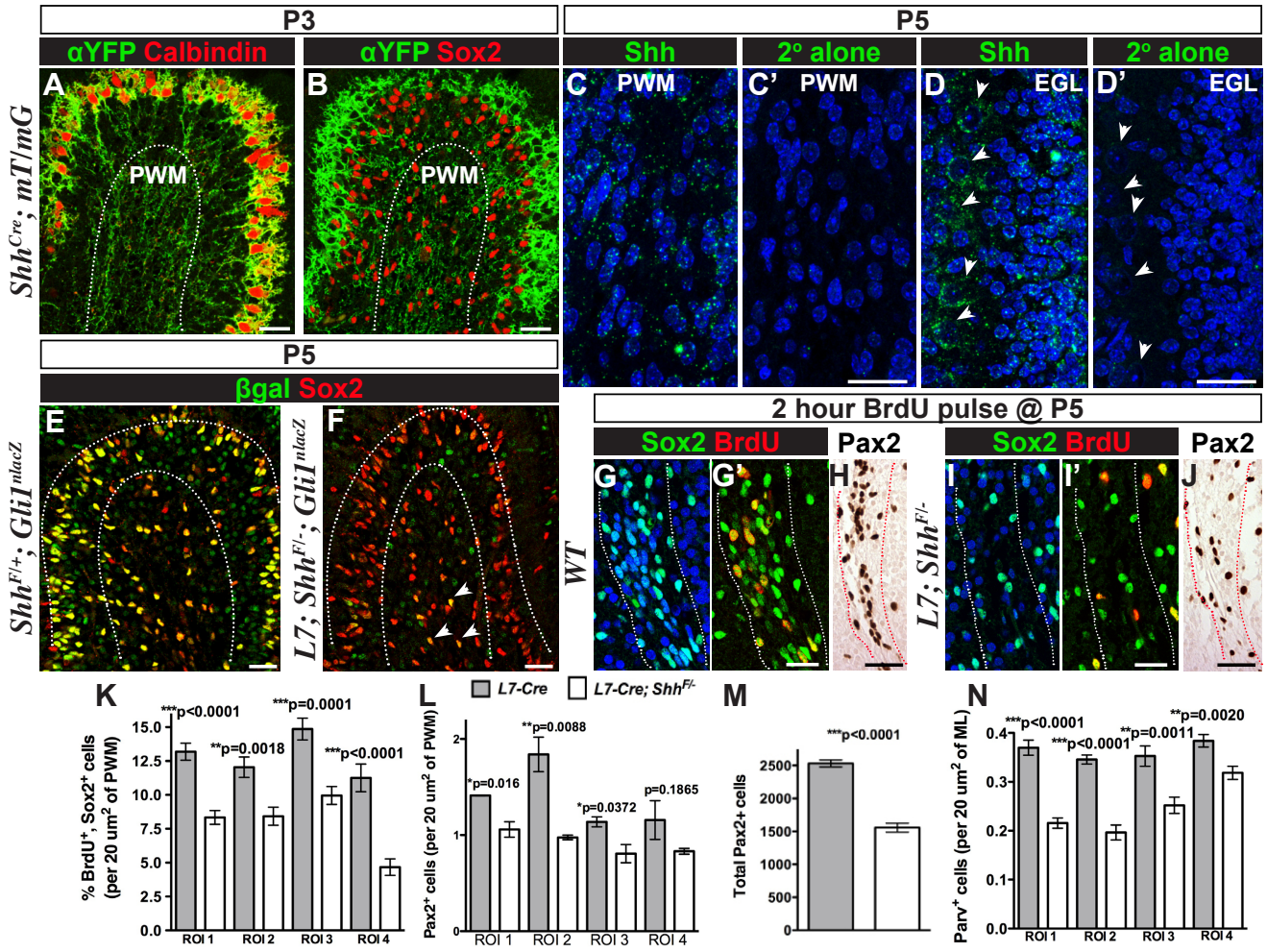
P3
P5
αYFP Calbindin
αYFP Sox2
Shh
2° alone
Shh
2° alone
A
B
C
C'
D
D'
PWM
PWM
PWM
EGL
EGL
Shh^Cre; mT/mG
P5
βgal Sox2
2 hour BrdU pulse @ P5
Sox2 BrdU
Pax2
Sox2 BrdU
Pax2
E
F
G
G'
H
I
I'
J
Shh^F/+; Gli1^nlacZ
L7; Shh^F/-; Gli1^nlacZ
WT
L7; Shh^F/-
K
% BrdU+, Sox2+ cells (per 20 um2 of PWM)
***p<0.0001
**p=0.0018
***p=0.0001
***p<0.0001
ROI 1
ROI 2
ROI 3
ROI 4
L
L7-Cre
L7-Cre; Shh^F/-
Pax2+ cells (per 20 um2 of PWM)
*p=0.016
**p=0.0088
*p=0.0372
p=0.1865
ROI 1
ROI 2
ROI 3
ROI 4
M
Total Pax2+ cells
***p<0.0001
N
Parv+ cells (per 20 um2 of ML)
***p<0.0001
***p<0.0001
**p=0.0011
**p=0.0020
ROI 1
ROI 2
ROI 3
ROI 4

Figure 3.12. Purkinje neuron-derived Shh signals distantly to maintain the PWM niche.

(**A, B**) Sagittal sections of P3 *Shh^{Cre}; mT/mG* cerebella showing PN cell body (Calbindin), PN axons (YFP) and astroglia (Sox2) in the PWM. (**C-D'**) Distribution of Shh protein (green) in PWM and EGL of P3 sagittal cerebellar sections. Nuclei are counterstained with To-pro3 iodide (blue). Note that Shh protein is concentrated around the PN soma (white arrowheads). (**E, F**) Shh signaling as revealed by β-galactosidase antibody staining is significantly reduced in *L7-cre; Shh$^{F/-}$; Gli1^{nlacZ}* mutant cerebella when compared to of control *Shh$^{F/+}$; Gli1^{nlacZ}* at P5. Inner white dotted line demarcates PWM, whereas outer dotted line indicates Bergmann glia. (**G-J**) In contrast to control, *L7-cre; Shh$^{F/-}$* mice show drastic reduction of proliferating Sox2^{+} cells (G, G', I, I') and Pax2^{+} progenitors (H, J) at P5 following a 2hr BrdU pulse. Staining for markers indicated. PWM is delineated by white dotted lines (**G, G', I, I'**) and red dotted lines (**H, J**). (**K-N**) Quantitative analyses of BrdU^{+}, Sox2^{+} cells (K), Pax2^{+} cells (L, M) and Parv^{+} cells (N) in *L7-cre* (grey bar) and *L7-cre; Shh$^{F/-}$* (open bar) cerebella. All the analyses were performed on 5 to 10 sections per brain and with three animals per genotype. Error bars are presented as SEM, and p value relative to control samples indicated. Red dotted lines demarcates the PWM. Scale bars indicate 25 μm. PWM, presumptive white matter.

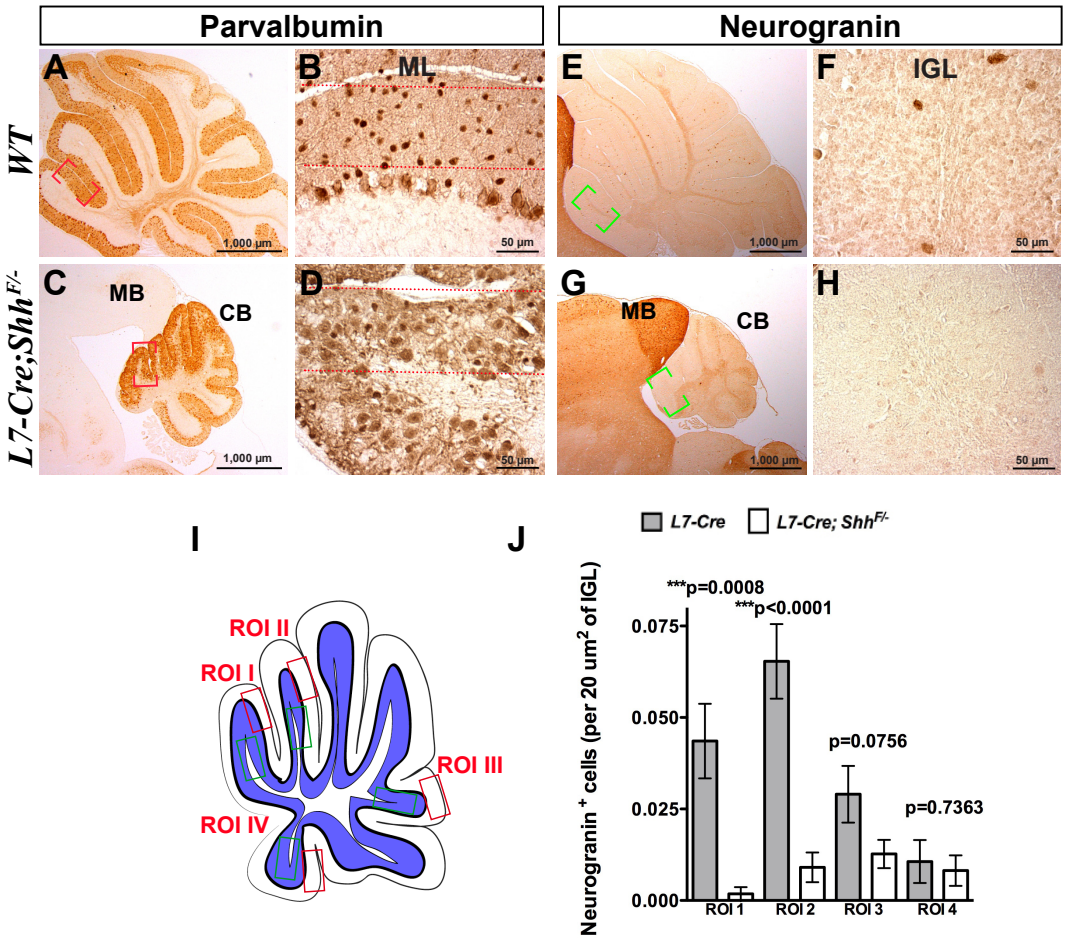

Figure 3.13 Paucity of mature GABAergic interneurons results from loss of PN-derived Shh.

(**A-H**) Sagittal sections of cerebella from control (A, B, E, F) and *L7-Cre; Shh*$^{F/-}$ (C, D, G, H) littermates, showing reduced numbers of GABAergic inhibitory interneurons at P30. Staining for Parvalbumin (**A-D**) and Neurogranin (**E-H**). (**I**) Schematic indicating regions used for analysis of ML (red boxes) or IGL (green boxes). (**J**) Quantitative analysis of internal granule layer (IGL) Golgi inhibitory interneurons. All the analyses were performed on 5 to 10 sections per brain and with three or four animals per genotype. Error bars are presented as SEM, and p value relative to control samples indicated. Scale bars indicate 25 µm. Abbreviations: CB, cerebellum; MB, midbrain; ML, molecular layer.

Postnatal expansion of GABAergic progenitors is independent of cerebellar growth

Because deletion of Shh from PNs substantially disrupts cortical expansion of the cerebellum (Lewis P.M., 2004), this approach could impair neurogenesis in the PWM indirectly via reduction of GCPs. To resolve this issue, we ablated Shh-responsiveness specifically from proliferative, *Atoh1*-expressing GCPs by TM administration at P1 and P2 (**Figure 3.14A, A'**) and analyzed local $Pax2^+$ pools at P7. First, as expected, the *Atoh1-Cre^{ER}; Smo$^{F/-}$* EGL exhibited substantially less proliferation (**Figure 3.14B, B'** versus **D, D'**). However, despite severe cerebellar hypoplasia (**Figure 3.14C** versus **E**), $Pax2^+$ cell numbers were not decreased (n=3, **Figure 3.14C, C'** versus **E, E'** and **F**). Together our findings indicate that GABA neurogenesis in the PWM is not linked to expansion of GCPs and global cerebellar growth, and that it proceeds normally when the latter processes are disrupted.

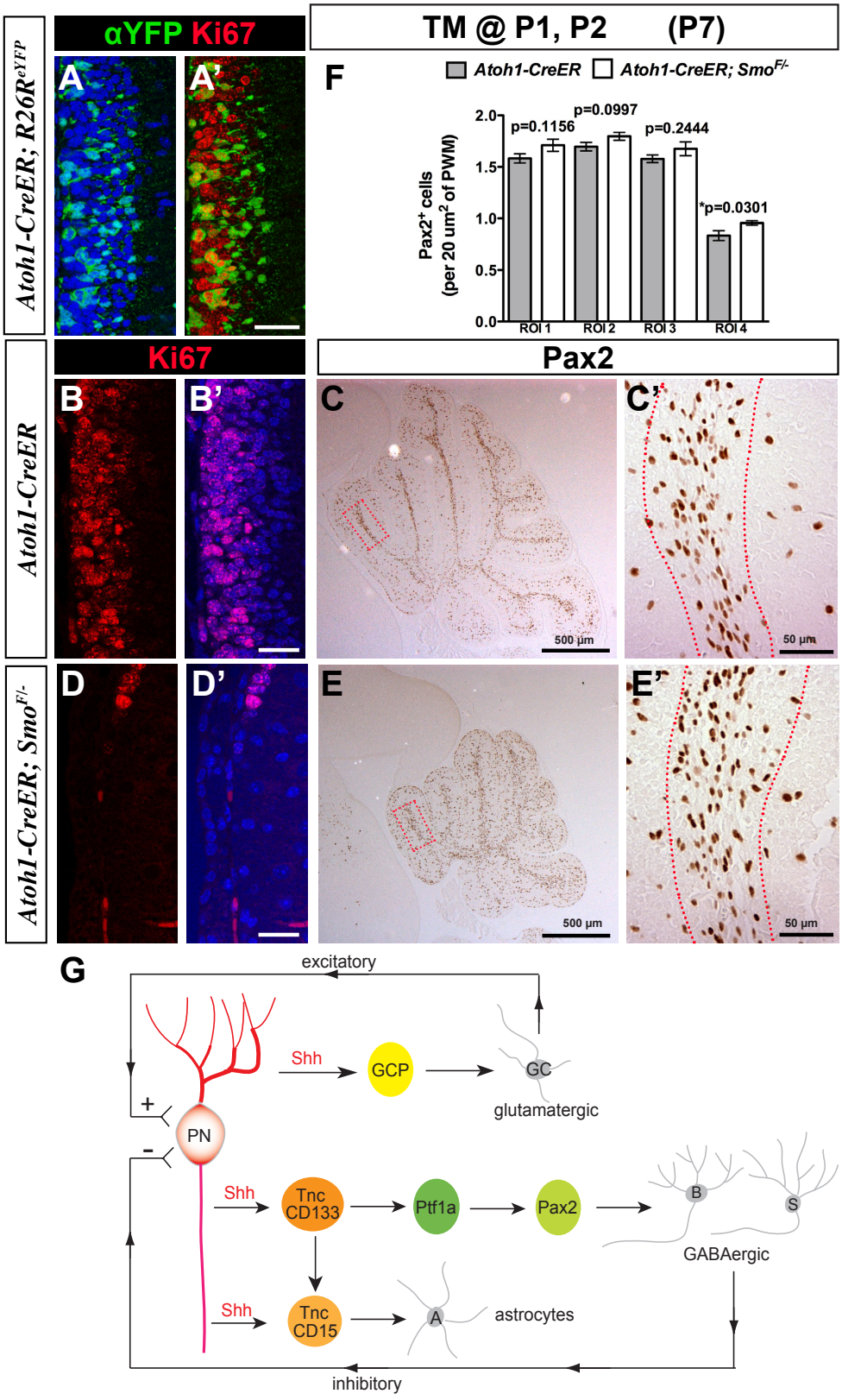
Atoh1-CreER; R26R^eYFP
αYFP Ki67
A
A'
TM @ P1, P2 (P7)
F
Atoh1-CreER
Atoh1-CreER; Smo^F/-
p=0.1156
p=0.0997
p=0.2444
*p=0.0301
Pax2+ cells (per 20 um2 of PWM)
2.0
1.5
1.0
0.5
0.0
ROI 1
ROI 2
ROI 3
ROI 4
Ki67
Pax2
B
B'
C
C'
D
D'
E
E'
500 μm
50 μm
G
excitatory
Shh
GCP
GC
glutamatergic
PN
+
-
Shh
Tnc CD133
Ptf1a
Pax2
B
S
GABAergic
Shh
Tnc CD15
A
astrocytes
inhibitory

Figure 3.14 Cerebellar hypoplasia does not affect GABA neurogenesis in the PWM niche.

(**A, E'**) Analysis of *Atoh1-creER^{T2}; R26R^{eYF}* (**A-A'**), *Atoh1-creER* (**B-C'**) and *Atoh1-creER; Smo$^{F/-}$* (**D-E'**) cerebella from littermates injected with tamoxifen at P1, P2 and analyzed at P7. (**A-A'**) Sagittal section of *Atoh1-creER^{T2}; R26R^{eYF}* showing efficient recombination in the EGL. (B-D') Number of Ki67^{+} cells in the EGL (B, B', D, D') but not Pax2^{+} progenitors (C, C', E, E') are drastically reduced in *Atoh1-creER; Smo$^{F/-}$* when compared to *Atoh1-creER* control. (**F**) Quantification of regional Pax2^{+} cells shows the development of GABAergic interneuron progenitors are not affected in *Atoh1-creER; Smo$^{F/-}$* mutants. Red dotted lines demarcate the PWM. Scale bars indicate 25 μm unless otherwise stated. Error bars are presented as SEM, and p value relative to control samples indicated. (**G**) Model of postnatal cerebellar neurogenesis. By sending Shh bi-directionally, Purkinje neurons (PN) simultaneously modulate the numbers of both excitatory and inhibitory interneurons, which originate in distant, spatially segregated progenitor domains. This model posits that the neonatal PWM niche is comprised of lineally-related, but molecularly and functionally divergent progenitor subpopulations, which descend from a Tnc$^{YFP\text{-}low}$ CD133^{+} primary progenitor. Within this niche, we show that Ptf1a^{+} GABAergic progenitors and Tnc$^{YFP\text{-}low}$ CD15^{+} astrocyte precursors are proliferative. This model was conceived based on clonal analysis of CD133^{+} PWM cells transplanted into neonatal cerebella (Lee et al., 2005) in combination with our own fate-mapping of Gli1^{+}, Ptf1a^{+}, Tnc^{+}, and CD133^{+} cells. GCP denotes granule cell precursors.

Discussion

The work presented here demonstrates that the PWM niche contains molecularly distinct subpopulations with divergent developmental potentials (broad lineage, neurogenic and astrocytic). These progenitor subpopulations commonly respond to Shh, which robustly promotes the propagation of their respective progeny. Finally, we found that PN-Shh maintains a bi-directional signaling axis that simultaneously promotes EGL-based cortical expansion and maintenance of the PWM niche. These results, together with previous studies, demonstrate that PNs are a central signaling node, modulating both inhibitory and excitatory neuronal cell numbers. Perturbations to the generation of these functionally distinct subpopulations as the result of PN dysfunction may have important implications for human neurodevelopmental disorders rooted in excitatory/ inhibitory imbalance.

Shh signals to molecularly and functionally distinct populations of PWM progenitor cells

Previous studies have suggested that astroglia marked by human GFAP promoter activity in the postnatal cerebellum contribute to both neurons and astrocytes (Silbereis et al., 2009). Our studies suggest that these astroglia are the major Shh-responding population in the PWM, whereas the cerebellar VZ no longer responds to Shh and is mitotically inactive. These astroglia not only express markers characteristic of NSCs, but their descendents, analyzed through Gli1-GIFM analysis, contribute broadly to cerebellar architecture, generating distinct GABAergic interneuron as well as astrocyte subtypes. Shh-responding astroglia are heterogeneous as they can be sorted into two populations based on Tnc^{YFP} reporter levels. As shown previously for *Tnc* mRNA expression (Yuasa, 1996), Tnc^{YFP} is expressed in both PCL and PWM, but not in the postnatal cerebellar VZ (**Figure** 3**.6A, A'**). The majority of glial cells associated with $Tnc^{YFP\text{-}high}$ likely represent Bergmann glia, as they are the most abundant glial population expressing strong *Tnc*. Indeed, the Tnc^{YFP} expression profile in cerebellar sections indicated that fluorescence intensity is much higher in Bergmann glia than in PWM astroglia (**Figure** 3**.6G, H)**.

The $Tnc^{YFP\text{-}low}$ population can be further separated into three molecularly distinct subpopulations based on expression of NSC-associated surface antigens, CD133 and CD15. We found that The $Tnc^{YFP\text{-}low}$ $CD133^{+}$ cells are the most broadly potent Shh-responding population in the PWM. These primary progenitors and their descendent cells, analyzed through Gli1, Ptf1a, Tnc, and CD133-GIFM analyses, contribute broadly to cerebellar architecture, generating distinct GABAergic interneurons and astrocytes. $Tnc^{YFP\text{-}low}$ $CD133^{+}$ cells display the full repertoire of NSC attributes, similar to $CD133^{+}$/ $lineage^{-}$ NSCs (Lee et al., 2005). Unlike these previously reported cerebellar NSCs (Lee et al., 2005), we found that Shh signaling and EGF synergize to

promote self-renewal of $Tnc^{YFP\text{-}low}$ cells, similar to the synergism of Shh - EGF reported for postnatal SVZ NSCs (Palma et al., 2005).

Unlike $Tnc^{YFP\text{-}low}$ $CD133^{+}$ cells, both $Tnc^{YFP\text{-}low}$ $CD15^{+}$ and $Tnc^{YFP\text{-}low}$ $CD133^{-}$ $CD15^{-}$ populations gave rise predominantly to astrocytes in culture. Collectively, our data (including CD133-GIFM) along with clonal analysis of $CD133^{+}$/ $lineage^{-}$ NSCs (Lee et al., 2005), suggest these latter populations represent stages along a progenitor lineage derived from more broadly potent $Tnc^{YFP\text{-}low}$ $CD133^{+}$ primary progenitors (**Figure 3.14G**). However, additional *in vivo* clonal analysis is required to demonstrate that intermediate astrocyte ($Tnc^{YFP\text{-}low}$ $CD15^{+}$) and GABAergic interneuron ($Ptf1a^{+}$) precursors are derived from a common $Gli1^{+}$ $Tnc^{YFP\text{-}low}$ $CD133^{+}$ astroglial primary progenitor.

The neurosphere-forming capacity of $Tnc^{YFP\text{-}low}$ $CD133^{-}$ populations was unanticipated but is not surprising, because restricted progenitors can also generate neurospheres *in vitro* (Kondo and Raff, 2000; Temple, 2001). Our work indicates that $Tnc^{YFP\text{-}low}$ $CD15^{+}$ cells are intermediate astrocyte precursors, and are functionally divergent from $CD15^{+}$ cells in the EGL (Ashwell and Mai, 1997; Read et al., 2009). Given that CD15 marks NSCs in the embryonic and adult SVZ (Capela and Temple, 2002; Solter and Knowles, 1978), our observation that $Tnc^{YFP\text{-}low}$ $CD15^{+}$ cells are restricted progenitors was somewhat unexpected, providing insight into the function of $CD15^{+}$ cells in other neurogenic niches.

Though Tnc^{YFP} cells display two distinct reporter levels, $Tnc^{YFP\text{-}high}$ Bergmann glial cells are spatially isolated from the proliferative PWM niche and lack CD133 expression. Additionally,

Tnc^{YFP}, similar to *Tnc* mRNA (Yuasa, 1996), is not expressed in the postnatal cerebellar VZ (**Figure 3.6A, A'**). Thus, $Tnc^{YFP\text{-}low}$ cells are the only relevant population in the context of neurogenesis/ gliogenesis occurring in the postnatal PWM. Unlike Bergmann glia, these $Tnc^{YFP\text{-}low}$ cells respond to Shh only transiently, suggesting Shh signaling is actively inhibited after P6. Recently, it was shown that Wnt signaling is activated in the PWM at postnatal stages (Selvadurai and Mason, 2011) and when ectopically activated Wnt signaling disrupts self-renewal in neonatal $CD133^{+}$/ $lineage^{-}$ NSCs (Pei et al., 2012). Therefore, it is possible that Wnt is antagonistic to Shh activity in the PWM, analogous to that proposed elsewhere for cerebellar GCPs (Lorenz et al., 2011).

Ptf1a marks transient amplifying progenitors of GABAergic interneurons

Late–born GABAergic interneurons are estimated to represent ~90% of all inhibitory interneurons in the cerebellum, and the majority of their progenitors, marked by Pax2 expression, are generated during the first week of postnatal life (Weisheit et al., 2006). Recent studies have shown that Pax2 expression is upregulated at the final progenitor cell division (Leto et al., 2009; Weisheit et al., 2006), and thus, a mechanism must exist to account for the vast numbers of $Pax2^{+}$ cells generated during this brief window. Although $Pax2^{+}$ cells can be traced to astroglia (Silbereis et al., 2009), it is unlikely that proliferation of astroglia alone is sufficient to expand the vast $Pax2^{+}$ pools. Our analyses demonstrated not only that $Pax2^{+}$ cells descend from $Ptf1a^{+}$ cells, but also that the latter are transient, intermediate progenitors that appear to drive the rapid expansion of $Pax2^{+}$ pools. This role for Ptf1a is distinctly different from its previously reported function in GABA lineage allocation, in which it acts to potently suppress glutamatergic fate (Hoshino et al., 2005; Pascual et al., 2007).

Purkinje neurons are a bi-directional signaling center

PNs are recognized by elaborate dendritic arbors, through which Shh is likely disseminated to the EGL, driving transient proliferation of GCPs (Lewis P.M., 2004). Our present study indicates that Shh from PNs is also necessary for maintenance of the distant PWM niche, where we propose that it targets distinct progenitor populations, including $Tnc^{YFP\text{-}low}$ $CD133^{+}$ primary progenitors, $Ptf1a^{+}$ GABA-intermediate and $Tnc^{YFP\text{-}low}$ $CD15^{+}$ astrocyte-intermediate progenitors (**Figure 3.14G**). While PNs are a common source of Shh ligand for both the EGL and PWM, our study indicated that direct perturbation of GCP proliferation did not impact GABAergic progenitor expansion, suggesting that cortical growth has little (if any) immediate impact on maintenance of the PWM.

Several recent studies suggested an atypical mode of Shh delivery to target sites, utilizing axons as a vehicle (Brownell et al., 2011; Garcia et al., 2010; Ihrie et al., 2011; Traiffort et al., 2001). This delivery mechanism was first noted in *Drosophila* in which Hh is transported along retinal axons to the brain (Huang and Kunes, 1996). Our study suggests a similar mechanism of Shh delivery from PNs to PWM targets, but extends this concept further by suggesting that Shh-producing neurons can promote neurogenesis along different axes. A bi-directional signaling mechanism has also been proposed for Brain-derived neurotrophic factor (BDNF) in neurons where it is transported along neuritic processes to axons and dendrites (von Bartheld et al., 1996). Interestingly, differential neuronal activity appears to modulate BDNF release from the axon and dendrite (Matsuda et al., 2009). Future studies are required to determine the mechanism of bi-directional Shh transport to the target fields.

One intriguing question raised by our study is why would PNs be charged with the complex task of regulating the simultaneous production of both inhibitory and excitatory interneurons? Some insight may be gained from the physiological function of PNs, the sole projection neurons in the cerebellar circuit. They integrate direct excitatory input from, in part, parallel fibers of granule neurons simultaneously with inhibitory input from basket and stellate cells (and Golgi cells indirectly), and relay cerebellar output via their projections to the DCN (Sillitoe and Joyner, 2007). Because the balance between inhibitory and excitatory neurons is critical for modulating precise neuronal output from PNs, we speculate that PNs represent a sentinel population governing the formation of neural circuitry by synchronizing the balanced generation of inhibitory and excitatory interneurons. Because the cerebellum has been linked to neurodevelopmental disorders associated with excitatory/ inhibitory imbalance, such as the autism spectrum disorders (ASD), in which neuropathologies associated with PNs have been widely noted (Catini et al., 2008; Palmen et al., 2004; Pierce and Courchesne, 2001; Tsai et al., 2012), this study provides an important contribution toward a greater understanding of neural network assembly

CHAPTER IV

ONCOGENIC SHH SIGNALING VIA GLI2 IS SUFFICIENT TO DRIVE FORMATION OF EWING'S SARCOMA-LIKE TUMORS INDEPENDENTLY OF EWS-FLI1

Introduction

Sarcomas represent a heterogeneous spectrum of tumors affecting numerous soft tissues, including muscle, fat, ligaments, and even bone. Though many sarcomas target the pediatric population, a few subtypes are restricted to adults (Lessnick et al., 2009). Nearly ubiquitous among sarcomas is the characteristic small round cell morphology, making the identification of other defining features necessary to discern sarcoma subtype (Fletcher et al., 2013; Lessnick et al., 2009). Markers of differentiation can be utilized to discriminate some sarcomas. The rhabdomyosarcoma (RMS) family, for example, is comprised of multiple tumor entities that display a spectrum of myogenic differentiation, which has led to wide spread suspicion that RMS originates in myogenic precursor cells (Kikuchi et al., 2011). This myogenic signature for RMS (determined by a Myogenin$^+$, MyoD$^+$, or Desmin$^+$ status) has served as a reliable diagnostic tool for clinicians.

However, molecular markers with such clear diagnostic power are yet to be defined for most other sarcoma variants, which lack a clear line of differentiation (Fletcher et al., 2013). The specific factors acting to drive such divergent sarcoma phenotypes are not known, but cellular origin and mutational profile appear to be powerful, influential forces (Kikuchi et al., 2011; Rubin et al., 2011). A major impediment towards developing new diagnostic markers for non-

RMS tumors has likely been the lack of faithful, genetically inducible mouse models. In particular, the Ewing's family of tumors (EFT) has been especially difficult to reproduce in mice. EFT includes extraosseous small round cell sarcomas (SRCS), those that affect bone, and peripheral neuro-ectodermal tumors (PNTs). Currently, the defining characteristic of this family is a chromosomal translocation at t(12;22)(q24;q12), resulting in the EWS1-FLI1 chimeric oncoprotein (Lessnick et al., 2009). Attempts to generate an EFT mouse model based on EWS1-FLI1 have not been successful (Haldar et al., 2009; Lin et al., 2008; Torchia et al., 2007), and were likely confounded by the inherent lethality of oncogenic translocations (Haldar et al., 2007; Haldar et al., 2009; Straessler et al., 2013). Furthermore, even though >95% of EFT are associated with t(12;22)(q24;q12), the drivers of EFT sarcomagenesis downstream of the EWS1-FLI1 oncoprotein have not been established (Lessnick et al., 2009; McAllister and Lessnick, 2005).

Several recent EFT studies have reported elevated expression of GLI1, a transcriptional activator of Sonic hedgehog (Shh) pathway target genes, and have described transcriptional regulation of GLI1 by EWS1-FLI1 (Beauchamp et al., 2009; Joo et al., 2009; Sankar et al., 2013; Zwerner et al., 2008). These findings are intriguing because aberrant activation of the Shh pathway by either deletion of the receptor, Ptch1, or activation of the signaling transducer, Smo, are sufficient to drive formation of RMS in numerous mouse models to date; but have not led to the formation of EFT (Hahn et al., 1998; Hatley et al., 2012; Mao et al., 2006; Nitzki et al., 2011; Rubin et al., 2011). We chose to postulate whether GLI2, the primary activator of Shh target genes (Corrales et al., 2006), rather than GLI1, is regulated by EWS-FLI1 and if this relationship could be an important mechanism underlying EFT formation.

To test whether activated GLI2 function alone is sufficient to drive sarcomagenesis, a truncated human GLI2 (GLI2ΔN) that lacks an N-terminal repressor domain and thus functions as a constitutive activator was used. The *CLEG2* allele, which encodes GLI2ΔN under control of the CAG promoter, has been demonstrated to function as a potent driver of basal cell carcinoma (Pasca di Magliano et al., 2006; Roessler et al., 2005). *CLEG2* was targeted to multipotent mesenchymal progenitors using L7(*Pcp2)-cre*, and 100% of mice (termed *PCG2*) formed SRCS. *PCG2* tumors were highly aggressive soft tissue sarcomas that expressed Nkx2.2, an emerging molecular marker for EFT and known Shh target gene (Smith et al., 2006; Vokes et al., 2007; Yoshida et al., 2012). Moreover, the gene expression profile of *PCG2* sarcomas shows a strong correlation with a large cohort of human EFT samples. Enrichment of EWS-FLI1 binding in two ~1.8 kb regions of human GLI2 suggests a direct EWS-FLI1 – GLI2 interaction may underlie EFT etiology. Altogether, *PCG2* mice represent an EFT-like model, suggesting that Gli2 is sufficient to drive sarcomagenesis independent of EWS-FLI1, and that EFTs arise from the mesenchymal lineage.

Experimental Procedures

Animals

All experiments were performed using young neonatal and adult animals, ages P3 – 1.5 years according to the NIH and VUMC Division of Animal Care.

Mice of the following genetic lines, of either sex, were used: *Gli1*^{nlacZ} (Bai C.B., 2002) *L7(PCp2)-Cre* (Lewis P.M., 2004), *R26R*^{eYFP} (Srinivas S., 2001), *Ai9* (Madisen et al., 2010), *Pax7-creER* (Murphy et al., 2011), *Myf5*^{Cre} (Haldar et al., 2007), *aP2-cre* (Urs et al., 2006),

Ptch^{lacZ} (Goodrich et al., 1997), *CLEG2* (Pasca di Magliano et al., 2006), and *SmoM2* (Mao et al., 2006).

Tissue processing, protein isolation, immunohistochemistry, and western blotting

Tissues were dissected out and fixed in 4% paraformaldehyde for either 4-6 hours or O/N at 4^{o} C, and were either processed for frozen embedding in OCT compound or processed for paraffin embedding. Frozen tissues were sectioned on a Leica cryostat at 10 um, paraffin embedded tissues were cut at 5 um. Protein was isolated from fresh or snap-frozen tumor and tibialis anterior muscle using standard lysis buffer, and a BCA assay (Thermo) was used for measuring concentration.

Antibodies

Immunohistochemistry (IHC) and immunocytochemistry (ICC) were performed as previously described (Huang X. et al., 2010). The following primary antibodies were used to perform IHC on frozen and/ or paraffin tissue sections: chicken α-βGal (ICL), mouse α-BrdU (DSHB), mouse α-CyclinD1 (DSHB), mouse α-Desmin (DSHB), chicken α-GFP (Aaves), rabbit α-Gli1 (Cell Signaling), rabbit α-Gli2 (Gift of Jonathan EggenSchwiler, Phd, UGA), rabbit α-Ki67 (NeoMarkers), mouse α-Laminin (Thermo), mouse α-Myc (DSHB), mouse α-Myogenin (DSHB), rabbit α-Myogenin (EPITOMICS), mouse α-Myf5 (DSHB), mouse α-MyoD (DSHB), mouse α-Nkx2.2 (DSHB), mouse α-Pax7 (DSHB), mouse α-Pax3 (DSHB), rabbit α-PDGFRα (Thermo), rabbit α-PPARγ (Cell Signaling), mouse α-tubulin (DSHB), mouse α-Vimentin (NeoMarkers). For bright-field staining, species-specific HRP-conjugated secondary antibodies (Invitrogen) were used followed by incubation in DAB reaction (Invitrogen). Double-labeling

fluorescence immunohistochemistry was performed using species-specific, AlexaFluor-tagged secondary antibodies Alexa 488, Alexa 568 and Alexa 647 (Invitrogen) followed by counterstaining with To-pro3 iodide (Invitrogen).

X-gal staining and transcript detection

X-gal staining for β-galactosidase activity was performed on post-fixed, frozen sections according to standard protocols. The following cDNAs were used as templates for synthesizing digoxygenin-labeled riboprobes: *Gli1*.

Gene expression profiling and Statistical analyses

RNA from tumor and unaffected tibialis muscle (n=3 animals) was isolated using a two-step protocol in which tissue was homogenized in Trizol and RNA was collected by phenol-chloroform extraction and column elution with RNeasy Mini kit (Qiagen). RNA was reverse transcribed to create a cDNA library by the VANTAGE core at VUMC prior to paired-end sequencing on the Illumina platform. We first performed quality control on raw data to identify potential outliers before doing any advanced analysis by applying tool FastQC. RNA data alignment was performed by TopHat (Trapnell et al., 2009), gene quantification was done by Cufflinks (Trapnell et al., 2010). Unsupervised cluster analysis based on Pearson's correlation coefficient on all genes shows clear separation between muscle and tumor samples. RPKM (reads per kilobase per million reads) based approaches with Cuffdiff (Trapnell et al., 2010) were used to detect differential expressed genes. False discovery rate (FDR < 0.05) was used for multiple test correction.

Microarray

External similarity analysis was conducted using the data set GSE9103, GSE12102 (Scotlandi et al., 2009) and GSE37371 from Gene Expression Onmibus. GSE9103 was generated from a skeletal muscle transcript profiling study which contains 40 vastus lateralis muscle biopsy samples: 10 young sedentary, 10 older sedentary, 10 young trained, 10 older trained. GSE9103 acted as normal samples in this analysis. Tumor counterparts were obtained from GSE12102 and GSE37371. GSE12102 contained 37 and GSE37371 contained 39 Ewing sarcoma samples. Gene expression profiling for all three datasets were conducted using Affymetrix Human Genome U133 Plus 2.0 Array. We downloaded the cell files and re-performed RMA normalization for all samples using Affymetrix's Expression Console.

Using the RMA normalized data, we performed selection normal vs. Ewing's sarcoma gene expression analysis using LIMMA (Smyth, 2004) package. We compared the results from microarray studies and our RNAseq study and found strong similarity in term of differentially expressed genes. The correlation of fold change between the top 1000 differentially expressed genes is 0.63 with p value =2.2e-16. Such strong correlation provides strong evidence of similarity between the microarray and RNAseq data analysis results. Additionally, the R2 platform was used for querying human EFT microarray datasets (Koster, 2008). Survival curves were generated using Prism software (GraphPad).

Microscopy

Bright-field images were collected on an Olympus BX51 upright microscope or on a Leica M165 FC stereoscope. Detection of double-labeling was performed using either confocal imaging on a

Leica TCS SP5 laser-scanning or with an Olympus fluorescent microscope outfitted with an Optigrid system (qioptiqimaging) for optical sectioning and Metamorph™ software (Molecular Devices) for image acquisition.

Results

GLI2ΔN induces the formation of undifferentiated small round cell sarcoma

Originally we sought to initiate ectopic Shh pathway activity in cerebellar Purkinje neurons by pairing the *L7(Pcp2)-cre* transgenic driver (Lewis P.M., 2004) with either *SmoM2* (Mao et al., 2006) or *CLEG2* alleles (Pasca di Magliano et al., 2006). Much to our surprise, we found that *L7(Pcp2)-cre; CLEG2* (*PCG2*) mice developed soft tissue tumors in the proximal limbs, head/ neck, and orbitals (**Figure 4.1I and K**). This phenotype was 100% penetrant (in both male and female mice) and tumors, which appeared on average around 8 weeks of life (n=46 mice), were highly aggressive, with potential to expand several cm within one week of first being palpable (**Figure 4.1I and J**). Basic histology indicated that *PCG2* tumors exhibited the hallmark SRCS pathology, typified by hyper dense regions of small round cells with high nuclear to cytoplasmic ratio, and varying expanses of necrosis similar to human SRCS (**Figure 4.1A-D**). Because aberrant Shh pathway activity following loss of the tumor suppressor, Ptch, has previously been linked to the formation of RMS (Hahn et al., 1998), we utilized *Ptch1*$^{+/-}$ (*Ptch*^{lacZ}) germline mutant mice for comparison, in which entrapped myofibers were abundant much like human RMS (**Figure 4.1E-H**).

Immunophenotype indicated that *PCG2* tumors consistently lacked evidence of myogenic differentiation, while clear reactivity for Myogenin, MyoD and Desmin was detected in *Ptch1*$^{+/-}$

tumors (**Figure 4.2A-F**). Two other factors seen in RMS, Pax7 and PDGFRα (Mao et al., 2006; Rubin et al., 2011; Taniguchi et al., 2008), were also evaluated. No Pax7 was seen in *PCG2* tumors although variable expression of PDGFRα, also a mesenchymal marker, was detected across a panel of several separate tumors (**Figures 4.2G, H** and 4**.3A-J**). Additionally, *PCG2* tumors often displayed a large fraction of proliferating cells, determined by Ki67 staining (**Figure 4.3K-O**), another typical feature of undifferentiated SRCS (Fletcher et al., 2013). The undifferentiated status of *PCG2* tumors was consistent, indicated by the absence of Myogenin and Desmin staining (**Figure 4.3P-Y**). Unfortunately, we were unable to evaluate a tumor phenotype in *L7(Pcp2)-cre; SmoM2* animals because these mice succumbed at weaning from brain malformations and concomitant low birth weight (**Figure 4.4A-B'**).

Further analysis of *PCG2* tumors indicated persistent Shh pathway activity, indicated by *Gli1* mRNA, and Gli1 and Cyclin D1 protein, direct read-outs for Shh signaling (**Figure 4.5A-B, D**) (Bai C.B., 2002; Kenney and Rowitch, 2000). We found that *PCG2* tumors display a high frequency of primary cilia (**Figure 4.5E, F**). Additionally, Gli2 protein was distributed widely in *PCG2* tumors, though localization appeared to be largely cytoplasmic, not compartmentalized at the distal tip of cilia as reported in other contexts (**Figure 4.5E,' F'**) (Qin et al., 2011). Gli2 was not detectable in *Ptch1*$^{+/-}$ RMS tumors (**Figure 4.5C**), suggesting that the level of Shh pathway activity may be another distinction between these two SRCS phenotypes. Altogether, these findings indicate that oncogenic Gli2 function is sufficient to drive the formation of undifferentiated, soft tissue SRCS distinctly different from RMS.

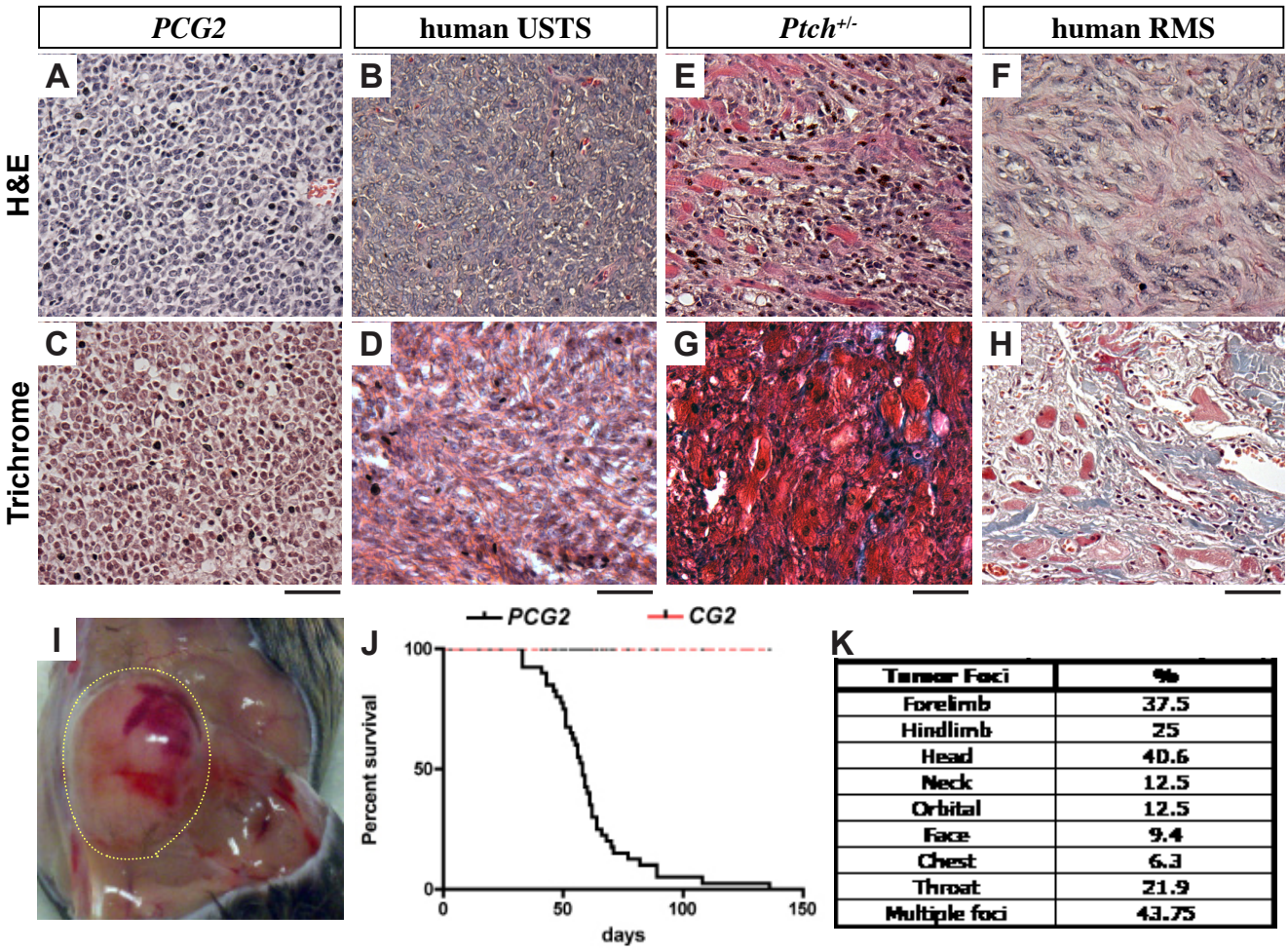

Figure 4.1. GLI2Δ N induces the formation of undifferentiated small round cell sarcoma in mice.

(A-H) Basic histological profile of *PCG2* tumors (A, C) compared to human USTS (B, D), *Ptch*$^{+/-}$ RMS (E, G), and human RMS (F, H). (I) External view of *PCG2* tumor mass located on the right proximal hind limb. (K) Kaplan-Myer survival plot for *PCG2* mice. Scale bars indicate 50 μm.

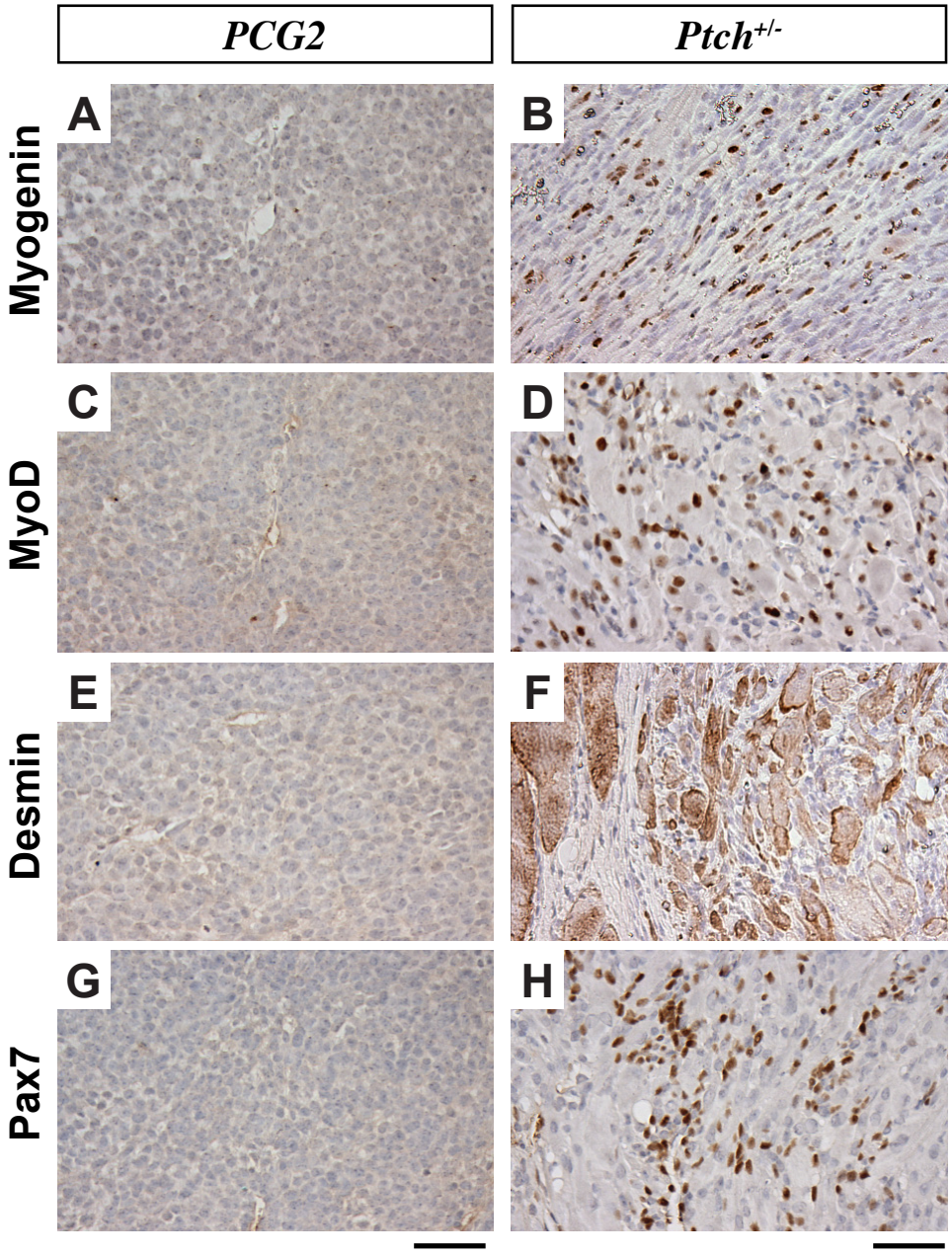

Figure 4.2. Immunophenotype indicates tumors from *PCG2* mice are undifferentiated SRCS.

Immunohistochemical profile of tumors from *PCG2* (A, C, E, G) and *Ptch*$^{+/-}$ mice (B, D, F, H). *PCG2* tumors lack myogenic marker expression, while *Ptch*$^{+/-}$ RMS display robust expression for Myogenin (A versus B), MyoD (C versus D), Desmin (E versus F), and Pax7 (G versus H). Scale bars indicate 50 μm.

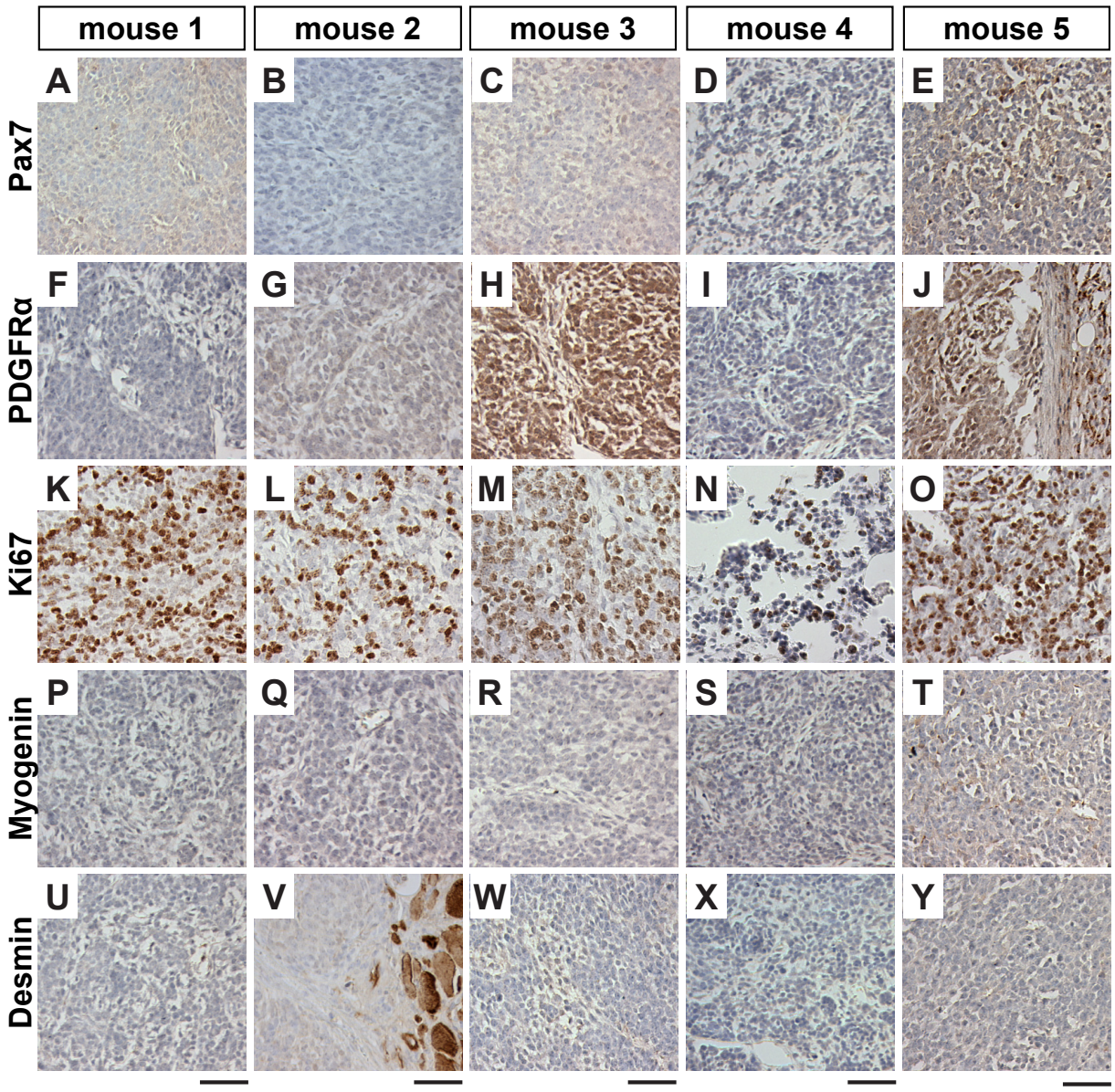

Figure 4.3. Immunophenotype of *PCG2* SRCS does not vary significantly across many samples.

(A-Y) Immunohistochemical profile indicates that phenotype of *PCG2* mice is not variable. *PCG2* tumors consistently lack expression of RMS markers Pax7 (A-E), PDGFRα (F-J), Myogenin (P-T), and Desmin (U-Y), but typically display a large proliferative fraction marked by Ki67 expression (K-O). Scale bars indicate 50 μm.

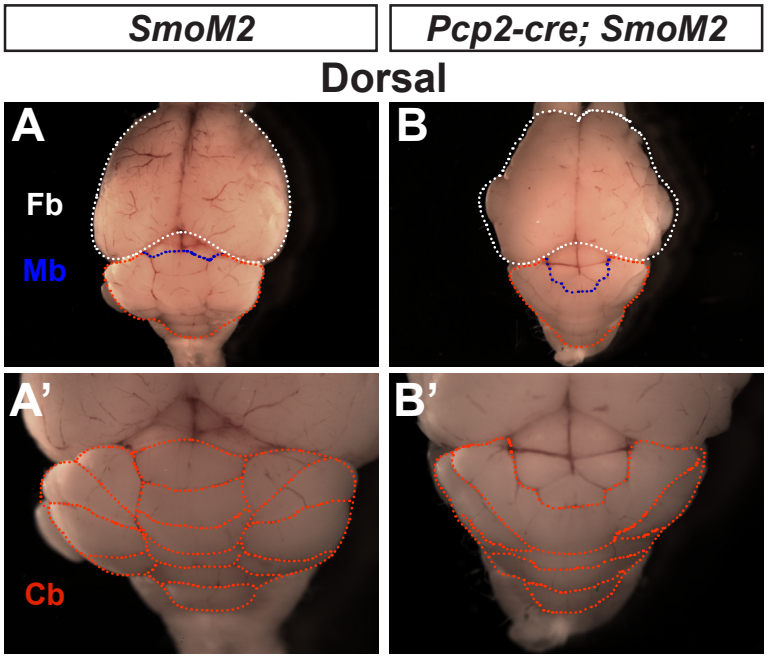

Figure 4.4. ***L7(Pcp2)-cre; SmoM2*** **succumb prior to tumor formation due to brain malformation.**

(A-B') External views of the dorsal surface of *SmoM2* (A, A') and *L7(Pcp2)-cre; SmoM2* (B, B') adult brains. Forebrain (white outline) of *L7(Pcp2)-cre; SmoM2* cerebella (B, B') exhibited large bulges that protruded through the skull, and cerebella (red outline) were malformed, with extreme narrowing along the medial-lateral axis when compared to *SmoM2* brains (A, A'). Cb, cerebellum; Fb, forebrain; Mb, midbrain.

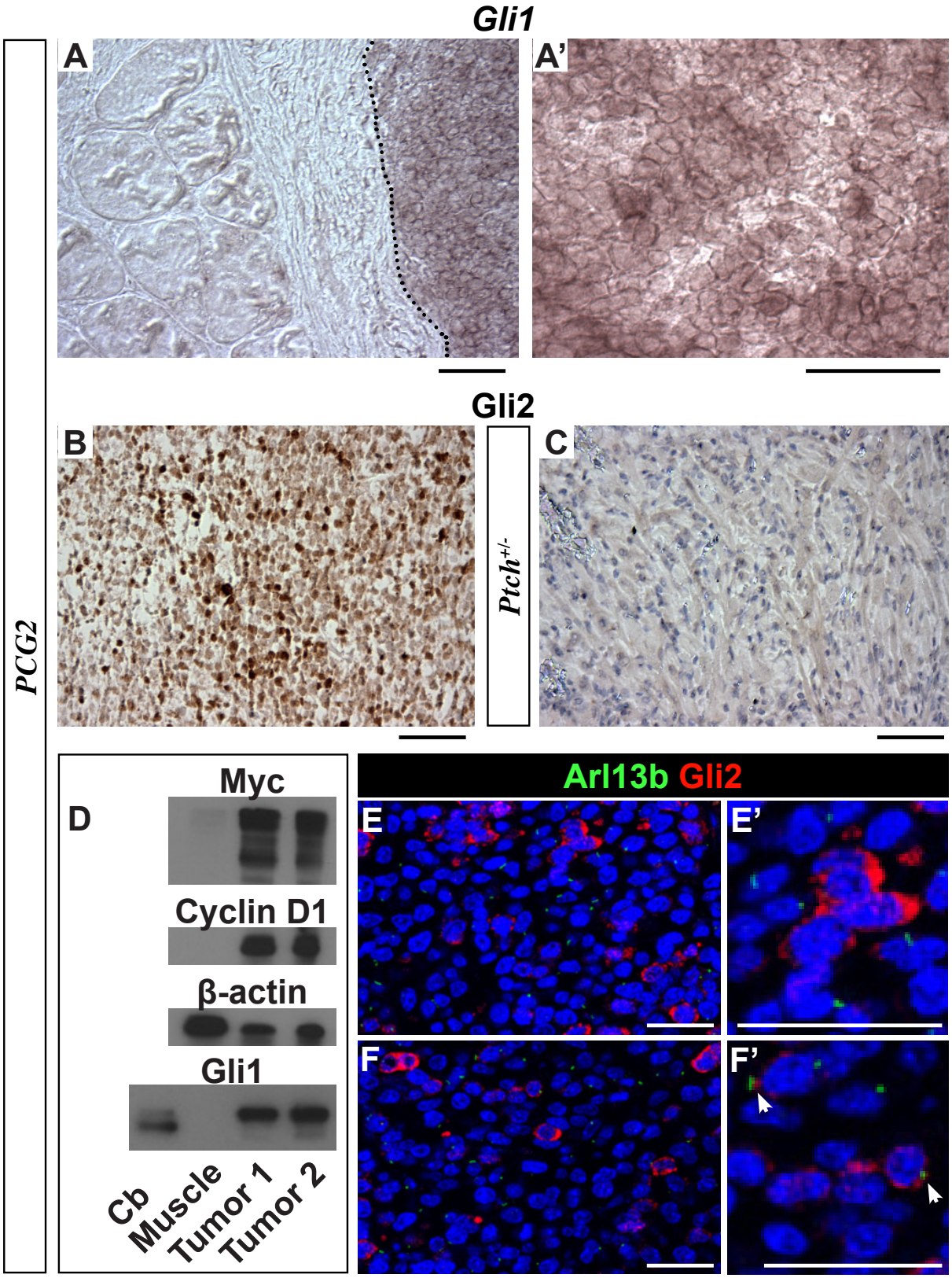
Gli1
A
A'
Gli2
B
C
Ptch+/-
PCG2
D
Myc
Cyclin D1
β-actin
Gli1
Cb
Muscle
Tumor 1
Tumor 2
Arl13b Gli2
E
E'
F
F'

Figure 4.5. Persistent Shh pathway activity was detected in *PCG2* SRCS.

(A-F') Evaluation of Shh pathway activity in *PCG2* tumors, measured by *Gli1* mRNA (A, A') and Gli2 staining (B), which was not detectable in $Ptch^{+/-}$ RMS (C). *Gli1* expression was robust in regions of tumor (black outline), but was not detectable in adjacent skeletal muscle fibers depicted on the left (A). (D) Western blotting further confirmed activation of pathway activity, indicating robust levels of Shh targets Gli1 and Cyclin D1, while Myc and β-actin served as controls. (E-F') Staining for Arl13b (green), indicated that *PCG2* tumors are widely ciliated and that Gli2 protein (red), is only detected in cytoplasmic pools, not in cilia distal tips. Scale bars indicate 50 μm (A-C) and 25 μm (E-F').

Gene profiling of *PCG2* tumors highlights the Ewing's family of tumors

In order to isolate a more specific SRCS subtype designation for *PCG2* tumors, we evaluated their gene expression profile using Next-Gen RNAseq. Unbiased and hierarchal clustering revealed a distinct signature for tumor versus unaffected control tissue (tibialis anterior muscle) (**Figure 4.6A**). Among the top 100 differentially expressed genes we found cell cycle genes, numerous mesenchymal progenitor genes, and several Shh target genes, the most intriguing of which was Nkx2.2 (**Figure 4.6B**). Mounting evidence has indicated expression of this pro-neural transcription factor is tightly correlated with the Ewing's family of tumors (EFT), but not other SRCS subtypes (Smith et al., 2006; Yoshida et al., 2012).

Indeed, the immunophenotype of *PCG2* tumors included robust expression of Nkx2.2, while $Ptch^{+/-}$ RMS was clearly negative (**Figure 4.6C, D**). We obtained numerous human EFT specimens from archives at VUMC (n=13), which further corroborated this trend (**Figure 4.6E, F**). We then compared the top 1000 differentially expressed genes from our *PCG2* profile with an additional human EFT microarray dataset (n=37), and found a Pearson's correlation value of 0.65, indicating strong similarity between these two genes profiles (a value of 1 indicates an

exact match). We queried an additional gene expression dataset using the R2 platform (Koster, 2008), representing a broad spectrum of human EFT specimens (n=154 combined), and independently found a consistent association of NKX2.2 expression and EFT (**Figure 4.7A**).

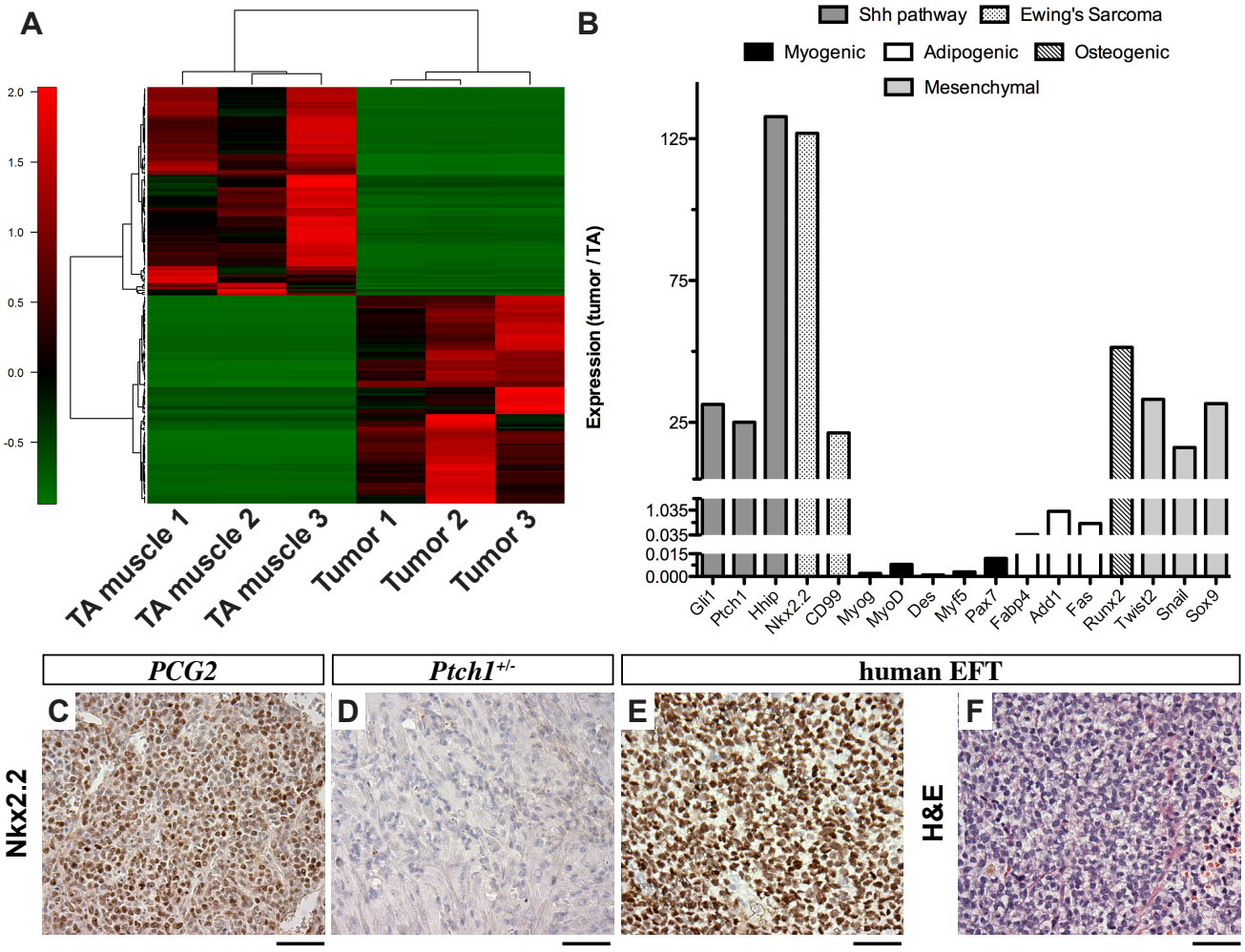

Figure 4.6. Gene profiling of *PCG2* tumors highlights the Ewing's family of tumors.

(A) Clustering analysis showing 100 most differentially expressed genes from *PCG2* tumor versus unaffected, adjacent tibialis anterior muscle (n=3) from RNA-seq expression profiling. (B) Expression of relevant pathway components ranked by clustering and gene ontology comparison. *PCG2* tumors showed high expression of Shh pathway target genes, mesenchymal genes, and EFT markers, Nkx2.2 and CD99, but did not strongly express adipogenic or myogenic markers. (C-F) Immunophenotyping indicated that *PCG2* tumors robustly expressed EFT marker, Nkx2.2 (C), which was not detectable in *Ptch*$^{+/-}$ RMS (D). Strong NKX2.2 expression was similarly seen in human EFT samples (E) that showed similar SRCS morphology to *PCG2* tumors at the basic histopathology level (F).

This difference between *PCG2* and human EFT gene profiles may be explained, at least in part, by differences between target gene activation by the EWS-FLI1 oncoprotein versus GLI2 alone, which itself may be an EWS-FLI1 transcriptional target. In pursuit of this latter notion, we again queried the above human EFT specimens (n=154 combined) using the R2 platform (Koster, 2008), and found high *GLI2* and *PTCH1* expression was frequently associated with this sarcoma family (**Figure 4.7B, C**). We speculated that if EWS-FLI1 mediates transformation by utilizing GLI2, an EWS-FLI1 – GLI2 interaction should be detectable. ChIP-Seq using an HA-tagged EWS-FLI1 was previously reported (Patel et al., 2012), and we queried these data and mapped two EWS-FLI binding peaks to GLI2 on chromosome 2. One peak corresponded to a 1.7 kb region with 13 potential FLI1 binding motifs, and a second mapped to a 1.7 kb region with 8 motifs (**Figure 4.7D** and not shown). These data strongly suggest that EWS-FLI1 binds GLI2, but additional work is required to fully demonstrate not only that this interaction occurs, but also that it regulates transcription of GLI2 and confers tumor propagating potential to human EFT cells. For a detailed list of experiments, refer to CHAPTER V, pages 119-129.

***PCG2* tumors originate in multipotent mesenchymal progenitors**

Determinations regarding the cellular origin for most sarcoma variants largely remain open-ended, owing to their undifferentiated phenotype. A clear line of differentiation, as seen in RMS, is not available to provide insight into their lineage. For EFT cellular origin, two schools of thought currently posit that EFT arise either from mesenchymal stem cells, or from the neural crest (Jedlicka, 2010). To investigate the cellular origin of *PCG2* tumors, *L7(Pcp2)-cre* mice were employed for fate-mapping studies. In addition to reported expression in Purkinje neurons (Lewis P.M., 2004), cre recombinase activity was detected in forelimb level dermamyotome cells

expressing either Pax3, Pax7, Myf5 or Myogenin in *L7(Pcp2)-cre; Rosa*^{eYFP} embryos between e9.5-e11.5 (**Figure 4.8A-D**). This molecular signature is indicative of mesenchymal progenitor cells, collectively known to generate skeletal muscle, dermis, adipocytes, bone, and satellite cells (Sabourin and Rudnicki, 2000). Consistent with this labeling, at e16.5-e17.5 reporter^{+} cells were found in dorsal and ventral myofibers of the trunk, but not limbs, in the proximal-most humorous bone primordium, and within the interstitium (**Figure 4.9A-C'**).

In distal hind limb muscles (tibialis anterior and gastrocnemius) from *L7(Pcp2)-cre;* Ai9 mice at P3, I found only that interstitial, myofiber-associated (MFA) cells expressing Vimentin were reporter^{+}, but myofibers themselves were not (**Figure 4.9D, D'**). Imaging of intact musculature in *L7(Pcp2)-cre;* Ai9 mice at P30 clearly indicated that myofibers of the head/ neck and proximal limbs were indeed reporter^{+} (**Figure 4.10A-B'**). The identity of these cells was clearer in cross sectional images of proximal hind limb in which myofibers were tdTomato^{+}, as were PPARγ^{+} adipocytes, consistent with embryonic fate-mapping (**Figure 4.10C, C'**). Allocation of the *L7(Pcp2)-cre* lineage did not appear to be altered by aberrant Shh signaling, since labeling in cross sections of *PCG2; Ai9* limbs was comparable to that seen in *PCG2* mice (not shown). Altogether, these data confirm that the *L7(Pcp2)-cre* lineage encompasses multipotent mesenchymal progenitors.

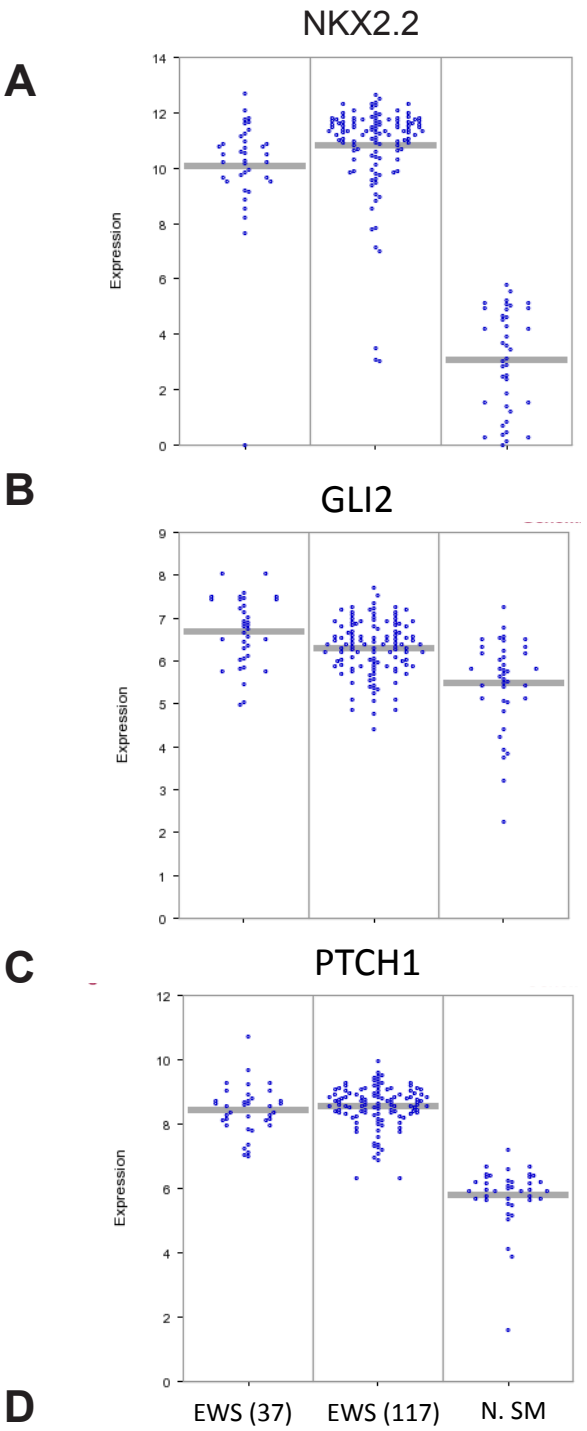

GLI2

chr2:121540126-121542000 **1.8 kb**

chr2:121566251-121568000 **1.7 kb**

Figure 4.7. Expression of *GLI2* in human EFT is likely driven by EWS-FLI1 activation.

(A-C) Expression of NKX2.2 and Shh pathway genes GLI2 and PTCH1 in a cohort of human EFT samples (n=37 and n=117) versus normal skeletal muscle. LOG2 expression displayed using the R2 microarray analysis and presentation platform. (D) Mapping of enrichment peaks for HA-EWS-FLI1 at three distinct locations on the GLI2 sequence using UCSC software.

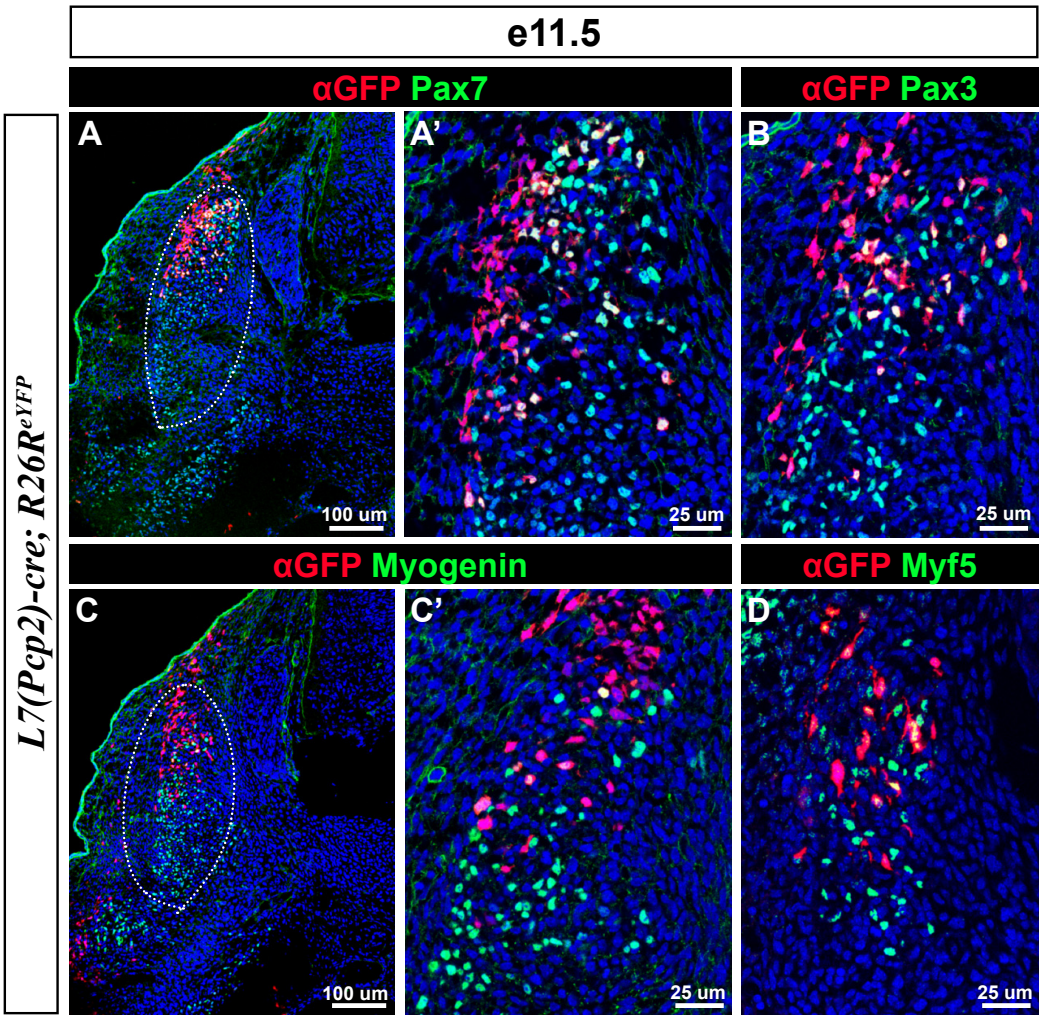

Figure 4.8. The *Pcp2* lineage includes mesenchymal progenitors in the dermamyotome.

(A-D) Transverse sections of *L7(Pcp2)-cre; R26R*^{eYFP} embryos (e11.5) at the forelimb level depicting the transient dermamyotome (white outline, A and C). Pcp2 lineage cells (red) express mesenchymal progenitor markers Pax7 (A, A'), Pax3 (B), Myogenin (C, C'), and Myf5 (D). Scale bars represent the indicated distances.

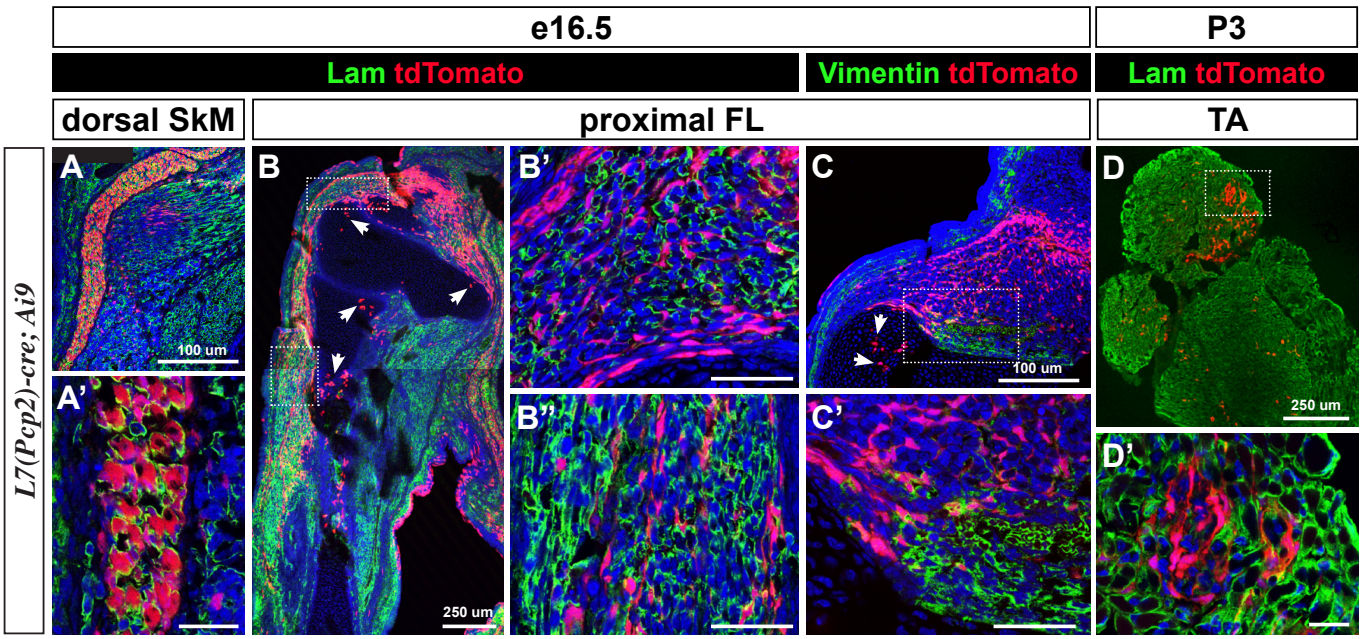

Figure 4.9. Late embryonic trunk muscle, bone and interstitial cells emerge from *Pcp2* lineage cells.

(A-C') Transverse sections of *L7(Pcp2)-cre; Ai9* embryos (e16.5-e17.5) at the forelimb level depicting Pcp2 lineage cells (red) within the dorsal skeletal musculature, expressing laminin (A, A'), as well as within the proximal humorous bone (B) and the interstitium (B-B"). A subset of interstitial cell expressed mesenchymal marker Vimentin (C, C'). (D, D') Cross sections of *L7(Pcp2)-cre; Ai9* tibialis anterior muscle indicated that Pcp2 lineage cells (red) were exclusively part of the interstitial space between laminin^{+} myofibers at P3. Lam, Laminin. Scale bars indicate 25 μm unless otherwise indicated.

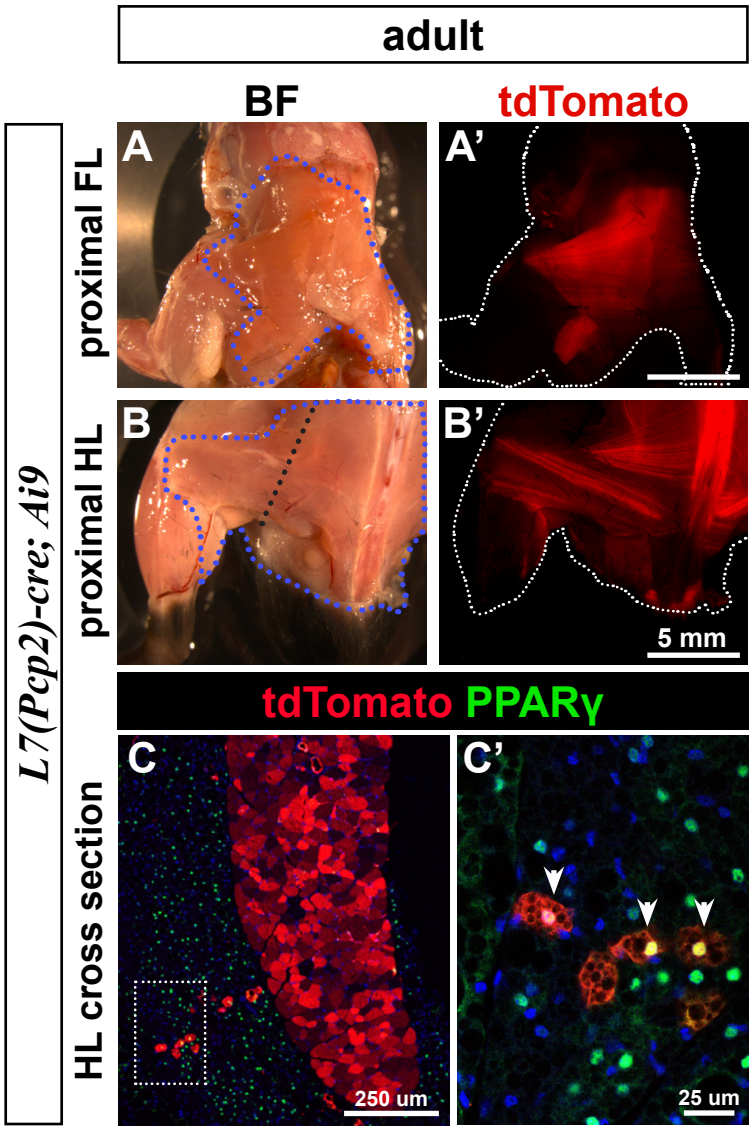

Figure 4.10. The *Pcp2* lineage contributes extensively to skeletal musculature and fat.

(A-B') whole mount fate-mapping of adult *L7(Pcp2)-cre; Ai9* mice. Direct fluorescence for tdTomato indicated that Pcp2 lineage cells (red) contribute widely to skeletal musculature (blue outline). (C, C') Cross sections of proximal hind limb revealed that Pcp2 lineage cells generate both mature myofibers (C) and PPARγ^{+} adipocytes (C'). White arrowheads indicate double labeled cells. Scale bars indicate 25 μm unless otherwise indicated.

Lineage-specific activation of GLI2ΔN phenocopies EFT-like SRCS

Having prospectively traced back the origin of *PCG2* tumors, we wanted to narrow down whether tumor-propagating potential resides within lineage-committed precursors versus multipotent mesenchymal progenitors. To this end GLI2ΔN was selectively activated in three distinct lineages: (1) early myoblasts, satellite cells and precursors of embryonic brown fat using *Myf5*^{Cre} mice (Beauchamp et al., 2000; Cornelison and Wold, 1997; Kuang et al., 2007; Seale et al., 2008), (2) adipocyte precursors using *aP2-cre* mice (Hatley et al., 2012; Urs et al., 2006), and postnatal and adult satellite cells using *Pax7-creER* mice (Murphy et al., 2011).

Targeting GLI2ΔN to *Myf5*^{Cre} cells drove tumor formation in ~50% of the resulting *M5G2* mice (n=11). These animals exhibited highly aggressive EFT-like SRCS typically by four weeks of age (**Figure 4.11A, I**), usually near the head and proximal fore limbs. The remainder of *M5G2* mice were severely runted and succumbed prior to tumor formation. Interestingly, *M5G2* tumors were histopathologically indistinguishable from *PCG2*; no detectable expression of Myogenin, MyoD, Desmin or Pax7 could be found, although robust Nkx2.2 expression was consistently observed in all *M5G2* tumors that I evaluated (**Figure 4.11B-D**).

Though *Myf5*^{Cre} cells are primarily myogenic precursors, the inclusion of fat and satellite cells in this lineage, albeit minor, prompted us to further evaluate tumor origin. Activation of GLI2ΔN in fatty acid binding protein-4 (fabp4)/ adipocyte protein-2 (aP2)$^{+}$ precursors of both brown and white fat using *aP2-cre* mice resulted in a SRCS phenotypic outcome similar to *PCG2* and *M5G2* mice (**Figure 4.7E**). 100% of *aP2G2* animals formed tumors in similar regions, including the head, neck, orbitals, and proximal limbs within 8 weeks on average (**Figure 4.11J**).

Occasionally tumors also occurred in the genitourinary region, likely owing to an accumulation of adipocytes in this anatomical site (see below). Immunophenotyping indicated that *aP2G2* tumors were histopathologically indistinguishable from *PCG2* and *M5G2* mice (**Figure 4.11F-H**).

Though these findings seemed to help narrow down the EFT cellular origin to adipocyte precursors, further evaluation of the *aP2-cre* lineage using *aP2-cre; Ai9* mice surprisingly revealed some contribution of these cells to myofibers (**Figure 4.12C', E, E'**). This finding contrasts what is known regarding the contribution of fabp-4/ $aP2^+$ cells (Hatley et al., 2012), but is the only global assessment of this lineage to the intact organism. Together, these findings indicate that GLI2ΔN tumor-initiating potential is not likely restricted to either myogenic or adipogenic precursors, or their precursors.

One additional cellular lineage that I chose to evaluate was myogenic satellite cells, which persist in the adult skeletal musculature (Kuang et al., 2007). GLI2ΔN was activated in $Pax7^+$ satellite cells using *Pax7-creER* mice, which received tamoxifen (TM) on P3 or P60. Regardless of when GLI2ΔN activation was induced, all *P7G2* mice to date formed SRCS, between 3-10 weeks of life (**Figure 4.13K**, n=6). Largely, tumors affected proximal limb and face regions, however, in some instances *P7G2* mice also developed tumor foci along the trunk, which appeared to emerge from muscle associated with the lumbar vertebrae (**Figure 4.13B**). Though metastases are known to occur in EFT (Shukla et al., 2013), it is difficult to conclude whether these foci were primary tumors or metastatic tumors.

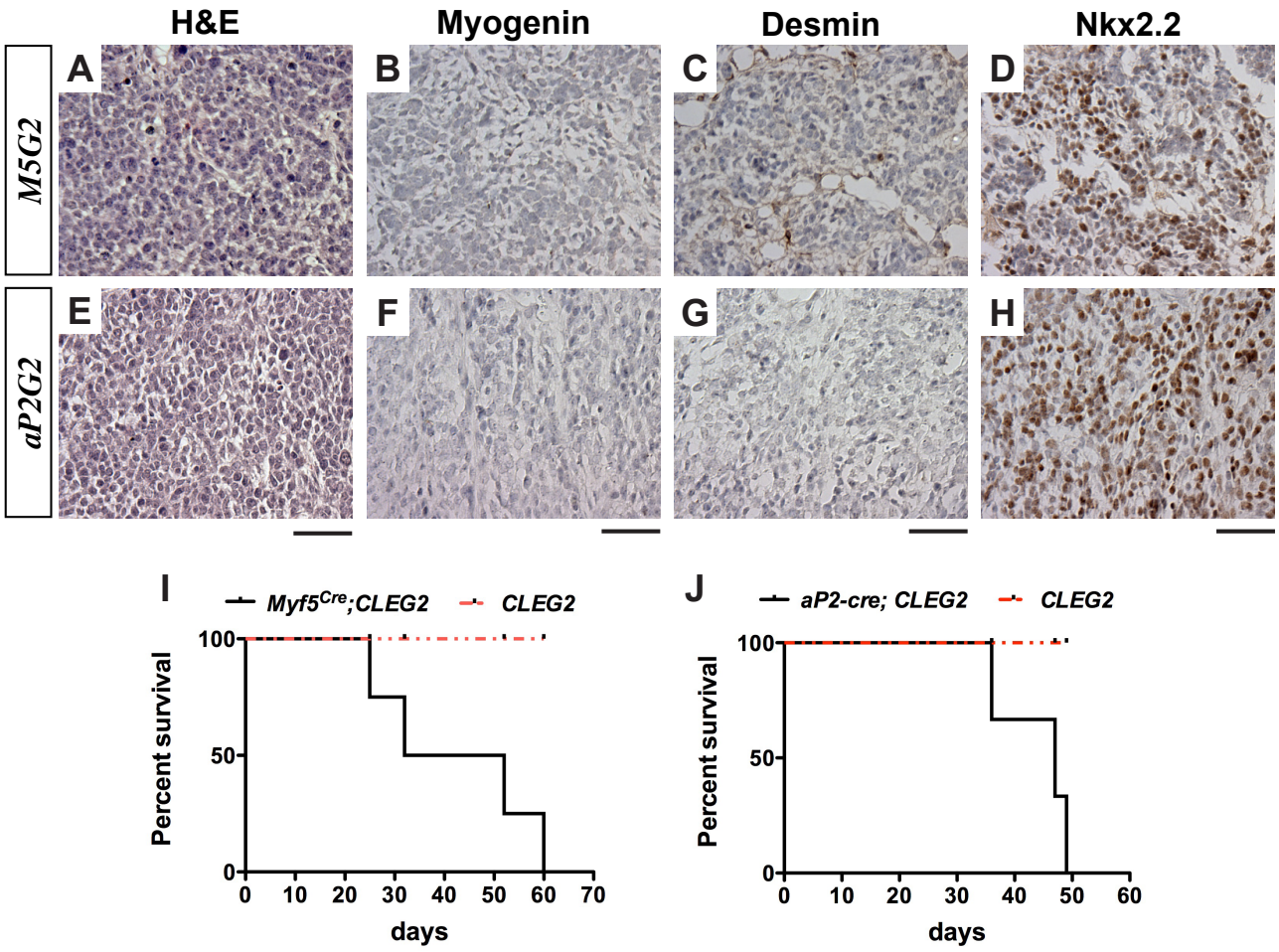

Figure 4.11. Lineage-specific activation of GLI2Δ N phenocopies EFT-like SRCS.

(A-H) Basic histopathology and immunophenotyping of *M5G2* (A-D) and *aP2G2* (E-H) mice indicated that activation of GLI2ΔN in either lineage recapitulates the EFT-like SRCS phenotype of *PCG2* mice. No expression of myogenic markers Myogenin (B, F) or Desmin (C, G) was detectable, although robust expression of Nkx2.2 was observed (D, H). (I, J) Kaplan-Myer survival curves for *M5G2* (I) and *aP2G2* (J) mice. Scale bars indicate 50 μm.

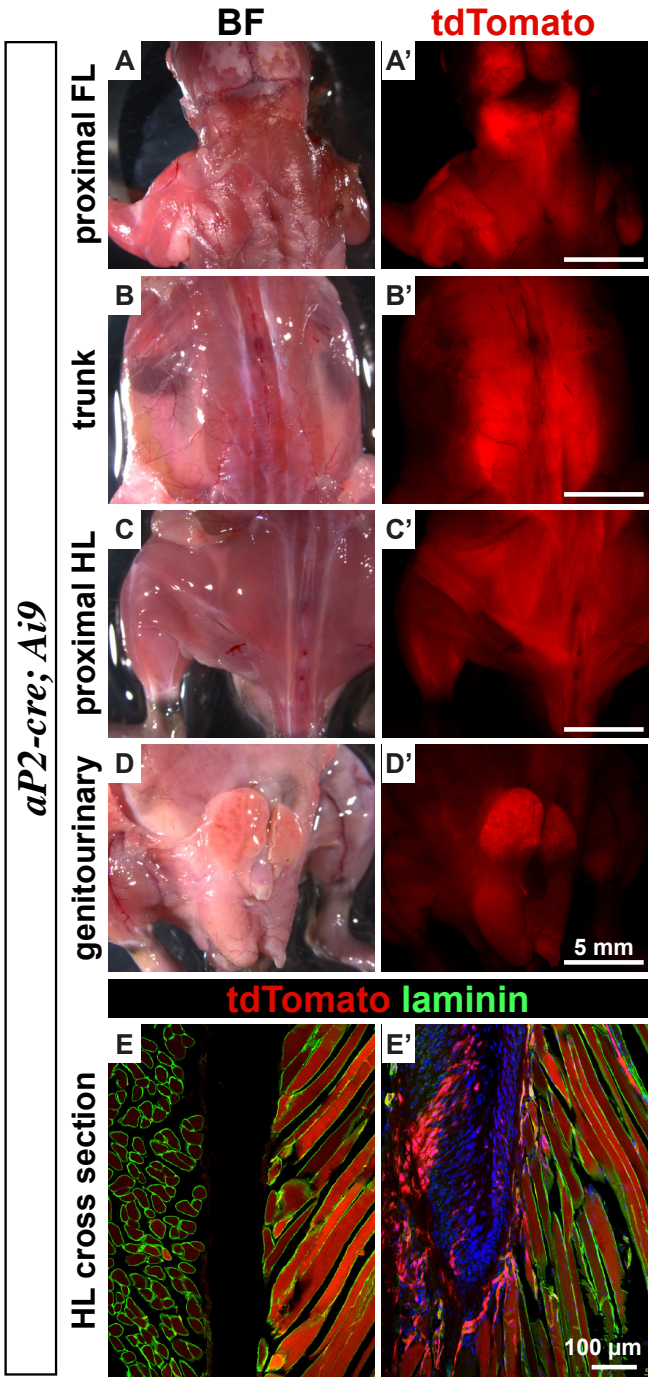

Figure 4.12. The aP2 lineage makes an unexpected contribution to skeletal muscle.

(A-D') whole mount fate-mapping of adult *aP2-cre; Ai9* mice. Direct fluorescence for tdTomato indicated that aP2 lineage cells (red) contribute widely to fat stores throughout the animal. (C, C') Cross sections of proximal hind limb revealed that aP2 lineage cells also contribute to mature, Laminin^{+} myofibers (E, E'). Scale bars represent the indicated distance.

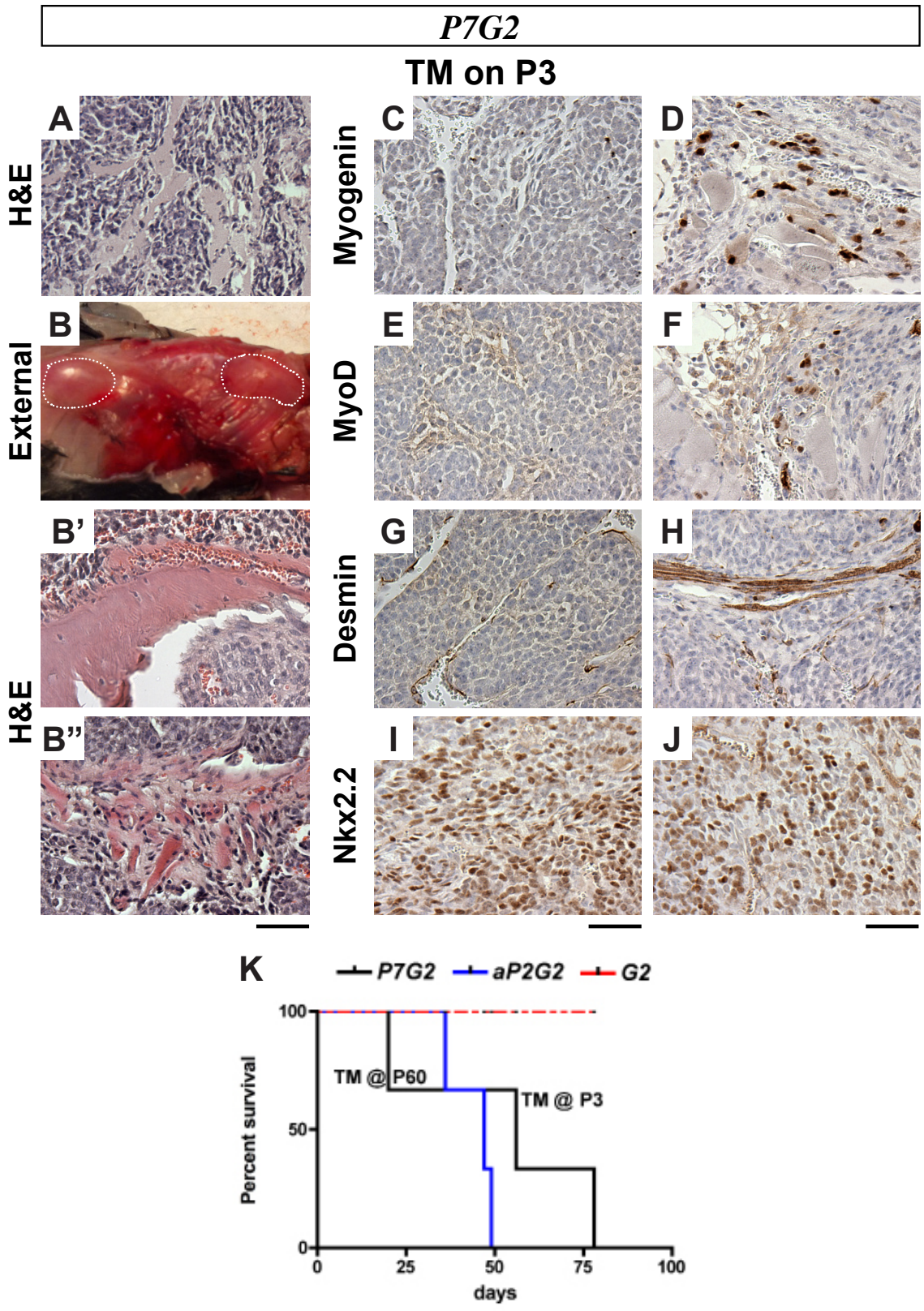
P7G2
TM on P3
A
H&E
B
External
B'
H&E
B"
C
Myogenin
D
E
MyoD
F
G
Desmin
H
I
Nkx2.2
J
K
P7G2
aP2G2
G2
100
50
0
Percent survival
TM @ P60
TM @ P3
0
25
50
75
100
days

Figure 4.13. Postnatal Pax7$^+$ cells can be transformed by GLI2Δ N to form EFT-like SRCS.

(A-J) Basic histopathology and immunophenotyping of *P7G2* mice indicated that activation of GLI2ΔN in postnatal Pax7$^+$ cells recapitulates the EFT-like SRCS phenotype of *PCG2*, *M5G2*, and *aP2G2* mice (A). (A-B") Histopathology revealed several attributes unique to *P7G2* mice; cystic spaces filled with eosinphilic matrix (A), rare spinal tumor foci (B), which displayed large areas of osteoid-like matrix (B') and entrapped muscle fibers (B"). Expression of myogenic markers Myogenin (C, D), MyoD (E, F) and Desmin (G, H) was detectable only in limited regions, most likely a result of tumor-induced myopathy in adjacent skeletal muscle. Robust expression of Nkx2.2 was consistently observed (I, J). (K) Kaplan-Myer survival curve for *P7G2* mice. Scale bars indicate 50 μm.

Additionally, *P7G2* tumors frequently exhibited histopathological features not seen in *PCG2*, *M5G2*, or *aP2G2* tumors. The most obvious were vast cystic spaces filled with eosinphilic deposits, some of which resembled osteoid, a defining feature of osteosarcoma (**Figure 4.13A, B'**). The second feature was a combination of extensive infiltrating Desmin$^+$ myofibers (**Figure 4.13B", H**) and regions of Myogenin$^+$ or MyoD$^+$ cells, which may be evidence of tumor-induced myopathy (**Figure 4.13D, F**). Though these histopathological features were intriguing, they were not sufficient to change the undifferentiated SRCS designation, since P7G2 tumors were otherwise immuno-histopathologically similar to *PCG2*, *M5G2*, and *aP2G2* tumors (**Figure 4.13C, E, G, I**). Collectively, these analyses highlight two sources of EFT initiating cells, either multipotent Pax7$^+$ cells disseminating from the embryonic dermamyotome or those embedded in the postnatal skeletal muscle interstitium.

Attenuating Shh pathway function modifies SRCS phenotype

The initial finding that GLI2ΔN is sufficient to induce EFT-like SRCS is intriguing, considering that activation of Shh signaling at the level of Patch/ Smo leads to RMS. Such divergent phenotypic outcomes may indicate that the intensity of pathway activation is a key influential

force in the sarcoma spectrum. To test this notion, one copy of *Gli1*, the other transcriptional activator of Shh target genes, was removed in an attempt to attenuate pathway activity. Only 30% of the resulting *PCG2; Gli1*^{nlacZ} mice developed tumors with an average onset of 6 months, while the remaining 70% succumbed to old age between 1.5-2 years (**Figure 4.14M**). Histopathological analyses revealed distinctive morphological features not seen in any *PCG2* tumors, including dense cell clusters surrounded by rich collagen deposits or very large, fluid-filled cystic spaces (**Figure 4.14B, D**, and not shown). Importantly, in addition to these distinguishing features, the immunophenotype of *PCG2; Gli1*^{nlacZ} tumors did differ significantly from *PCG2* tumors; expression of Nkx2.2 was not detected, though neither were myogenic RMS markers (**Figure 4.14F, I, J**). *PCG2; Gli1*^{nlacZ} tumors, similar to *PCG2*, were highly proliferative and exhibited persistent Shh pathway activation (**Figure 4.14G, H, K, L**). However, the meaningful differences described above indicate that attenuation of pathway activity can substantially modify the phenotypic outcome of SRCS, reverting an EFT-like phenotype to undifferentiated SRCS.

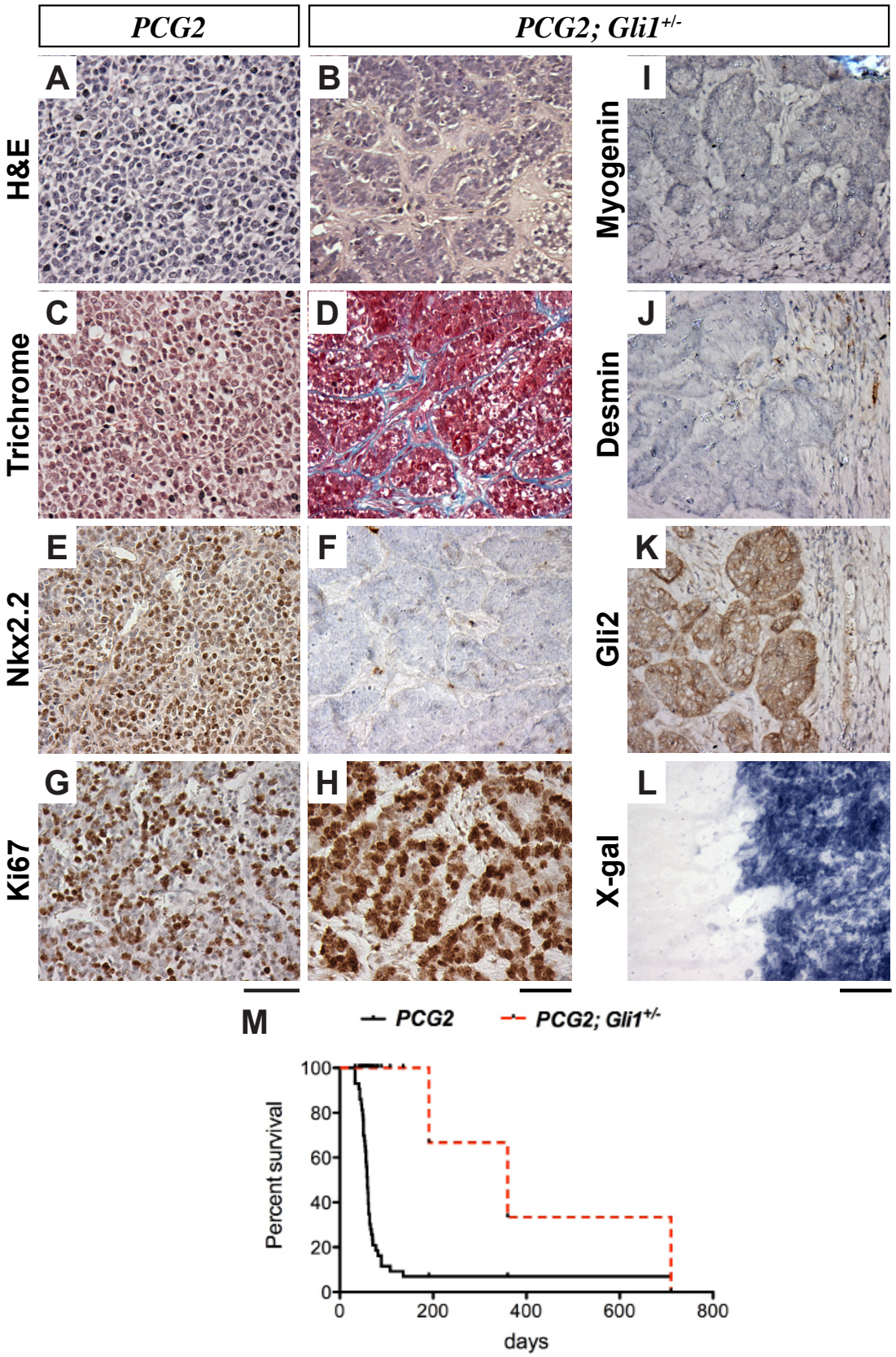
PCG2
PCG2; Gli1+/-
A
B
I
H&E
Myogenin
C
D
J
Trichrome
Desmin
E
F
K
Nkx2.2
Gli2
G
H
L
Ki67
X-gal
M
PCG2
PCG2; Gli1+/-
Percent survival
100
80
60
40
20
0
0
200
400
600
800
days

Figure 4.14. Attenuation of Shh signaling activity modifies the SRCS phenotype.

(A-M) Comparison of tumors from *PCG2* (A, C, E, G) and *PCG2; Gli1*$^{+/-}$ (B, D, F, H) mice indicated that attenuation of Shh pathway activation modifies SRCS phenotype. (A-D) Basic histopathology indicated that *PCG2; Gli1*$^{+/-}$ tumors exhibited dense cellular clustering and rich collagen deposits (blue) not seen in *PCG2* tumors. Most notably, no expression of Nkx2.2 was detected in *PCG2; Gli1*$^{+/-}$ tumors (F versus E). However, both tumors exhibited dense proliferative fractions, indicated by Ki67 staining (G, H). The differentiation status of *PCG2; Gli1*$^{+/-}$ tumors was not changed; no expression of either Myogenin (I) or Desmin (J) was detected. Persistent Shh pathway activity was evident, indicated by staining for Gli2 (K) and X-gal (L). (M) Kaplan-Myer survival curves for *PCG2* and *PCG2; Gli1*$^{+/-}$ (J) mice. Scale bars indicate 50 μm.

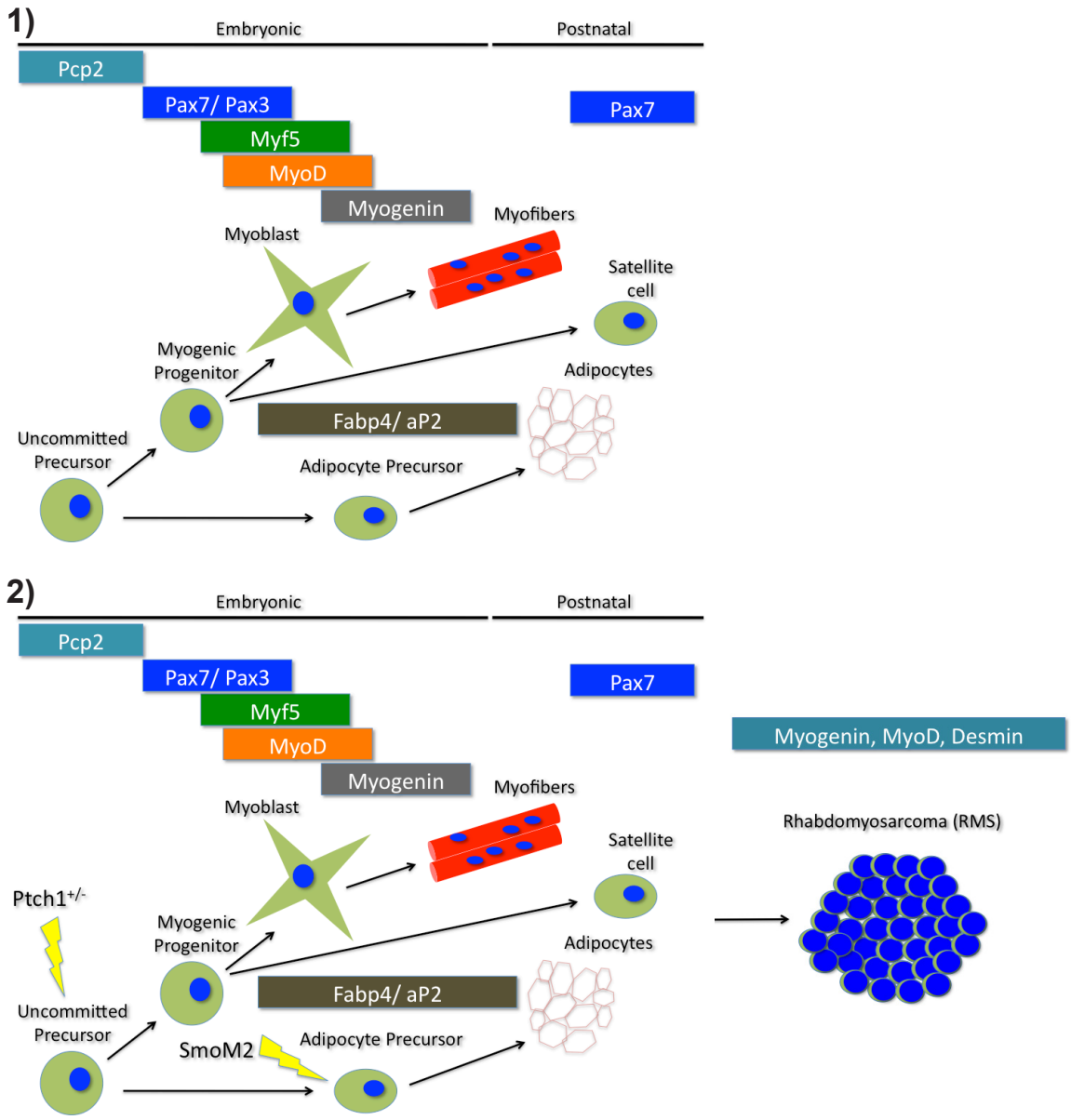
1)
Embryonic
Postnatal
Pcp2
Pax7/ Pax3
Pax7
Myf5
MyoD
Myogenin
Myofibers
Myoblast
Satellite cell
Myogenic Progenitor
Adipocytes
Fabp4/ aP2
Uncommitted Precursor
Adipocyte Precursor
2)
Embryonic
Postnatal
Pcp2
Pax7/ Pax3
Pax7
Myf5
MyoD
Myogenin
Myogenin, MyoD, Desmin
Myofibers
Myoblast
Rhabdomyosarcoma (RMS)
Satellite cell
Ptch1+/-
Myogenic Progenitor
Adipocytes
Fabp4/ aP2
Uncommitted Precursor
SmoM2
Adipocyte Precursor

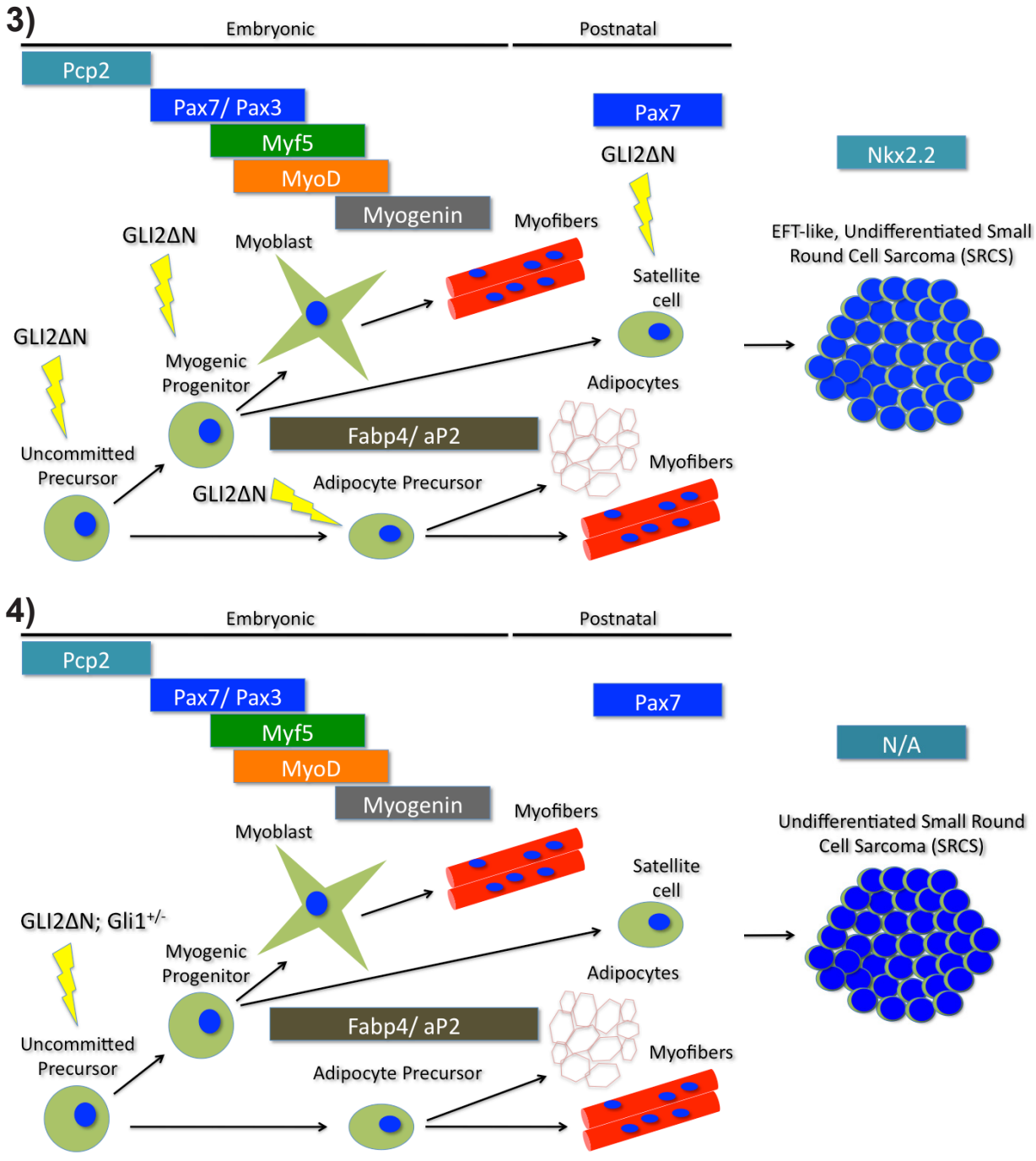
3)
Embryonic
Postnatal
Pcp2
Pax7/ Pax3
Myf5
MyoD
Myogenin
Pax7
GLI2ΔN
Nkx2.2
Myofibers
GLI2ΔN
Myoblast
Satellite cell
EFT-like, Undifferentiated Small Round Cell Sarcoma (SRCS)
GLI2ΔN
Myogenic Progenitor
Adipocytes
Fabp4/ aP2
Uncommitted Precursor
Myofibers
GLI2ΔN
Adipocyte Precursor
4)
Embryonic
Postnatal
Pcp2
Pax7/ Pax3
Pax7
Myf5
MyoD
N/A
Myogenin
Myofibers
Myoblast
Undifferentiated Small Round Cell Sarcoma (SRCS)
Satellite cell
GLI2ΔN; Gli1+/-
Myogenic Progenitor
Adipocytes
Fabp4/ aP2
Uncommitted Precursor
Myofibers
Adipocyte Precursor

Figure 4.15. The level of Shh pathway activation determines SRCS phenotypic outcome.

(1) A schematic diagram summarizing the fate of several mesenchymal precursor populations based on fate-mapping studies described in this thesis work and by others. Briefly, *Pcp2-cre* cells at mid-embryogenesis generate myogenic (Pax7/3^{+}, Myf5^{+}, Myogenin^{+}) and adipogenic (Fabp4/aP2^{+}) precursors, as well as postnatal satellite cells (Pax7^{+}). (2) A summary depicting the prospective Rhabdomyosarcoma cellular origin with respect to Shh pathway activation using either deletion of *Ptch1* in uncommitted precursor cells or *SmoM2* in the adipogenic lineage. (3) A summary of the work described here; deregulated Shh signaling using activation GLI2ΔN in *Pcp2-cre*, Myf5^{Cre}, a*P2-cre*, and *Pax7-creER* lineage cells results in EFT-like SRCS. Surprisingly, fate-mapping studies with a*P2-cre* mice indicated this lineage also contributes to a subset of skeletal myofibers. (4) Attenuation of Shh pathway activation by deletion of one *Gli1* allele from *PCG2* mice modified the tumor outcome from an EFT-like phenotype to undifferentiated SRCS, for which no molecular diagnostic markers are currently available.

Discussion

Collectively, the studies described here extend the connection between deregulated Shh pathway activity and cancer, providing a previously unappreciated link to the formation of EFT-like SRCS. Our data clearly show that elevated GLI2 function is sufficient to potently mediate EFT sarcomagenesis, independently of the characteristic EWS-FLI1 oncoprotein. However, our work also suggests that GLI2 is a key mediator acting directly downstream of EWS-FLI1, which would not be dispensable in the human tumor context. *PCG2* mice are the first genetically-inducible model for EFT, providing a more complete understanding of specific molecular events that drive EFT formation and new insight regarding the cellular origin of Ewing's sarcoma, linking it to multipotent mesenchymal progenitors and satellite stem cells.

An EWS-FLI1 – GLI2 interaction likely underlies EFT formation

Previous studies have implicated the GLI family of proteins as oncogenes; in particular GLI2 is known to be upregulated in numerous human cancers, including glioma (Ruiz i Altaba et al.,

2002). The full-length human GLI2 sequence was found to encode an 328 amino acid N-terminal domain that imposes strong repressor function, and the truncated GLI2ΔN mutant isoform can act as a potent oncoprotein when expressed in mice (Pasca di Magliano et al., 2006; Roessler et al., 2005). It is unlikely that truncating mutations in GLI2 will be linked to the etiology of EFT, since no studies to date have implicated such mutations in any human cancer, rather GLI2 over-expression mediated by unknown means has been found. Rather, our data suggest that activation of GLI2 expression occurs through direct binding of EWS-FLI1 at two distinct locations in the GLI2 sequence.

The EWS-FLI1 translocation is found in the vast majority of EFT cases and appears to be the major driver of sarcomagenesis. It is difficult, therefore, to understand why past attempts to produce a genetically-inducible EFT mouse using EWS-FLI1 have not succeeded. Targeting of a R26R-driven EWS-FLI1 to hematopoietic tissues caused rapid onset of myeloid/ erythroid leukemia (Torchia et al., 2007), while activation of a CAG-driven EWS-FLI1 in mesenchymal cells led to abnormal limb development and accelerated formation of osteosarcoma in a $p53^{-/-}$ background (Lin et al., 2008). Activation of Shh signaling could be required to prime cells for transformation or to better tolerate EWS-FLI1. To test this, introduction of full-length human GLI2 together with EWS-FLI1 into the mesenchymal lineage, or alternatively, introduction of EWS-FLI1 into the $Ptch^{+/-}$ background could be used in an attempt to induce EFT formation. Modeling EFT with an autonomously activated GLI2 allowed us to bypass inherent difficulties associated with EWS-FLI1, but the potential requirement for EWS-FLI1 – mediated GLI2 activation underscores the importance of *PCG2* mice as an accurate recapitulation of EFT.

Cell of origin and mutational profile shape sarcoma phenotypic outcome

Even though mouse modeling difficulties have thus far prevented researchers from gaining new understanding of EFT, extensive efforts have been made to model other sarcoma variants and ascertain their respective cellular origins, including multiple RMS entities, clear cell sarcoma and synovial sarcoma (Haldar et al., 2007; Haldar et al., 2009; Keller et al., 2004; Straessler et al., 2013). Many studies have utilized activation of the Shh pathway to induce embryonal RMS (eRMS), which indicate the cellular origin could either be uncommitted, embryonic precursors or adipocyte-committed precursors (Hahn et al., 1998; Hatley et al., 2012; Mao et al., 2006; Nitzki et al., 2011). Yet, others have incorporated compound mutational profiles (including *Ptch* deletion) into a wide range of cellular lineages, ultimately describing a tumor continuum that connects RMS to undifferentiated pleomorphic sarcoma (Rubin et al., 2011). Our work, however, may have illuminated a much broader sarcoma spectrum, providing an unappreciated link between RMS and EFT.

Based on our findings, EFT-like undifferentiated SRCS can arise from lineage-restricted Myf5^{+}, aP2^{+}, or postnatal Pax7^{+} cells. Even though cell of origin contributes to outcome, mutational profile may be the principal driver dictating tumor phenotype. For instance, activation of Shh signaling in the *Myf5*^{Cre} lineage using *Ptch* deletion induces RMS in <5% of mice (Nitzki et al., 2011), while activation with *SmoM2* is embryonic lethal (Hatley et al., 2012). Elsewhere, *Myf5*^{Cre}*; p53*$^{-/-}$*; Ptch*$^{+/-}$ mice were reported to develop multiple sarcoma types, including RMS, pleomorphic sarcoma and osteosarcoma, similar to postnatal activation of Shh signaling in *Pax7-creER; p53*$^{-/-}$*; Ptch*$^{+/-}$ mice (Rubin et al., 2011). Interestingly, *Ptch* deletion in these studies acted as a strong modifier of tumor phenotype, favoring myogenic differentiation over undifferentiated

entities mostly seen in *Myf5^{Cre}; p53$^{-/-}$* and *Pax7-creER; p53$^{-/-}$* mice (Rubin et al., 2011). No doubt, the level at which Shh pathway activation occurs is a critical determinant of outcome, but mechanisms driving such divergent phenotypes are not clear.

Reaching different thresholds of pathway activation may invoke distinctive modes of action for downstream mediators. We know that in the developing embryo, induction of *Myf5* expression by Shh is required for epaxial muscle specification (Gustafsson et al., 2002). Since the expression of the primary myogenic regulatory factors (MRFs), Myf5 and MyoD, is required for production of Myogenin^{+} myoblasts (Sabourin and Rudnicki, 2000), which are a hallmark of RMS, it seems fitting that aberrant Shh pathway activity in precursors of muscle can drive the formation of myogenic RMS.

However, it is counterintuitive that the same oncogenic force could also drive the formation of an undifferentiated SRCS, like EFT. A possible explanation underlying this finding could be that higher level pathway activity mediated by GLI2ΔN could activate Nkx2.2, which is currently the most reliable molecular marker for EFT and is itself an important mediator of sarcomagenesis (Smith et al., 2006; Yoshida et al., 2012). Indeed, Nkx2.2 is a known Shh transcriptional target in the ventral neural tube (Vokes et al., 2007) where Shh dosage is the strongest and Gli2 primarily mediates target gene expression (Cho et al., 2008; Eggenschwiler et al., 2006; Matise et al., 1998). Induction of ectopic Nkx2.2 by GLI2 could be a critical step towards promoting an EFT-like phenotype. Furthermore, the absence of Nkx2.2 expression in RMS may stem from an insufficient level of Shh pathway activation. An additional possibility is direct repression of

myogenic differentiation by Gli-mediated blockade of MRF activation, since Gli1/ Gli2 have been shown elsewhere to block transcriptional activity of Myf5 and MyoD (Gerber et al., 2007).

PCG2 SRCS are distinct from other Shh-driven tumors

Other studies have compared *SmoM2* and *CLEG2* alleles to investigate aberrant Shh pathway activity in medulloblastoma and basal cell carcinoma (Han et al., 2009; SY et al., 2009). In both cases, when *SmoM2* was used the resulting tumors were widely ciliated, similar to *PCG2* EFT-like SRCS. However, it was found that the primary cilium potently represses GLI2ΔN function; only in the absence of primary cilia could GLI2ΔN fully promote medulloblastoma or basal cell carcinoma formation. Thus it is surprising that GLI2ΔN mediates such potency despite the ciliated status of *PCG2* tumors. It is important to note that human EFT specimens are ciliated (not shown). However, this conundrum begs the question, could *PCG2* tumor phenotype be modified in the absence of primary cilia beyond potential changes in aggressiveness? This query could easily be resolved by ablating primary cilia with conditional deletion of either Kif3a or IFT88 floxed alleles. However, this repressive effect may be cell type-dependent, explaining why Purkinje neuron defects were not apparent in *PCG2* animals.

CLEG2 has also been used to model pancreatic carcinoma, and when activated in the pancreatic epithelium induces neoplasia, categorized as undifferentiated carcinoma lacking any character of differentiated pancreatic cells types. However, only when combined with an activating Kras mutation ($Kras^{G12D}$) was *CLEG2* able to recapitulate the earliest stages of pancreatic ductal adenocarcinoma (PDA) (Pasca di Magliano et al., 2006). Elsewhere, studies using *SmoM2* targeted to the pancreatic epithelium found this oncogene was not able to induce neoplasia,

providing an additional example that the level of Shh pathway activation can mediate very different tumor outcomes (Tian et al., 2009). Hopefully, our studies will open up important new territory for cancer researchers. Altogether our work identified GLI2 as a key mediator of EFT sarcomagenesis acting downstream of EWS-FLI1, highlighting GLI2 as a potential therapeutic target in EFT. Thus our mouse models offer a variety of powerful systems in which to evaluate EFT-targeted therapeutic agents.

CHAPTER V

FUTURE DIRECTIONS

A useful measurement that weighs the relative impact of a study is to determine how many subsequent studies and findings to which it ultimately leads. The two projects I described in CHAPTERS III to IV will hopefully lead to many more interesting and important discoveries. Here, I will attempt to outline the next steps I would take to follow up these studies and where I anticipate their respective trajectories leading.

In CHAPTER II, I described a population of Shh-responding, proliferative GABAergic precursors in the cerebellar PWM niche that express transcription factor Ptf1a (**Figure 3.1H', I**). Previously, Ptf1a function in the developing CNS has been linked only to fate specification, and Ptf1a^{+} cells were thought to be exclusively post-mitotic (Hoshino et al., 2005; Pascual et al., 2007). My findings revealed an important mechanism supporting the rapid accumulation of GABAergic precursor cells in the PWM, driven by Ptf1a^{+} transient amplifying cells. Although these precursors respond to Shh, we cannot be entirely certain that this signal functions to induce proliferation. Although I ablated Shh reception in the parent progenitor population using *Tnc*$^{YFP\text{-}CreER}$ mice and subsequently found a near complete loss of Ptf1a^{+} precursors (**Figure 3.9E, F, N**), I never directly removed Shh reception in Ptf1a^{+} cells. Therefore, it would be fascinating to delete Smo using *Ptf1a*^{Cre} or *Ptf1a*^{CreER} mice to determine whether Shh acts as a proliferative signal or if it plays an additional role, such as in lineage or fate specification.

I would incorporate a reporter strain, such as *Rosa*^{eYFP}, to track descendants of recombined Ptf1a^{+} parent cells. Most likely, I would find a reduction in the proliferative capacity of the latter population, causing a reduction in ML GABAergic inhibitory interneurons that I have found to descend from them (**Figure 3.2C**). This outcome may cause a general loss of both ML interneuron subtypes (basket and stellate cells), or may be skewed towards a preferential loss of stellate cells, the later born subtype. Another possible outcome could be a fate change in Ptf1a^{+}, *Smo*$^{F/-}$ mutant cells in which they revert to a glial precursor-like cell. I reported that GABAergic interneurons are co-generated in the PWM alongside astrocytes (**Figure 3.3H, I**), so it would be interesting to learn that Shh signaling also functions in Ptf1a^{+} cells to maintain them on the path to neuronal fate.

A more complete time-course to elaborate on when Ptf1a^{+} cells divide in the PWM is key for understanding Shh function. Even though I demonstrated that Shh-responding cells divide in the PWM at P3 and P5, they represent multiple subpopulations; including CD133^{+} multi-potent primary progenitors, Ptf1a^{+} transient amplifying cells and CD15^{+} astrocyte intermediate progenitors (**Figure 3.14G**). It is unclear when or if Shh-responding, Ptf1a^{+} cells divide. Additionally, Shh signaling appears to be undetectable by P6 when I found that a fraction of Ptf1a^{+} cells in general are dividing. Therefore, room for anticipating multiple possible outcomes exists, all of which are exciting to consider. Shh signaling might initiate and maintain the majority of cellular divisions occurring in the Ptf1a^{+} population, but it may also, or alternatively, specify GABAergic fate by inducing the expression of pro-neural transcription factors like Ptf1a itself. Certainly, many important details and functions remain to be described.

Even though the exact function of Shh signaling in Ptf1a^{+} cells is uncertain, ablating this signaling relationship would be expected to somehow disrupt the integration of ML inhibitory interneurons into the cerebellar circuit. These cells maintain connectivity with PNs, the sole projection neuron in the cerebellum, and provide inhibitory feedback, thus playing an important role in balancing excitatory/ inhibitory signaling (Sillitoe and Joyner, 2007). Shh plays an important part in orchestrating the formation of a completely wired and balanced neuronal network (Fleming et al., 2013). Because imbalances in excitatory/ inhibitory signaling are a hallmark feature of neuropsychiatric disorders, including autism, we could extend our studies to include evaluating whether PN activity is altered in our genetic mutant system using electrophysiology (Ramamoorthi and Lin, 2011).

Indeed, early collaborative work with the Danny Winder laboratory at VUMC has allowed us to successfully perform attached whole cell patched clamping of PNs to record spontaneous inhibitory postsynaptic currents (IPSCs). The use of Ptf1a-driven deletion of Smo is highly amenable to such studies because overall cerebellar cortical architecture would likely be intact, unlike the *Tnc$^{YFP\text{-}CreER}$; Smo$^{F/-}$* mutants I described in CHAPTER III, which display some cerebellar hypoplasia and cortical layering defects. The analyses I am proposing here could be combined with neuro-behavioral assays to more firmly link Shh function, and the PN, to the origin of neurodevelopmental disorders like autism.

In addition to the relationship between Ptf1a^{+} cells and Shh that I found in the PWM, two other Shh-responding populations I described there are Tnc$^{YFP\text{-}low}$, CD133^{+} primary progenitors and Tnc$^{YFP\text{-}low}$, CD15^{+} astrocyte precursors (**Figure 3.14G**). Further evaluation of these cells and their

specific requirements for Shh is warranted. I refer to Tnc$^{YFP\text{-}low}$, CD133^{+} cells as primary progenitors because they appear to be multi-potent, stem cell-like parent cells generating both Ptf1a^{+} and Tnc$^{YFP\text{-}low}$, CD15^{+} cell types. Similar to Ptf1a^{+} cells, I found that CD15^{+} cells are largely absent in the PWM of *Tnc$^{YFP\text{-}CreER}$; Smo$^{F/-}$* mutants (**Figure 3.11B, D**). It is difficult to say exactly why this occurs. The easy explanation would be that Tnc$^{YFP\text{-}low}$, CD15^{+} cells require Shh to provide a mitogenic signal, inducing their proliferation and expansion of the CD15^{+} astrocyte progenitor pool. Alternatively, however, these cells may prematurely differentiate, and a similar conundrum also exists for Tnc$^{YFP\text{-}low}$, CD133^{+} cells following Smo ablation. These cells could either fail to sufficiently divide and propagate downstream progenitor subpopulations or they could perhaps lose their stem cell identity and prematurely differentiate. Based on my characterization of *Tnc$^{YFP\text{-}CreER}$; Smo$^{F/-}$* mutants so far it is hard to say which scenario is the right one, although I am confident that loss of viability is not a major factor for any of the above populations based on my findings in CHAPTER III.

Though somewhat challenging, an elegant strategy to tease apart any such cell-type specific functions for Shh would be transplantation studies. To that end, FACS could be used to separately isolate Tnc$^{YFP\text{-}low}$, CD15^{+} and Tnc$^{YFP\text{-}low}$, CD133^{+} populations from both WT *Tnc$^{YFP\text{-}CreER}$* and *Tnc$^{YFP\text{-}CreER}$; Smo$^{F/-}$* mutant mice. Additionally, I would incorporate the *Ai9* reporter strain to express an indelible tdTomato fluorophore to track recombined cells, which could then be transplanted into WT littermate recipients using stereotactic micro-injections.

Having gained new insight into the distinct progenitor subpopulations occupying the neonatal cerebellar PWM raised intrigue regarding the medulloblastoma cell of origin. Currently, mouse

models indicate that medulloblastomas can arise from multi-potent cerebellar stem cells or granule cell committed precursors (Read et al., 2009; Sutter et al., 2010; Yang Z, 2008). A valid question to address now is whether $Tnc^{YFP\text{-}low}$, $CD15^{+}$ and/ or $Tnc^{YFP\text{-}low}$, $CD133^{+}$ cells could be transformed by oncogenic Shh pathway activation, leading to medulloblastoma. First, *$Tnc^{YFP\text{-}CreER}$; SmoM2* mice could be administered TM and kept for observation. Such a strategy should indicate whether this outcome is possible or not. If so, the next step would be to dissect which progenitor, $Tnc^{YFP\text{-}low}$, $CD15^{+}$or $Tnc^{YFP\text{-}low}$, $CD133^{+}$ cells serve as tumor initiating cells. To this end, the above populations could be isolated from *$Tnc^{YFP\text{-}CreER}$; SmoM2* mice using FACS and transplanted into WT recipients.

Another important future direction to consider is determining the mechanism by which PNs distribute Shh ligand over such a distance in two directions. The dissemination of Shh to the overlying EGL was first described in 1999 (Wechsler-Reya and Scott, 1999), but still we do not really understand how the molecule reaches such a distant target field two cortical layers away. It has been suggested that PN dendrites, which project towards the surface of the cerebellum, are the basis for Shh distribution (Lewis P.M., 2004). I found that PNs simultaneously transmit Shh inward to the PWM, and it appears that this likely occurs by utilizing PN axons that descend directly to the cerebellar core (**Figure 3.12A-C'**). It may be the case that these nascent neuronal projections aid in shuttling Shh bi-directionally, recent studies have shown that Shh-producing mesenchymal cells situated in the posterior compartment of the developing limb bud project dynamic filapodia to transmit Shh to receiving cells in the anterior compartment (Sanders et al., 2013).

These specialized filapodial structures are highly dynamic and visualizing them requires live cell imaging, since traditional fixation methods apparently do not preserve them well. It is possible that PNs utilize a similar structure for transmitting Shh to the EGL. I have attempted to determine whether such a structure can be detected using a membrane-targeted YFP reporter (*mT/mG*) crossed to the Shh^{Cre} driver. Using fixed tissues, PNs from Shh^{Cre}*; mT/mG* cerebella appear to project long, thin structures into the overlying EGL, that are distinct from dendrites. Our lab has initiated studies utilizing live cell imaging on cerebellar slices from Shh^{Cre}*; Ai9* mice and indeed, we have been able to visualize very long, thin PN projections that, to our knowledge, have not been reported anywhere in the literature. Our next step is to continue live cell imaging, but using Shh^{Cre}*; mT/mG* and/ or *L7(Pcp2)-cre; mT/mG* mice that should provide more stable and complete labeling of any membrane-bound cellular projections.

Though these approaches should allow us to detect and study PN projections, they will not tell us about Shh ligand localization. To understand dynamics of Shh transmission, we can combine live cell imaging techniques with genetic studies and stereotactic micro-injections to deliver lentiviral-encoded, fluorophore tagged versions of Shh expressed under control of the L7(Pcp2) promoter. I have learned to perform these injections and have mapped coordinates to allow for reproducible injections into the neonatal cerebellum. These approaches should allow us to study distribution of PN-derived Shh in real time. It may be possible to simply culture live cerebellar slices in virus prior to imaging. However, once we have established a basic understanding of Shh transmission in the growing cerebellum, we can move toward genetic studies to uncover what molecules support this process.

Our lab has developed a conditional allele for Dispatched (Disp), a molecule thought to be required for Shh secretion and juxtacrine signaling (Kawakami et al., 2002). No doubt we could move our live imaging studies into a Disp mutant context; *L7(Pcp2)-cre; Disp*$^{F/-}$ versus *L7(Pcp2)-cre; Disp*$^{F/+}$ littermates. To dissect mechanism(s) by which Shh could be targeted to and transmitted along the PN axon, conditional mutants for relevant microtubule-based motor proteins could be utilized. Kinesin-II, for instance, plays important roles in transporting cargoes along axons, and a floxed allele for the motor subunit, Kif3a, is readily accessible. Without a doubt, there are many avenues of inquiry left to follow up on the work in CHAPTER III; the difficult task may be prioritizing where to look first.

The studies in CHAPTER IV describing mouse sarcoma models and possible function for Gli2 in the etiology of EFT no doubt also highlight several future studies. The evidence indicating that GLI2 is likely an important mediator of EFT sarcomagenesis so far is limited; we know that GLI2 expression occurs at a high level in a substantial cohort of human EFT samples (n=154), and that ChIP-seq indicates that the EWS-FLI1 oncoprotein binds two regions on human Gli2, where it may act to induce GLI2 expression (**Figure 4.7A-D**). These data are strongly suggestive of a role for Gli2 in EFT, and furthermore our mouse modeling indicates that activation of Gli2 alone is sufficient to drive EFT formation. However, several key issues remain unresolved in order to firmly document an EWS-FLI1 - Gli2 interaction, and to test whether Gli2 is indeed required in these tumors. In the long run, the application of our mouse model for screening potential therapeutic compounds should be considered.

So far we have mapped 21 potential EWS-FLI1 binding motifs distributed between two regions (1.8 kb and 1.7 kb) on human Gli2 that display the H3K27ac mark indicative of an active enhancer (Creyghton et al., 2010). The obvious next step is to perform ChIP experiments to clearly demonstrate that EWS-FLI1 does in fact bind GLI2. If binding can be demonstrated, then a next step would be testing whether EWS-FLI1 is sufficient to activate GLI2 expression via binding to these two regions. The latter can be cloned into the pGL3-promoter luciferase reporter construct, which would then be transfected into TC32, TC71, and A673 human EFT cells lines known to carry the EWS-FLI1 chimera for a cell-based reporter assay to measure GLI2 activation. We can then knockdown EWS-FLI1 in TC32, TC71, and A673 EFT cells lines and measure whether this affects GLI2 expression and subsequent protein levels. EWS-FLI1 knockdown can also be used as a control for ChIP experiments to assess whether binding to GLI2 is indeed EWS-FLI1 - mediated.

Though these experiments will clearly indicate if EWS-FLI1 can directly activate GLI2, such data would not indicate if GLI2 activation is actually required for EFT formation. To address this question I would utilize a stable GLI2 knockdown in EFT cell lines that would then be used in xenograft studies with an established gastrocnemius transplantation model. Based on my data so far, I would anticipate a robust decrease in tumor forming potential with attenuated GLI2 function. Altogether, these data would demonstrate that GLI2 is both necessary and sufficient for EFT formation.

Because EFT data are not available through TCGA (the cancer genome atlas) yet, and extensive comparison of currently available microarray datasets with our RNA-seq results is problematic, I

plan to perform comparisons of expression profiles from *PCG2* tumors and EFT cell lines, TC32, TC71, and A673 once the latter become available through our collaborator, Patrick Grohar, MD, PhD. Such analyses will permit a more complete genome-wide comparison between our mouse model and human EFT, perhaps providing important further confirmation regarding the placement of our mouse model in the Ewing's family. It may also help us gain insight into the differential regulation of target genes between GLI2 alone and EWS-FLI1. Such data could prove very helpful in understanding differences between the two entities, such as tumor aggressiveness, drug sensitivity, and site of tumor origin. In addition to soft tissue, EFT is also known to occur in the bone, something we have not seen in our mouse model. Expression data could be one approach to reconcile this difference. Fate-mapping studies of the *L7(Pcp2)-cre* lineage did indicate some contribution to bone, so it may seem somewhat strange that tumors never target bone in this model. EWS-FLI1 transcriptional regulation may impart different properties to tumors than GLI2 alone, allowing for differences such as this one.

It is not really clear why so many past attempts to generate an EFT mouse model based on the EWS-FLI oncoprotein were not successful (Lin et al., 2008; Torchia et al., 2007), but one likely reason is the inherent lethality of oncoproteins (Haldar et al., 2007; Haldar et al., 2009; Straessler et al., 2013). Another possibility is that investigators have not identified the appropriate cellular lineage to target. Therefore, it would be worthwhile to create our own Rosa26-EWS-FLI1 mouse to cross with the *L7(Pcp2)-cre* driver used in our study. No one, so far, has targeted the EFT oncoprotein to this lineage, and it may be key to creating a *bona fide* EFT mouse using the most defining feature of Ewing's, EWS-FLI1. Having this reagent would also allow us to further

elucidate the EFT cell of origin, since we could cross it with all the driver lines described in CHAPTER IV; *Pax7-creER*, *Myf5*^{Cre}, *aP2-cre* and other available lines that we have not yet tried.

A major conceptual realization to which my sarcoma studies have led, is that the level of Shh pathway activation dictates the resulting sarcoma phenotype; others have shown that activation at the level of Patched1/ Smo leads to RMS and now my work indicates that activation at the level of Gli2 induces EFT. To support this idea, it is important to differentially activate the pathway in the same lineage, to rule out the possibility that cellular origin contributes to tumor phenotype. A previously documented mouse model for RMS is the *aP2-cre; SmoM2* mouse (Hatley et al., 2012), which targets the adipocyte lineage similar to the *aP2-cre; CLEG2* mice I described in CHAPTER IV. Even though we already know the outcome of generating *aP2-cre; SmoM2* mice, having them would allow us to perform genome-wide RNA expression profiling between the two tumor types. Identifying the most highly, differentially expressed genes might lead us to find useful biomarkers to help further distinguish these two sarcoma variants. Additionally, we may be able to better understand what other factors shape the specific sarcoma phenotypic outcome, and even uncover potential therapeutic targets.

Perhaps the most significant application for a mouse tumor model is in drug screening to test potential therapeutic compounds. While cells lines are more conducive to large-scale drug screens, mouse models can offer a powerful system to further evaluate promising compounds, understand their respective toxicities, etc. If the *PCG2* model is truly an accurate recapitulation of EFT, then it should prove useful in testing compounds uncovered in screens utilizing human EFT cell lines. For instance, our collaborator Patrick Grohar has developed a compound that

blocks the DNA-binding of EWS-FLI1 to target genes (Grohar et al., 2011). Another collaborator at VUMC, Charles Hong, MD, PhD has developed a currently unpublished compound, Egmanone, which appears to inhibit the Shh pathway by disrupting Gli2 activity. Our lab has extensive unpublished data on a known compound called AICAR, which we have found potently blocks Gli2 function. Clearly, there is much further work that can be done with *PCG2* mice in the short term, without having to identify new compounds. To track tumor progression/ regression in real time, we have obtained a Gli1-luciferase reporter mouse that can provide an accurate read-out for pathway activity using bioluminescent, live animal imaging.

Currently, there is a major need in the field for inhibitors of the Shh pathway that act downstream of Smo, where the action of most established inhibitors is targeted. The clinical application of Smo inhibitors has not been met with great success. For example, treatment of medulloblastoma using a Smo inhibitor from Genentech, GDC-0449, initially reduced one terminal patient's tumor burden to an undetectable level. However, his cancer acquired a secondary mutation that blocked GDC-0449 activity, allowing a much more aggressive cancer to emerge (Yauch et al., 2009). Ideally, a combined approach to block pathway activity at multiple levels will be the future of targeted therapy. The generation of *PCG2* mice came at what seems to be good timing, and the potential contribution that could be made with *PCG2* mice to developing such approaches hopefully will be substantial.

BIBLIOGRAPHY

Ahn, S., and Joyner, A.L. (2004). Dynamic changes in the response of cells to positive hedgehog signaling during mouse limb patterning. Cell *118*, 505-516.

Ahn, S., and Joyner, A.L. (2005). In vivo analysis of quiescent adult neural stem cells responding to Sonic hedgehog. Nature *437*, 894-897.

Altman J, B.S. (1997). Development of the Cerebellar System in relation to its evolution, structure, and function. (Indianapolis, CRC Press).

Alvarez-Buylla, A., Garcia-Verdugo, J.M., and Tramontin, A.D. (2001). A unified hypothesis on the lineage of neural stem cells. Nat Rev Neurosci *2*, 287-293.

Ashwell, K.W., and Mai, J.K. (1997). A transient CD15 immunoreactive sling in the developing mouse cerebellum. Int J Dev Neurosci *15*, 883-889.

Bai C.B., A.W., Lee J.S., Stephen D., Joyner A.L. (2002). Gli2, but not Gli1, is required for initial Shh signaling and ectopic activation of the Shh pathway Development *129*, 4753-4761.

Beauchamp, E., Bulut, G., Abaan, O., Chen, K., Merchant, A., Matsui, W., Endo, Y., Rubin, J.S., Toretsky, J., and Uren, A. (2009). Gli1 Is a Direct Transcriptional Target of EWS-FLI1 Oncoprotein. The Journal of Biological Chemistry *284*, 9074-9082.

Beauchamp, J.R., Heslop, L., Yu, D.S., Tajbakhsh, S., Kelly, R.G., Wernig, A., Buckingham, M.E., Partridge, T.A., and Zammit, P.S. (2000). Expression of CD34 and Myf5 defines the majority of quiescent adult skeletal muscle satellite cells. J Cell Biol *151*, 1221-1234.

Brownell, I., Guevara, E., Bai, C.B., Loomis, C.A., and Joyner, A.L. (2011). Nerve-derived sonic hedgehog defines a niche for hair follicle stem cells capable of becoming epidermal stem cells. Cell Stem Cell *8*, 552-565.

Capela, A., and Temple, S. (2002). LeX/ssea-1 Is Expressed by Adult Mouse CNS Stem Cells, Identifying Them as Nonependymal. Neuron *35*, 865-875.

Catini, M., Jones, D., and Daly, E. (2008). Altered cerebellar feedback projections in Asperger syndrome. Neuroimage *41*, 1184-1191.

Chen, J.K., Taipale, J., Young, K.E., Maiti, T., and Beachy, P.A. (2002). Small molecule modulation of Smoothened activity. Proc Natl Acad Sci U S A *99*, 14071-14076.

Chiang, C., Swan, R.Z., Grachtchouk, M., Bolinger, M., Litingtung, Y., Robertson, E.K., Cooper, M.K., Gaffield, W., Westphal, H., Beachy, P.A., *et al*. (1999). Essential role for Sonic hedgehog during hair follicle morphogenesis. Dev Biol *205*, 1-9.

Chiang, C., Y., L., Lee, E., Young, K.E., Cordent, J.L., Westphal, H., and Beachy, P.A. (1996). Cyclopia and defective axial patterning in mice lacking sonic hedgehog gene funciton. Nature *383*, 407-413.

Cho, A., Ko, H.W., and Eggenschwiler, J.T. (2008). FKBP8 cell-autonomously controls neural tube patterning through a Gli2- and Kif3a-dependent mechanism. Dev Biol *321*, 27-39.

Cooper, M.K., Porter, J.A., Young, K.E., and Beachy, P.A. (1998). Teratogen-mediated inhibition of target tissue response to Shh signaling. Science *280*, 1603-1607.

Cornelison, D.D., and Wold, B.J. (1997). Single-cell analysis of regulatory gene expression in quiescent and activated mouse skeletal muscle satellite cells. Dev Biol *191*, 270-283.

Corrales, J.D., Blaess, S., Mahoney, E.M., and Joyner, A.L. (2006). The level of sonic hedgehog signaling regulates the complexity of cerebellar foliation. Development *133*, 1811-1821.

Corrales JD, R.G., Blaess S, Guo Q, Joyner AL (2004). Spatial pattern of sonic hedgehog signaling through Gli genes during cerebellum development. Development *131*, 5581-5590.

Creyghton, M.P., Cheng, A.W., Welstead, G.G., Kooistra, T., Carey, B.W., Steine, E.J., Hanna, J., Lodato, M.A., Frampton, G.M., Sharp, P.A., *et al*. (2010). Histone H3K27ac separates active from poised enhancers and predicts developmental state. Proc Natl Acad Sci U S A *107*, 21931-21936.

Dahmane, N., and Ruiz i Altaba, A. (1999). Sonic hedgehog regulates the growth and patterning of the cerebellum. Development *126*, 3089-3100.

Doetsch, F. (2003). A niche for adult neural stem cells. Curr Opin Genet Dev *13*, 543-550.

Eggenschwiler, J.T., Bulgakov, O.V., Qin, J., Li, T., and Anderson, K.V. (2006). Mouse Rab23 regulates hedgehog signaling from smoothened to Gli proteins. Dev Biol *290*, 1-12.

Feil, R., Wagner, J., Metzger, D., and Chambon, P. (1997). Regulation of Cre recombinase activity by mutated estrogen receptor ligand-binding domains. Biochem Biophys Res Commun *237*, 752-757.

Fleming, J.T., He, W., Hao, C., Ketova, T., Pan, F.C., Wright, C.C.V., Litingtung, Y., and Chiang, C. (2013). The Purkinje Neuron Acts as a Central Regulator of Spatially and Functionally Distinct Cerebellar Precursors. Developmental cell *27*, 278-292.

Fletcher, C.D.M., Chibon, F., and Mertens, F. (2013). Undifferentiated/ unclassified sarcomas. In WHO Classification of Tumours of Soft Tissue and Bone, C.D.M. Fletcher, J.A. Bridge, P.C.W. Hogendoorn, and F. Mertens, eds. (Lyon), pp. 236-238.

Fuccillo, M., Joyner, A.L., and Fishell, G. (2006). Morphogen to mitogen: the multiple roles of hedgehog signalling in vertebrate neural development. Nat Rev Neurosci *7*, 772-783.

Garcia, A.D., Petrova, R., Eng, L., and Joyner, A.L. (2010). Sonic hedgehog regulates discrete populations of astrocytes in the adult mouse forebrain. J Neurosci *30*, 13597-13608.

Gerber, A.N., Wilson, C.W., Li, Y.J., and Chuang, P.T. (2007). The hedgehog regulated oncogenes Gli1 and Gli2 block myoblast differentiation by inhibiting MyoD-mediated transcriptional activation. Oncogene *26*, 1122-1136.

Gillig, P.M., and Sanders, R.D. (2010). Pychriatry, Neurology, and the Role of the Cerebellum. Pychriatry *7*, 38-43.

Goodrich, L.V., Milenkovic, L., Higgins, K.M., and Scott, M.P. (1997). Altered neural cell fates and medulloblastoma in mouse patched mutants. Science *277*, 1109-1113.

Grimaldi, P., Parras, C., Guillemot, F., Rossi, F., and Wassef, M. (2009). Origins and control of the differentiation of inhibitory interneurons and glia in the cerebellum. Dev Biol *328*, 422-433.

Grohar, P.J., Woldemichael, G.M., Griffin, L.B., Mendoza, A., Chen, Q.R., Yeung, C., Currier, D.G., Davis, S., Khanna, C., Khan, J., *et al*. (2011). Identification of an inhibitor of the EWS-FLI1 oncogenic transcription factor by high-throughput screening. J Natl Cancer Inst *103*, 962-978.

Gustafsson, M.K., Pan, H., Pinney, D.F., Liu, Y., Lewandowski, A., and Epstein, D.J. (2002). Myf5 is a direct target of long-range Shh signaling and Gli regulation for muscle specification. Genes Dev *16*, 114-126.

Hahn, H., Wojnowski, L., Zimmer, A.M., Hall, J., Miller, G., and Zimmer, A. (1998). Rhabdomyosarcomas and radiation hypersensitivity in a mouse model of Gorlin syndrome. Nat Med *4*, 619-622.

Hald, J., Sprinkel, A.E., Ray, M., Serup, P., Wright, C., and Madsen, O.D. (2008). Generation and characterization of Ptf1a antiserum and localization of Ptf1a in relation to Nkx6.1 and Pdx1 during the earliest stages of mouse pancreas development. J Histochem Cytochem *56*, 587-595.

Haldar, M., Hancock, J.D., Coffin, C.M., Lessnick, S.L., and Capecchi, M.R. (2007). A Conditional Mouse Model of Synovial Sarcoma: Insights into a Myogenic Origin. Cancer Cell *11*, 375-388.

Haldar, M., Hedberg, M.L., Hockin, M.F., and Capecchi, M.R. (2009). A CreER-based random induction strategy for modeling translocation-associated sarcomas in mice. Cancer Res *69*, 3657-3664.

Han, Y.G., Kim, H.J., Dlugosz, A.A., Ellison, D.W., Gilbertson, R.J., and Alvarez-Buylla, A. (2009). Dual and opposing roles of primary cilia in medulloblastoma development. Nat Med *15*, 1062-1065.

Hatley, M.E., Tang, W., Garcia, M.R., Finkelstein, D., Millay, D.P., Liu, N., Graff, J., Galindo, R.L., and Olson, E.N. (2012). A mouse model of rhabdomyosarcoma originating from the adipocyte lineage. Cancer Cell *22*, 536-546.

Hatten, M.E., and Heintz, N. (1995). Mechanisms of neural patterning and specification in the developing cerebellum. Annu Rev Neurosci *18*, 385-408.

Haycraft C, Banizs B, Aydin-Son Y, Zhang Q, Michaud E, and B, Y. (2005). Gli2 and Gli3 Localize to Cilia and require the intraflagellar transport protein polaris for processing and function. PLoS Genet *1*.

Hoshino, M., Nakamura, S., Mori, K., Kawauchi, T., Terao, M., Nishimura, Y.V., Fukuda, A., Fuse, T., Matsuo, N., Sone, M., *et al*. (2005). Ptf1a, a bHLH transcriptional gene, defines GABAergic neuronal fates in cerebellum. Neuron *47*, 201-213.

Huang X., Liu J., Ketova Tatiana K., Fleming J.T., Grover V.K., Cooper M.K., Litingtung Y., and Chiang, C. (2010). Transventricular delivery of Sonic hedgehog is essential to cerebellar ventricular zone development. PNAS *107*, 8422-8427.

Huang, Z., and Kunes, S. (1996). Hedgehog, transmitted along retinal axons, triggers neurogenesis in the developing visual centers of the Drosophila brain. Cell *86*, 411-422.

Huangfu, D., and Anderson, K.V. (2005). Cilia and Hedgehog responsiveness in the mouse. Proc Natl Acad Sci U S A *102*, 11325-11330.

Ihrie, R.A., Shah, J.K., Harwell, C.C., Levine, J.H., Guinto, C.D., Lezameta, M., Kriegstein, A.R., and Alvarez-Buylla, A. (2011). Persistent sonic hedgehog signaling in adult brain determines neural stem cell positional identity. Neuron *71*, 250-262.

Ingham PW, M.A. (2001). Hedgehog signaling in animal development: paradigms and principles. . Gene and Development *15*, 3059-3087.

Jedlicka, P. (2010). Ewing Sarcoma, an enigmatic malignancy of likely progenitor cell origin, driven by transcription factor oncogenic fusions. Int J Clin Exp Pathol *3*, 338-347.

Joo, J., Christensen, L., Warner, K., States, L., Kang, H., Vo, K., Lawlor, E.R., and May, W.A. (2009). GLI1 Is a Central Mediator of EWS/FLI1 Signaling in Ewing Tumors. PLoS One *4*.

Kawakami, T., Kawcak, T., Li, Y.J., Zhang, W., Hu, Y., and Chuang, P.T. (2002). Mouse dispatched mutants fail to distribute hedgehog proteins and are defective in hedgehog signaling. Development *129*, 5753-5765.

Keller, C., Arenkiel, B.R., Coffin, C.M., El-Bardeesy, N., DePinho, R.A., and Capecchi, M.R. (2004). Alveolar rhabdomyosarcomas in conditional Pax3:Fkhr mice: cooperativity of Ink4a/ARF and Trp53 loss of function. Genes Dev *18*, 2614-2626.

Kenney, A.M., and Rowitch, D.H. (2000). Sonic hedgehog promotes G(1) cyclin expression and sustained cell cycle progression in mammalian neuronal precursors. Mol Cell Biol *20*, 9055-9067.

Kikuchi, K., Rubin, B.P., and Keller, C. (2011). Developmental origins of fusion-negative rhabdomyosarcomas. Curr Top Dev Biol *96*, 33-56.

Klein, C., Butt, S.J.B., Machold, R.P., Johnson, J.E., and Fishell, G. (2005). Cerebellum and forebrain derived stem cells possess intrinsic regional character. Development *132*, 4497-4508.

Kondo, T., and Raff, M. (2000). Oligodendrocyte precursor cells reprogrammed to become multipotential CNS stem cells. Science *289*, 1754-1757.

Koster, J. (2008). R2: microarray analysis and visualization platform (Amsterdam, AMC).

Kuang, S., Kuroda, K., Le Grand, F., and Rudnicki, M.A. (2007). Asymmetric self-renewal and commitment of satellite stem cells in muscle. Cell *129*, 999-1010.

Lee, A., Kessler, J.D., Read, T.A., Kaiser, C., Corbeil, D., Huttner, W.B., Johnson, J.E., and Wechsler-Reya, R.J. (2005). Isolation of neural stem cells from the postnatal cerebellum. Nat Neurosci *8*, 723-729.

Lessnick, S.L., Dei Tos, A.P., Sorensen, P.H., Dileo, P., Baker, L.H., Ferrari, S., and Hall, K.S. (2009). Small round cell sarcomas. Semin Oncol *36*, 338-346.

Leto, K., Bartolini, A., and Rossi, F. (2010). The prospective white matter: an atypical neurogenic niche in the developing cerebellum. Arch Ital Biol *148*, 137-146.

Leto, K., Bartolini, A., Yanagawa, Y., Obata, K., Magrassi, L., Schilling, K., and Rossi, F. (2009). Laminar fate and phenotype specification of cerebellar GABAergic interneurons. J Neurosci *29*, 7079-7091.

Leto K, C.B., Williams IM, Magrassi L, Rossi F (2006). Different types of cerebellar GABAergic interneurons originate from a common pool of multipotent progenitor cells. J Neurosci *26*, 11682-11694.

Lewis P.M., D.M.P., McMahon J.A., Logan M., Martin J.F., St-Jacques B., McMahon A.P. (2001). Cholesterol modification of sonic hedgehog is required for long-range signaling activity and effective modulation of signaling by Ptc1. Cell *105*, 599-612.

Lewis P.M., G.-L.A., Smeyne R., Kottmann A., McMahon A.P. (2004). Sonic hedgehog signaling is required for expansion of granule neuron precursors and patterning of the mouse cerebellum. Development Biology *270*, 393-410.

Li, Y., Zhang, H., Litingtung, Y., and Chiang, C. (2006). Cholesterol modification restricts the spread of Shh gradient in the limb bud. Proc Natl Acad Sci U S A *103*, 6548-6553.

Lin, P.P., Pandey, M.K., Jin, F., Xiong, S., Deavers, M., Parant, J.M., and Lozano, G. (2008). EWS-FLI1 induces developmental abnormalities and accelerates sarcoma formation in a transgenic mouse model. Cancer Res *68*, 8968-8975.

Liu, F., Walmsley, M., Rodaway, A., and Patient, R. (2008). Fli1 acts at the top of the transcriptional network driving blood and endothelial development. Current Biology *18*, 1234-1240.

Liu, J., Li, Q., Kuehn, M.R., Litingtung, Y., Vokes, S.A., and Chiang, C. (2013). Sonic hedgehog signaling directly targets Hyaluronic Acid Synthase 2, an essential regulator of phalangeal joint patterning. Dev Biol *375*, 160-171.

Long, F., Zhang, X.M., Karp, S., Yang, Y., and McMahon, A.P. (2001). Genetic manipulation of hedgehog signaling in the endochondral skeleton reveals a direct role in the regulation of chondrocyte proliferation. Development *128*, 5099-5108.

Lorenz, A., Deutschmann, M., Ahlfeld, J., Prix, C., Koch, A., Smits, R., Fodde, R., Kretzschmar, H.A., and Schuller, U. (2011). Severe alterations of cerebellar cortical development after constitutive activation of Wnt signaling in granule neuron precursors. Mol Cell Biol *31*, 3326-3338.

Machold R., F.G. (2005). Math1 is expressed in temporally discrete pools of cerebellar rhombic-lip neural progenitors. Neuron *48*, 17-24.

Madisen, L., Zwingman, T.A., Sunkin, S.M., Oh, S.W., Zariwala, H.A., Gu, H., Ng, L.L., Palmiter, R.D., Hawrylycz, M.J., Jones, A.R.*, et al*. (2010). A robust and high-throughput Cre reporting and characterization system for the whole mouse brain. Nat Neurosci *13*, 133-140.

Maka, M.C., Stolt, C.C., and Wegner, M. (2005). Identification of Sox8 as a modifier gene in a mouse model of Hirschsprung disease reveals underlying molecular defect. Dev Biol *277*, 155-169.

Mao, J., Ligon, K.L., Rakhlin, E.Y., Thayer, S.P., Bronson, R.T., Rowitch, D., and McMahon, A.P. (2006). A novel somatic mouse model to survey tumorigenic potential applied to the Hedgehog pathway. Cancer Res *66*, 10171-10178.

Maricich SM, H.K. (1999). Pax-2 expression defines a subset of GABAergic interneurons and their precurosors in the developing murine cerebellum. Journal of Neurobiology *41*, 281-294.

Matise, M.P., Epstein, D.J., Park, H.L., Platt, K.A., and Joyce, J.A. (1998). Gli2 is required for induction of floor plate and adjacent cells, but not most ventral neurons in the mouse central nervous system. Development *125*, 2759-2770.

Matsuda, N., Lu, H., Fukata, Y., Noritake, J., Gao, H., Mukherjee, S., Nemoto, T., Fukata, M., and Poo, M.M. (2009). Differential activity-dependent secretion of brain-derived neurotrophic factor from axon and dendrite. J Neurosci *29*, 14185-14198.

McAllister, N.R., and Lessnick, S.L. (2005). The potential for molecular therapeutic targets in Ewing's sarcoma. Curr Treat Options Oncol *6*, 461-471.

Mecklenburg, N., Garcia-Lopez, R., Puelles, E., Sotelo, C., and Martinez, S. (2011). Cerebellar oligodendroglial cells have a mesencephalic origin. Glia *59*, 1946-1957.

Merkle, F.T., Tramontin, A.D., Garcia-Verdugo, J.M., and Alvarez-Buylla, A. (2004). Radial glia give rise to adult neural stem cells in the subventricular zone. Proc Natl Acad Sci U S A *101*, 17528-17532.

Murphy, M.M., Lawsom, J.A., Mathew, S.J., Hutcheson, D.A., and Kardon, G. (2011). Satellite cells, connective tissue fibroblasts and their interactions are crucial for muscle regeneration. Development *138*, 3625-2637.

Muzumdar, M.D., Tasic, B., Miyamichi, K., Li, L., and Luo, L. (2007). A global double-fluorescent Cre reporter mouse. Genesis *45*, 593-605.

Nitzki, F., Zibat, A., Frommhold, A., Schneider, A., Schulz-Schaeffer, W., Braun, T., and Hahn, H. (2011). Uncommitted precursor cells might contribute to increased incidence of embryonal rhabdomyosarcoma in heterozygous Patched1-mutant mice. Oncogene *43*, 4428-4436.

Noor, A. (2010). Disruption at the PTCHD1 Locus on Xp22.11 in Autism Spectrum Disorder and Intellectual Disability. Sci Transl Med *2*.

Palma, V., Lim, D.A., Dahmane, N., Sanchez, P., Brionne, T.C., Herzberg, C.D., Gitton, Y., Carleton, A., Alvarez-Buylla, A., and Ruiz i Altaba, A. (2005). Sonic hedgehog controls stem cell behavior in the postnatal and adult brain. Development *132*, 335-344.

Palmen, S., van Engeland, H., Hof, P., and Schmitz, C. (2004). Neuropathological findings in autism. Brain *127*, 2572-2583.

Pan, F.C., Bankaitis, E.D., Boyer, D., Xu, X., Van de Casteele, M., Magnuson, M.A., Heimberg, H., and Wright, C.V. (2013). Spatiotemporal patterns of multipotentiality in Ptf1a-expressing cells during pancreas organogenesis and injury-induced facultative restoration. Development *140*, 751-764.

Pasca di Magliano, M., Sekine, S., Ermilov, A., Ferris, J., Dlugosz, A.A., and Hebrok, M. (2006). Hedgehog/Ras interactions regulate early stages of pancreatic cancer. Genes Dev *20*, 3161-3173.

Pascual, M., Abasolo, I., Mingorance-Le Meur, A., Martinez, A., Del Rio, J.A., Wright, C.V., Real, F.X., and Soriano, E. (2007). Cerebellar GABAergic progenitors adopt an external granule cell-like phenotype in the absence of Ptf1a transcription factor expression. Proc Natl Acad Sci U S A *104*, 5193-5198.

Patel, M., Simon, J.M., Iglesia, M.D., Wu, S.B., McFadden, A.W., Lieb, J.D., and Davis, I.J. (2012). Tumor-specific retargeting of an oncogenic transcription factor chimera results in dysregulation of chromatin and transcription. Genome Res *22*, 259-270.

Pei, Y., Brun, S.N., Markant, S.L., Lento, W., Gibson, P., Taketo, M.M., Giovannini, M., Gilbertson, R.J., and Wechsler-Reya, R.J. (2012). WNT signaling increases proliferation and impairs differentiation of stem cells in the developing cerebellum. Development *139*, 1724-1733.

Pierce, K., and Courchesne, E. (2001). Evidence for a cerebellar role in reduced exploration and stereotyped behavior in autism. Biol Psychiatry *49*, 655-664.

Qin, J., Lin, Y., Norman, R.X., Ko, H.W., and Eggenschwiler, J.T. (2011). Intraflagellar transport protein 122 antagonizes Sonic Hedgehog signaling and controls ciliary localization of pathway components. Proc Natl Acad Sci U S A *108*, 1456-1461.

Ramamoorthi, K., and Lin, Y. (2011). The contribution of GABAergic dysfunction to neurodevelopmental disorders. Trends Mol Med *17*, 452-462.

Read, T., Fogarty, M.P., Markant, S.L., McLendon, R.E., Wei, Z., Ellison, D.W., Febbo, P.G., and Wechsler-Reya, R.J. (2009). Identification of CD15 as a Marker for Tumor-Propagating Cells in a Mouse Model of Medulloblastoma. Cancer Cell *15*, 135-147.

Roessler, E., Ermilov, A.N., Grange, D.K., Wang, A., Grachtchouk, M., Dlugosz, A.A., and Muenke, M. (2005). A previously unidentified amino-terminal domain regulates transcriptional activity of wild-type and disease-associated human GLI2. Hum Mol Genet *14*, 2181-2188.

Rubin, B.P., Nishijo, K., Chen, H.I., Yi, X., Schuetze, D.P., Pal, R., Prajapati, S.I., Abraham, J., Arenkiel, B.R., Chen, Q.F.*, et al*. (2011). Evidence for an unanticipated relationship between undifferentiated pleomorphic sarcoma and embryonal rhabdomyosarcoma. Cancer Cell *19*, 177-191.

Ruiz i Altaba, A., Sanchez, P., and Dahmane, N. (2002). Gli and hedgehog in cancer: tumours, embryos and stem cells. Nat Rev Cancer *2*, 361-372.

Sabourin, L.A., and Rudnicki, M.A. (2000). The molecular regulation of myogenesis. Clin Genet *57*, 16-25.

Sanders, T.A., Llagostera, E., and Barna, M. (2013). Specialized filopodia direct long-range transport of SHH during vertebrate tissue patterning. Nature *497*, 628-632.

Sankar, S., Tanner, J.M., Bell, R., Chaturvedi, A., Randall, R.L., Beckerle, M.C., and Lessnick, S.L. (2013). A novel role for keratin 17 in coordinating oncogenic transformation and cellular adhesion in ewing sarcoma. Mol Cell Biol *33*, 4448-4460.

Scotlandi, K., Remondini, D., Castellani, G., Manara, M.C., Nardi, F., Cantiani, L., Francesconi, M., Mercuri, M., Caccuri, A.M., Serra, M.*, et al*. (2009). Overcoming resistance to conventional

drugs in Ewing sarcoma and identification of molecular predictors of outcome. J Clin Oncol *27*, 2209-2216.

Seale, P., Bjork, B., Yang, W., Kajimura, S., Chin, S., Kuang, S., Scime, A., Devarakonda, S., Conroe, H.M., Erdjument-Bromage, H., *et al*. (2008). PRDM16 controls a brown fat/ skeletal muscle switch. Nature *454*, 961-967.

Selvadurai, H.J., and Mason, J.O. (2011). Wnt/b-catenin Signalling Is Active in a Highly Dynamic Pattern during Development of the Mouse Cerebellum. PLoS One *6*, e23012.

Shukla, N., Schiffman, J., Reed, D., Davis, I.J., Womer, R.B., Lessnick, S.L., and Lawlor, E.R. (2013). Biomarkers in Ewing Sarcoma: The Promise and Challenge of Personalized Medicine. A Report from the Children's Oncology Group. Front Oncol *3*, 141.

Silbereis, J., Cheng, E., Ganat, Y.M., Ment, L.R., and Vaccarino, F.M. (2009). Precursors with GFAP promoter activity transiently generate GABA interneurons in the postnatal cerebellum. Stem Cells *27*, 1152-1163.

Sillitoe, R.V., Gopal, N., and Joyner, A.L. (2009). Embryonic origins of ZebrinII parasagittal stripes and establishment of topographical purkinje cell projections. Neuroscience *162*, 574-588.

Sillitoe, R.V., and Joyner, A.L. (2007). Morphology, molecular codes, and circuitry produce the three-dimensional complexity of the cerebellum. Annu Rev Cell Dev Biol *23*, 549-577.

Smith, R., Owen, L.A., Trem, D.J., Wong, J.S., Whangbo, J.S., Golub, T.R., and Lessnick, S.L. (2006). Expression profiling of EWS/FLI identifies NKX2.2 as a critical target gene in Ewing's sarcoma. Cancer Cell *9*, 405-416.

Smyth, G.K. (2004). Linear models and empirical bayes methods for assessing differential expression in microarray experiments. Stat Appl Genet Mol Biol *3*, Article3.

Solter, D., and Knowles, B.B. (1978). Monoclonal antibody defining a stage-specific mouse embryonic antigen (SSEA-1). Proc Natl Acad Sci U S A *75*, 5565-5569.

Soriano, P. (1999). Generalized lacZ expression with the ROSA26 Cre reporter strain. Nat Genet *21*, 70-71.

Sotelo, C. (2004). Cellular and genetic regulation of the development of the cerebellar system. Prog Neurobiol *72*, 295-339.

Srinivas S., W.T., Lin C.S., William C.M., Tanabe Y., Jessell T.M., Constantini F. (2001). Cre reporter strains produced by targeted insertion of EYFP and ECFP into the ROSA26 locus. BMC Dev Biol *1*.

Stolt, C.C., Rehberg, S., Ader, M., Lommes, P., Riethmacher, D., Schachner, M., Bartsch, U., and Wegner, M. (2002). Terminal differentiation of myelin-forming oligodendrocytes depends on the transcription factor Sox10. Genes Dev *16*, 165-170.

Straessler, K.M., Jones, K.B., Hu, H., Jin, H., van de Rijn, M., and Capecchi, M.R. (2013). Modeling clear cell sarcomagenesis in the mouse: cell of origin differentiation state impacts tumor characteristics. Cancer Cell *23*, 215-227.

Sudarov, A., Turnbull, R.K., Kim, E.J., Lebel-Potter, M., Guillemot, F., and Joyner, A.L. (2011). Ascl1 genetics reveals insights into cerebellum local circuit assembly. Journal of Neuroscience *31*, 11055-11069.

Sutter, R., Shakhova, O., Bhagat, H., Behesti, H., Sutter, C., Penkar, S., Santuccione, A., Bernays, R., Heppner, F.L., Schuller, U., *et al*. (2010). Cerebellar stem cells act as medulloblastoma-initiating cells in a mouse model and a neural stem cell signature characterizes a subset of human medulloblastomas. Oncogene *29*, 1845-1856.

SY, W., AD, S., PL, S., AN, E., CK, B., Jr, E.E., Dlugosz, A.A., and Reiter, J. (2009). Primary cilia can both mediate and suppress Hedgehog pathway-dependent tumorigenesis. Nat Med *15*, 1055-1061.

Taniguchi, E., Nishijo, K., McCleish, A.T., Michalek, J.E., Grayson, M.H., Infante, A.J., Abbound, H.E., Legallo, R.D., Qualman, S.J., Rubin, B.P., *et al*. (2008). PDGFR-A is a therapeutic target in alveolar rhabdomyosarcoma. Oncogene *27*, 6550-6560.

Temple, S. (2001). The development of neural stem cells. Nature *414*, 112-117.

Tian, H., Callahan, C.A., Dupree, K.J., Darbonne, W.C., Ahn, C.P., Scales, S.J., and de Sauvage, F.J. (2009). Hedgehog signaling is restricted to the stromal compartment during pancreatic carcinogenesis. Proc Natl Acad Sci U S A *106*, 4254-4259.

Tompers, D.M., and Labosky, P.A. (2004). Electroporation of murine embryonic stem cells: a step-by-step guide. Stem Cells *22*, 243-249.

Torchia, E.C., Boyd, K., Rehg, J.E., Qu, C., and Baker, S.J. (2007). EWS/FLI1 Induces Rapid Onset of Myeloid/ Erythroid Leukemia in Mice. Mol Cell Biol *27*, 7918-7934.

Traiffort, E., Moya, K.L., Faure, H., Hassig, R., and Ruat, M. (2001). High expression and anterograde axonal transport of aminoterminal sonic hedgehog in the adult hamster brain. Eur J Neurosci *14*, 839-850.

Trapnell, C., Pachter, L., and Salzberg, S.L. (2009). TopHat: discovering splice junctions with RNA-Seq. Bioinformatics *25*, 1105-1111.

Trapnell, C., Williams, B.A., Pertea, G., Mortazavi, A., Kwan, G., van Baren, M.J., Salzberg, S.L., Wold, B.J., and Pachter, L. (2010). Transcript assembly and quantification by RNA-Seq

reveals unannotated transcripts and isoform switching during cell differentiation. Nat Biotechnol *28*, 511-515.

Tsai, P.T., Hull, C., Chu, Y., Greene-Colozzi, E., Sadowski, A.R., Leech, J.M., Steinberg, J., Crawley, J.N., Regehr, W.G., and Sahin, M. (2012). Autistic-like behaviour and cerebellar dysfunction in Purkinje cell Tsc1 mutant mice. Nature *488*, 647-651.

Urs, S., Harrington, A., Liaw, L., and Small, D. (2006). Selective expression of an aP2/Fatty Acid Binding Protein 4-Cre transgene in non-adipogenic tissues during embryonic development. Transgenic Res *15*, 647-653.

Vokes, S.A., Ji, H., McCuine, S., Tenzen, T., Giles, S., Zhong, S., Longabaugh, W.J., Davidson, E.H., Wong, W.H., and McMahon, A.P. (2007). Genomic characterization of Gli-activator targets in sonic hedgehog-mediated neural patterning. Development *134*, 1977-1989.

von Bartheld, C.S., Byers, M.R., Williams, R., and Bothwell, M. (1996). Anterograde transport of neurotrophins and axodendritic transfer in the developing visual system. Nature *379*, 830-833.

Wallace, V.A. (1999). Purkinje-cell-derived Sonic hedgehog regulates granule neuron precursor cell proliferation in the developing mouse cerebellum. Curr Biol *9*, 445-448.

Wechsler-Reya, R.J., and Scott, M.P. (1999). Control of neuronal precursor proliferation in the cerebellum by Sonic Hedgehog. Neuron *22*, 103-114.

Weisheit, G., Gliem, M., Endl, E., Pfeffer, P.L., Busslinger, M., and Schilling, K. (2006). Postnatal development of the murine cerebellar cortex: formation and early dispersal of basket, stellate and Golgi neurons. Eur J Neurosci *24*, 466-478.

White, J.J., and Sillitoe, R.V. (2012). Development of the cerebellum: from gene expression patterns to circuit maps. WIRES Dev Biol.

Yamada, K., and Watanabe, M. (2002). Cytodifferentiation of Bergmann glia and its relationship with Purkinje cells. Anat Sci Int *77*, 94-108.

Yamanaka, H., Yanagawa, Y., and Obata, K. (2004). Development of stellate and basket cells and their apoptosis in mouse cerebellar cortex. Neuroscience Research *50*, 13-22.

Yang Z, E.T., Markant S, et al (2008). Medulloblastoma Can Be Initiated by Deletion of Patched in Lineage-Restricted Progenitors or Stem Cells. Cancer Cel *14*, 135-145.

Yauch, R.L., Dijkgraaf, G.J., Alicke, B., Januario, T., Ahn, C.P., Holcomb, T., Pujara, K., Stinson, J., Callahan, C.A., Tang, T.*, et al*. (2009). Smoothened mutation confers resistance to a Hedgehog pathway inhibitor in medulloblastoma. Science *326*, 572-574.

Yoshida, A., Sekine, S., Tsuta, K., Fukayama, M., Furuta, K., and Tsuda, H. (2012). NKX2.2 is a useful immunohistochemical marker for Ewing sarcoma. Am J Surg Pathol *36*, 993-999.

Yuasa, S. (1996). Bergmann glial development in the mouse cerebellum as revealed by tenascin expression. Anatomy and Embryology *194*, 223-234.

Zhang, L., and Goldman, J.E. (1996). Generation of cerebellar interneurons from dividing progenitors in white matter. Neuron *16*, 47-54.

Zhu, L., Gibson, P., Currle, D.S., Tong, Y., Richardson, R.J., Bayazitov, I.T., Poppleton, H., Zakharenko, S., Ellison, D.W., and Gilbertson, R.J. (2009). Prominin 1 marks intestinal stem cells that are susceptible to neoplastic transformation. Nature *457*.

Zwerner, J.P., Joo, J., Warner, K.L., Christensen, L., Hu-Lieskovan, S., Triche, T.J., and May, W.A. (2008). The EWS/FLI1 oncogenic transcription factor deregulates GLI1. Oncogene *27*, 3282-3291.